THIN METASTRUCTURES WITH ENGINEERED THERMAL EXPANSION

Thesis by
Eleftherios E. Gdoutos

In Partial Fulfillment of the Requirements for the
degree of
Doctor of Philosophy

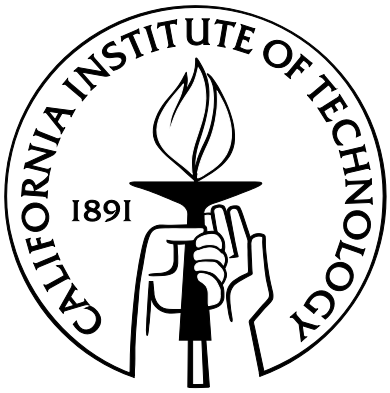

CALIFORNIA INSTITUTE OF TECHNOLOGY
Pasadena, California
2013
(Defended April 24, 2013)

To my family and friends.

ACKNOWLEDGEMENTS

I express by deepest gratitude to my adviser, Professor Chiara Daraio, who allowed me the opportunity to initiate and complete this work. Her tutelage has invaluably guided me to develop my academic capacity by deepening my scientific understanding and by always motivating me to appreciate the broad implications of my research. During my graduate career, she has been a true mentor. I greatly appreciate it.

I am deeply indebted to the members of my thesis committee: Professor Guruswami Ravichandran, Professor Sergio Pellegrino, and Dr. Andrew Shapiro. Professor Ravichandran's calm, confident counsel will always inspire me. I especially thank Professor Pellegrino for his support, particularly when projects took an unexpectedly longer amount of time. I am genuinely grateful for Dr. Shapiro's weekly advice and insistence on new experimental techniques and solution approaches; I have learned a lot. I thank Professor Kaushik Bhattacharya for encouraging me to critically evaluate research assumptions during my candidacy exam. I am grateful to Professor Ares Rosakis for informing me in my decision to attend this wonderful institution. I profoundly thank all my instructors at Caltech: Professor Oscar Bruno, Dr. Yunjin Kim, Dr. Jay Polk, Professor Dan Meiron, Professor Niles Pierce, Dr. Greg Davis, Dr. Mike Watkins, Professor Dale Pullin, Professor Houman Owhadi, Mr. Alireza Ghaffari, Professor Tapio Schneider, Professor Colin Camerer, and Professor Ken Pickar.

I would also like to acknowledge Ms. Dimity Nelson, Ms. Cheryl Gause, Ms. Christine Ramirez, and Ms. Jennifer Stevenson. They always provided the best support I could hope for.

I sincerely acknowledge my collaborators at JPL: Dr. Harish Manohara, Dr. Risaku Toda, Dr. Victor White, and Mr. Jerry Mulder. I especially thank Mr. Mulder for his tremendous effort in sample welding. I also thank Mr. Joe Haggerty for finding answers to even the most challenging machining questions.

I thank the members of my lab group who welcomed me to the group in my first year. What I learned from Dr. Nick Boechler, Dr. Dev Khatri, Dr. Abha Misra, and Dr. Jordan Raney has been immensely useful. My collaboration with Dr. Namiko Yamamoto has been educational and rewarding and I thank her for that. I thank all my officemates and lab group members: Dr. Carly Donahue, Ivan Szelengowicz, Andrea Leonard, Joseph Lydon, Sebastian Liska, Ludovica Lattanzi, Paul Anzel, Wei-Hsun Lin, Ramathasan Thevamaran, Hayden Burgoyne, Luca Bonanomi, and Marc Serra Garcia.

I thank the Graduate Student Council for allowing me the opportunity to contribute to the organization and I thank the Caltech Graduate Office, particularly Professor Joseph Shepherd and Dr. Felicia Hunt for our excellent collaboration. I thank all the organizers of the Inaugural Student–Faculty Colloquium. They guaranteed the event's success with tremendous effort.

I thank everyone whose friendship I shared at Caltech: Jocelyn Escourrou, Philipp Oettershagen, Juan Pedro Mendez Ganado, Adrian Sanchez Menguiano, Kristen John, Ignacio Maqueda, Stephanie Coronel, Siddhartha Verma, Jomela Meng, Vicki Stolyar, Andy Galvin, Gloria Sheng, and Panagiotis Natsiavas. I especially thank Landry Fokoua Djodom and Namiko Saito. Their friendship has been and will continue to be invaluable.

I am obliged to my best friends from college Mustafa Hassan and Akif Irfan. I am thankful to have had the opportunity to build lifelong friendships in Los Angeles: Chris Scullin, Nicole Barefoot, and Kathryn Barefoot, thank you. I must especially

recognize Eleni Barefoot, who has been an unwavering source of support, motivation, and liveliness; I am, indeed, privileged.

I am most thankful to my parents and sister. Mom's, Dad's, and Alex's encouragement, love, and well-timed visits to Pasadena have been instrumental in this endeavor. Their lifelong teaching has shaped who I am. Thank you.

ABSTRACT

The geometry and constituent materials of metastructures can be used to engineer the thermal expansion coefficient. In this thesis, we design, fabricate, and test thin thermally stable metastructures consisting of bi-metallic unit cells and show how the coefficient of thermal expansion (CTE) of these metastructures can be finely and coarsely tuned by varying the CTE of the constituent materials and the unit cell geometry. Planar and three-dimensional finite element method modeling is used to drive the design and inform experiments, and predict the response of these metastructures. We demonstrate computationally the significance of out-of-plane effects in the metastructure response. We develop an experimental setup using digital image correlation and an infrared camera to experimentally measure full displacement and temperature fields during testing and accurately measure the metastructures' CTE. We experimentally demonstrate high aspect ratio metastructures of Ti/Al and Kovar/Al which exhibit near-zero and negative CTE, respectively. We demonstrate robust fabrication procedures for thermally stable samples with high aspect ratios in thin foil and thin film scales. We investigate the lattice structure and mechanical properties of thin films comprising a near-zero CTE metastructure. The mechanics developed in this work can be used to engineer metastructures of arbitrary CTE and can be extended to three dimensions.

TABLE OF CONTENTS

LIST OF FIGURES

LIST OF TABLES

Chapter 1

INTRODUCTION

Thermal expansion is usually considered an intrinsic material property not dependent on geometry. In this thesis, we demonstrate the ability to engineer high aspect ratio material ensembles that exhibit desired thermal expansion beyond the bounds of their constituents. We design, fabricate, and characterize material ensembles that exhibit near-zero and negative coefficients of thermal expansion (CTE) in thin foil and thin film scales, a combination which has not been demonstrated before.

A lot of work has been conducted over the last century on discovering and elucidating the behavior of materials that exhibit unique thermal properties such as low and negative CTE [1-3]. In the past decade, in addition to the discovery of materials with unique properties, work has focused on designing material ensembles that exhibit engineered properties by leveraging their geometry, periodicity, and material properties. *Metamaterials*, as they are usually called, exhibit unique acoustic or electromagnetic properties, such as sound wave manipulation, negative index of refraction, and artificial magnetism [4-6]. In this work, we develop high aspect ratio bi-material ensembles that exhibit near-zero and negative CTE through their constituent material properties and structural geometry. These material ensembles are termed *metastructures*; they derive their properties primarily from their mechanical structure. We engineer near-zero and negative CTE metastructures in thin foil and thin film scales. By realizing and

characterizing these metastructures, we demonstrate that a breadth of CTEs outside the limits of the CTE exhibited by available materials can be attained.

This thesis focuses on the development, characterization, and application of thin metastructures with tailored CTE. We expound upon the physical principles describing CTE tunability and characterize metastructure unit cells and arrays in thin foil and thin film size scales. We establish an experimental setup to characterize the thermal behavior of these metastructures and develop a computational model to predict and explain their unique behavior. We further develop a robust fabrication procedure to experimentally realize near-zero and negative CTE metastructures in previously unachievable scales.

1.1 Applications for Metastructures with Engineered CTE

The ability to engineer the coefficient of thermal expansion (CTE) of materials is highly impactful in applications where thermal strains may cause failure or decreased performance. Particularly in systems that experience temperature cycling throughout their operation or lifetime, it is advantageous that component materials either exhibit low CTE or match the CTE of an underlying structure. Examples of such systems abound in aerospace, the energy and semiconductor industries, civil engineering, and even biomedical applications [7-10]. Earth-orbiting spacecraft can experience temperature variations as large as 150 K as they orbit in shadow and sunlight and potentially develop high thermal strains. In these cases, use of low-CTE materials is warranted in the design process [11, 12]. Thermal expansion mismatch is known to cause cracks in solar cells and packaged semiconductor chips [13-15]. To avoid such failures, engineers use materials that have similar CTE. In microelectromechanical systems (MEMS,) medical applications, and civil structures thermal expansion is a critical design consideration [7, 16-18]. The desire for

improved performance and lower failure rates has given rise to demand for materials with low and tunable CTE.

To meet this demand, various materials have been used. Zerodur, a lithium aluminosilicate glass-ceramic trademarked by Schott Glass Technologies, and other glasses have been used for large telescope mirrors thanks to their low CTE (0 - 2 ppm/^{o}C) [19]. In silicon integrated chips (IC's), silicon, aluminum nitride, and silicon carbide have been used to match the CTE of the IC to prevent thermal-stress induced cracking [15]. Invar (nickel iron alloy $Fe_{64}Ni$) and other nickel alloys are used in a variety of applications where thermal stability and toughness is desired. Carbon composites, which exhibit low CTE, have applications ranging from automotive to aerospace. Despite their widespread use, however, these materials exhibit several limitations: ceramics are brittle; the CTE of nickel alloys tends to vary significantly with temperature; composites are prone to thermal fatigue and are usually costly.

An alternative approach is to develop metastructures which are designed to exhibit the desired CTE. The obvious advantage of this approach is that the range of achievable CTE is much greater than it would be by using single materials. Indeed, variable CTE metastructure concepts have been presented as early as 1996 by Sigmund and Torquato [20] and Lakes [21] who showed composite structures with theoretically unbounded CTE. More recently, Steeves et al [22] and Berger et al [23] have designed and experimentally realized bi-metallic 2D metastructures that exhibit near-zero CTE. These metastructures have been experimentally shown to exhibit low CTE over a wide temperature range (25 – 220 ^{o}C) and theoretically can exhibit unbounded CTE (though in practice the CTE range is limited by the availability of constituent materials). The metastructures exhibit high in-plane stiffness and their metallic constituents contribute to robustness compared to ceramics. Limitations, however, still exist. Previous work has not experimentally

shown negative CTE metastructures; fabrication techniques have limited applicability to large structures; the effect of structural design parameters is not well understood; and out-of-plane deformations have not been thoroughly studied.

1.2 Thesis Objectives

In this thesis, we aim to extend scientific understanding in the field of metatsructures with near-zero and negative CTE by:

(i) Designing and experimentally realizing low and negative CTE metastructures

(ii) Extending the fabrication limits of these metastructures to thin foils and thin films

(iii) Elucidating scientific principles governing the mechanics of these metastructures

(iv) Predicting the thermal behavior of these metastructures through computational modeling

(v) Leveraging the understanding of the thermal deformation mechanics of these metastructures to develop an accurate predictive model of their CTE.

1.3 Definition of CTE for Metastructures

Coefficient of thermal expansion (CTE) denotes a material's geometric dependence on temperature under specified thermodynamic conditions. Most materials will

expand when they undergo a positive temperature change. Mathematically, the coefficient of thermal expansion (CTE) tensor, $\alpha_{ij,}$ is the temperature derivative of the strain tensor, e_{ij}, under constant pressure [24]:

$$a_{ij} = \left(\frac{\partial e_{ij}}{\partial T}\right)_p. \tag{1.1}$$

Of course, the true strain tensor (with reference to the deformed configuration where u_i is the deformation tensor) and Cauchy strain tensor, ε_{ij} are defined as:

$$e_{ij} = \frac{1}{2}\left(\frac{\partial u_i}{\partial x_j} + \frac{\partial u_j}{\partial x_i} - \frac{\partial u_k}{\partial x_i}\frac{\partial u_k}{\partial x_j}\right) \text{ and } \varepsilon_{ij} = \frac{1}{2}\left(\frac{\partial u_i}{\partial x_j} + \frac{\partial u_j}{\partial x_i}\right). \tag{1.2}$$

My work will focus on small deformations and thus from this point "strain" will refer to the Cauchy strain, ε_{ij}. By assuming a linear dependence of strain on temperature (which is accurate for small temperature changes, around non-cryogenic temperatures [24]) we can write:

$$a_{ij} = \frac{\varepsilon_{ij}}{\Delta T}. \tag{1.3}$$

Ignoring shear strains, we can compute the CTE along a particular direction using the following expression:

$$a = \frac{l_f - l_i}{l_i}\frac{1}{T_f - T_i}. \tag{1.4}$$

Using Equation 1.4, in which l denotes length along a specific direction and subscripts f and i denote the final and initial configurations respectively, one can compute the CTE of any material along that direction by applying a temperature change and measuring the original length and change in length of an infinitesimally thin segment along that direction.

This definition of CTE is applicable and useful when defining thermal expansion between atoms in a crystal. In this way, we use this definition of CTE to characterize the thermal response of metastructures. In the same way that atomic unit cells are building blocks for crystals, structural unit cells are building blocks for metastructures. The CTE of metastructures is thus defined discreetly, between nodes of unit cells within the metastructure.

1.4 Thesis Organization

This thesis is organized in six chapters: Chapter 1 presents scientific context for the work of this thesis and outlines the objectives. Chapter 2 presents an introduction to the physics behind thermal expansion and reviews previous work in materials and metastructures with unique CTE. The focus is on metastructures. Advantages and limitations of previous work are critically evaluated. Chapter 3 presents the design of thin foil unit cell metastructures exhibiting low and negative CTE. An experimental setup to measure the CTE of these metastructures is developed and near-zero thin foil CTE unit cells are experimentally realized. A predictive model based on a computational sensitivity analysis is developed and verified. Chapter 4 presents the design and experimental realization of thin foil metastructure arrays exhibiting low and negative CTE. An experimental setup to study the deformation mechanics of these metatrustructure arrays is developed and negative and near-zero CTE metatsructure arrays are experimentaly delivered. A computational model is used to compare with experimental results and provide insight to the deformation mechanics. Chapter 5 presents the characterization of the Al and Ti thin film constituents of a near-zero CTE thin film metastructure. The grain size, elastic modulus, atomic orientation, and intrinsic film stress is characterized. Chapter 6 demonstrates the design of thin film metastructure arrays exhibiting near-zero CTE. A novel fabrication procedure to achieve free-standing

thin films is described and the CTE is measured. Chapter 7 outlines the conclusions of this thesis and presents possible future extensions of this work.

Chapter 2

BACKGROUND

The observation that materials tend to expand when heated dates back to the first century when ancient Greek mathematician and engineer Heron of Alexandria noted that air expands in the presence of fire. In the 17th century the concept of temperature was introduced and Galileo used scientific principles to design the first gas thermometers. In 1714, the first precision mercury thermometer was developed by German-born physicist G.B. Fahrenheit (1686 – 1736). Still, thermal expansion was not well understood as a material property (but rather as a way to define temperature) until the realization that different solids expanded at different rates was prompted by the study of pendulum clocks in the 1730s [24]. It was not until the 20th century that scientific principles were used to explain thermal expansion.

Interest in thermal expansion grew in the middle of the 20th century as demand for materials with low CTE shifted beyond pendulum clocks to the automotive industry (engine components), consumer products (usually cookware), electronic devices, and scientific instruments (mostly telescopes). The search and design for materials with low-CTE usually centered on ceramics and metal alloys [1-3, 19] until the 1970s with the interest on effective properties of composite materials and foams [25-27]. Since then, a lot of work has been conducted on the design and development of materials and metastructures with desired thermal properties, initially theoretically and more recently, experimentally [20, 22, 23, 28-30].

2.1 Thermodynamic Foundations of Thermal Expansion

Scientific explanations of thermal expansion were initially formulated by Mie and Gruneisen in the early 1900s [31-34]. Based on their work the volumetric CTE, a_V, can be derived from thermodynamic principles:

$$\mathrm{a_V} = \frac{\gamma \mathrm{C_V} \chi_\mathrm{T}}{\mathrm{V}} = \frac{\gamma \mathrm{C_p} \chi_\mathrm{s}}{\mathrm{V}}, \tag{2.1}$$

where γ (Gruneisen's parameter) is a parameter relating the volume of a lattice to its vibrational frequency, C_V and C_p are the heat capacities at constant volume and pressure, χ_T and χ_s are the isothermal and adiabatic compressibilities (bulk moduli), and V is the lattice volume. Equation 2.1 provides an intuitive understanding of CTE as the effect of the nonlinearly dependent force experienced by an atom as a function of displacement from its equilibrium position as through Gruneisen's parameter:

$$\gamma = -\frac{\partial \ln(\omega_\mathrm{i})}{\partial \ln(\mathrm{V})}, \tag{2.2}$$

where ω_i is the i^{th} vibrational mode frequency. Equation 2.2 vanishes when the atomic force-displacement relation is linear; no dependence of vibrational frequency of volume is observed in that case.

Equation 2.1 was found to be accurate for a wide temperature range for many solids and lays down the essentials for understanding thermal expansion from a thermodynamic point of view. It accurately accounts for the experimentally observed correlation between CTE, heat capacity, and compressibility. However, Equation 2.1 does not take into account two critical aspects of thermal expansion: (i) non-vibrational effects seen at ferromagnetic phase transitions and (ii) thermal expansion anisotropy [24]. These two mechanisms are usually responsible for the

low or negative CTE exhibited by certain materials. Furthermore, it is often difficult to compute Gruneisen's parameter from first principles without significant simplifications. Later work on the understanding of thermal expansion has focused on accurately computing Gruneisen's parameter and generalizing the same principles to take into account non-vibrational effects and anisotropy [24]. These principles have been used to explain the low or negative CTE exhibited by certain materials.

Sections 2.2 and 2.3 review the scientific background behind commonly found low/negative CTE materials (< 2 ppm/^{o}C) and metastructures.

2.2 Low and Negative CTE Materials

Most low CTE materials discovered so far are either ceramics or metal alloys [1, 2]. While advances in polymer technology have enabled the engineering of relatively low in-plane CTE (~4 ppm/^{o}C) polyimide films, this comes at the cost of high out-of-plane CTE [35, 36]. Sections 2.2.1 and 2.2.2 review scientific background on low-CTE ceramics and metal alloys respectively.

2.2.1 Oxide Ceramics

A lot of previous work has focused on characterizing oxide ceramics with low or negative CTE. Table 2.1 [1] lists some of these oxides and their average CTE over a broad temperature range. In general the low/negative CTE of most oxides is due to a combination of the following two factors: (i) stiff, three-dimensionally linked bonds which resist change in bond length and (ii) atomic structures with low packing density that enables the lattice to accommodate thermal energy in transverse vibrations, perpendicular to the bond directions, effectively converting thermal energy to potential energy.

Material	**Average CTE (ppm/°C)**	**Temperature range (°C)**
β-Spodumene	0.9	25-1000
β-Eurocryptite	-6.2	25-1000
Cordierite	1.4	25-800
NZP	0.6	25-1000
$NaZr_2P_3O_{12}$	-0.4	25-1000
Nb_2O_5	1.0	25-1000
Al_2TiO_5	1.4	25-800
$Zr_2P_2O_9$	0.4	25-600
$Be_3Al_2Si_6O_{18}$	2.0	25-1000
SiO_2	0.5	25-1000
Zerodur	0.12	20-600

Table 2.1 Average CTE over measured temperature for various low and negative CTE oxides.

Zerodur (CTE = 0.12 ppm/°C), a glass ceramic produced by Schott, has been widely applied as a mirror in large telescopes, such as Keck I and Keck II. Its composition is ~70% crystalline and ~30% amorphous. The CTE highly depends on the phase ratio. The crystalline and amorphous phases exhibit negative and positive CTE, respectively. The low CTE behavior of Zerodur is thus enabled by appropriately controlling the two phases to balance the overall CTE. This is a significant advantage as the CTE of Zerodur can be engineered depending on the phase ratio.

The crystalline phase exhibits negative CTE with a similar mechanism to β-Spodumene (CTE = 0.9 ppm/°C), β-Eurocryptite (CTE = -6.2 ppm/°C). These oxides exhibit very strong bonds in three dimensions and atomic structures which accommodate thermal energy in gaps within the crystal [37-39].

Zerodur and related glass-ceramics have been successfully used in aerospace and astronomical applications. However, two main drawbacks limit their widespread use. First, manufacturing and shaping Zerodur is costly and time-consuming.

Secondly, as most ceramics, Zerodur is brittle. This severely limits its applicability when considering thin sheets (e.g., usually an aspect ratio between diameter and thickness of at most four is maintained for solid Zerodur substrates) [40, 41].

2.2.2 Transition Metal Alloys and Invar

Metals usually exhibit CTE one order of magnitude higher than ceramics. However, a specific set of transition metal alloys has been shown to exhibit very low CTE and unique elastic properties. The most well-known of these alloys, Invar, was discovered in 1897 by Guillaume who, for this discovery, was awarded the 1920 Nobel prize in physics [42]. This $Fe_{65}Ni_xMn3_{5-x}$ face-centered cubic alloy (for x = 35) gained its name due to its approximate dimensional invariance under temperature change [24].

Depending on the nickel composition of the alloy, Invar's CTE can range from ~0.5 to ~20 ppm/°C. Common grades (35% nickel) usually exhibit CTE of ~1.2 ppm/°C though grades designed for CTE of 5.3 ppm/°C are also developed for electronics packaging components. Invar's CTE is an order of magnitude below what is predicted by the Gruneisen model [43, 44]. The explanation for Invar's low CTE is related to ferromagnetic phases that occur when the nickel concentration is ~35%. Various specific mechanisms to explain this phenomenon have been proposed, however, none so far succeed in describing Invar's unique behavior comprehensively [45-48].

Invar is widely used in applications where thermal stability is desirable. Early applications included pendulum clocks, thermostats, and ceramic-to-metal seals. More recently, Invar has been used in precision measurement instruments, composite molds for the aerospace industry, and cryogenic transport containers [49]. It has natural advantages over ceramics due to its ductility, it exhibits high stiffness (similar to titanium), and its use for more than a century has led to

thorough characterization and advances in manufacturability. However, the applicability of Invar is limited by physical principles. Invar's CTE is roughly invariable over a small temperature range (4 to 38 °C) and substantially diminishes in temperatures higher than 100 °C due to loss of ferromagnetism as the Curie temperature (225 °C) is approached. Invar also tends to exhibit creep behavior and has a high tendency to oxidize [14, 50, 51]. The small temperature range of Invar's low CTE has significantly limited its use in aerospace and other applications where high temperature ranges cannot be avoided.

2.3 Material Ensembles with Low or Negative Thermal Expansion Coefficient

Material ensembles, such as certain fiber composites and low-CTE metastructures exhibit low CTE thanks to their structure and constituent materials. The low-CTE of fiber composites is usually due to the low CTE of the fiber material; for low-CTE metastructures, structural design enables CTEs outside the bounds of the constituent materials.

2.3.1 General Two-Phase Materials and Fiber Composites

The effective thermoelastic properties of multiphase materials have been thoroughly studied [52-57]. Initially, Kerner derived the thermal expansion of a composite of packed grains based on the volume fraction and the shear modulus [52]. Hashin and Shtrikman used variational principles to derive tight bounds for the elastic properties of alloys, in agreement with experimental findings [53]. These bounds were later simplified and used to determine the elastic properties of anisotropic composite materials by Milton et al. [54]. By relating elastic properties to thermal expansion, Rosen and Hashin derived exact expressions for the thermal expansion tensor of two-phase composites as a function of their geometry and bulk

modulus [55]. While it can be shown that for three-phase composites (such as the metastructure studied here) it is not possible to find exact expressions relating bulk modulus to thermal expansion, bounds on the CTE can be developed [56, 57]. The tightest bounds for the CTE and biaxial stiffness of composites as a function of area fraction were developed by Gibiansky and Torquato [56]. These bounds demonstrate that the ensemble CTE need not be bounded by the CTEs of its constituents but also obviate the trade-off between biaxial stiffness and CTE.

Carbon-fiber reinforced composites, a particular type of composite materials, are widely used in commercial, high-end automotive, and aerospace applications thanks to their high specific strength and stiffness. In addition to those properties, carbon fiber composites can also exhibit near-zero CTE due to the negative in-plane CTE of graphite. The overall CTE of the composite is usually anisotropic and depends on the volume fraction, type of matrix, and heat treatment. It usually ranges between ~0-2 ppm/^{o}C for carbon fiber composites. However, carbon fiber composites experience two important limitations: (i) they are prone to thermal fatigue and delamination due to the CTE mismatch between fiber and matrix and (ii) the mechanism resulting in low-CTE for fiber composites limits the lower bound of the CTE to that of the fiber.

2.3.2 Low-CTE Metastructures

The first metastructures with engineered CTE can be attributed to Sigmund and Torquato, Gibiansky and Torquato, and Lakes [20, 21, 28, 56]. Steeves et al. and Berger et al. developed low-CTE metastructures following principles of previous work but with increased stiffness [22, 23, 29, 30]. Jefferson et al. patented a low-CTE metastructure design in 2012 [58]. All designs use high and low CTE materials to achieve effective CTE outside the bounds of those materials. Figure 2.1 shows

schematics of the low-CTE metastructure designs developed by Lakes (a) and Steeves (b).

The design by Lakes (Figure 2.1a) uses a series of bimaterial strips which undergo bending when experiencing temperature change. Bending causes an effective contraction in unidirectional length with the expansion in the normal direction accommodated by open space.

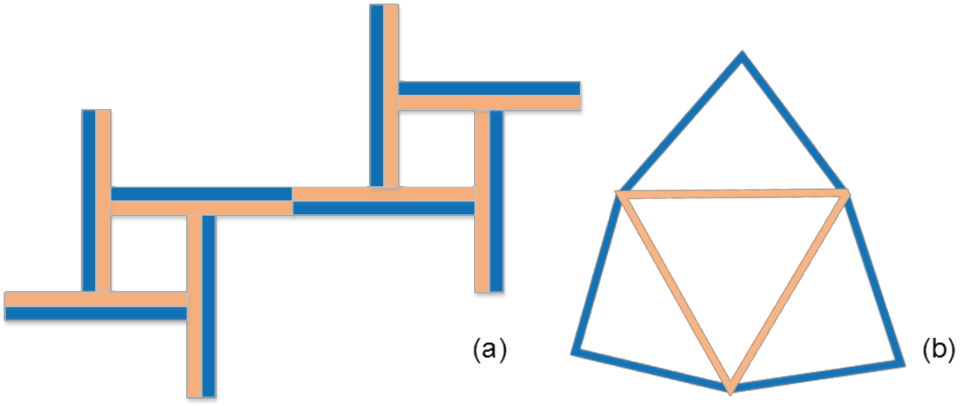

Figure 2.1 (a) Metastructure with unbounded CTE designed by Lakes [21]. (b) Metastructure with low CTE designed by Steeves et al. [22]. High and low CTE materials are indicated by blue (darker) and orange (lighter) colors, respectively.

The curvature, κ, of a bimaterial beam as a result of thermal bending can be computed by [21, 59, 60]:

$$\kappa = \frac{6(\alpha_2-\alpha_1)}{(h_1+h_2)} \frac{\Delta T\left(1+\frac{h_1}{h_2}\right)^2}{3\left(\left(1+\frac{h_1}{h_2}\right)^2\right)+\left(1+\frac{h_1E_1}{h_2E_2}\right)\left(\left(\frac{h_1}{h_2}\right)^2+\frac{h_2E_2}{h_1E_1}\right)}, \tag{2.3}$$

where subscripts *1* and *2* denote material 1 and 2 respectively, α denotes CTE, h denotes beam height, E denotes elastic modulus and ΔT denotes temperature change. The overall CTE of a metastructure designed by Lakes can be computed by the considering the strain as a result of curvature increment $d\kappa$:

$$\varepsilon = \left(\frac{1}{2}\cot\left(\frac{\theta}{2}\right) - \frac{1}{\theta}\right) l_{arc}\, d\kappa, \tag{2.4}$$

where l_{arc} is the length of a bimaterial beam or arc and ϑ is the included angle. Thus the CTE, α, can be expressed as:

$$\alpha = \frac{l_{arc}}{(h_1+h_2)} \frac{6(a_2-a_1)\left(1+\frac{h_1}{h_2}\right)^2}{3\left(\left(1+\frac{h_1}{h_2}\right)^2\right)+\left(1+\frac{h_1E_1}{h_2E_2}\right)\left(\left(\frac{h_1}{h_2}\right)^2+\frac{h_2E_2}{h_1E_1}\right)} \left(\frac{1}{2}\cot\left(\frac{\theta}{2}\right) - \frac{1}{\theta}\right). \tag{2.5}$$

By manipulating the geometric and material parameters in Equation 2.5, arbitrarily high and low values of CTE can be achieved. Whether the CTE is positive or negative depends on the placement of constituents within each bimaterial beam (the metastructure shown in Figure 2.1a exhibits negative CTE). This metastructure exhibits 2D cubic symmetry which results in isotropic thermal expansion but anisotropic elasticity. However, hexagonal, elastically isotropic metastructures can also be designed with the same principles. The main advantage of this design is that it can achieve theoretically unbounded CTE.

However, the design proposed by Lakes [21] has not yet been experimentally realized. Jefferson et al. [58] patented the design and analysis of a very similar structure to Lakes', though it is not mentioned whether that structure has been experimentally realized. The main limitation of this design is that it is dominated by bending, and thus exhibits low in-plane stiffness and strength which limits manufacturability.

Sigmund and Torquato [20, 28] employ topology optimization to achieve desired thermal expansion and stiffness properties. Their method begins with an initial design guess and explores the geometric design space by minimizing a cost function until a converged design is reached. Material parameters are generally specified initially.

The main advantage of this algorithm is that it describes a general approach to design any bimaterial structure for a set of properties, as long as the cost function can be defined. Using this methodology, Sigmund and Torquato optimized the geometry for bimaterial metastructure designs which exhibit zero and negative CTEs as well as high biaxial stiffness. However, a significant limitation of this approach is that the resulting designs tend to be too complicated for manufacturing. Additionally, the optimization algorithm is prone to falling into local minima, so it is important to test a variety of initial guesses. Another limitation is that the approach can optimize for geometry or material properties, but not for both.

More recently, Steeves et al. and Berger et al. [22, 23, 29, 30] showed that through another periodic arrangement in a two-dimensional truss-like structure of two pin jointed materials with different CTEs (Figure 2.1b) the overall response of the metastructure can exhibit zero CTE. The CTE, α, of a pin-jointed metastructure can be easily derived:

$$\alpha = \alpha_1 \frac{1-\frac{1}{2}\left(\frac{\alpha_2}{\alpha_1}\right)\sin(2\theta)\left(\frac{1}{\sqrt{3}}+\tan(\theta)\right)}{1-\frac{1}{2}\sin(2\theta)\left(\frac{1}{\sqrt{3}}+\tan(\theta)\right)}. \tag{2.6}$$

In Equation 2.6, subscripts *1* and *2* denote materials 1 and 2, α denotes the material CTE and ϑ denotes a characteristic design angle. Equation 2.6 assumes that members undergo only axial stresses. This assumption limits the applicability of Equation 2.6 to slender beams.

With a few more calculations the CTE for a metastructure with bonded joints can be derived [61]:

$$\alpha = \alpha_1 \left(1 - \frac{(C_1 \tan(\theta)(\sin(2\theta)+\sqrt{3}\cos(2\theta))-12(\cos(\theta)+\sqrt{3}\sin(\theta)^2)\left(\frac{a_2}{a_1}-1\right)}{C_1(\sqrt{3}\cos(\theta)-\sin(\theta))^2+12(\cos(\theta)+\sqrt{3}\sin(\theta))\left(\cos(\theta)+\sqrt{3}\sin(\theta)+2\frac{E_1A_1}{E_2A_2}\right)}\right), \tag{2.7}$$

where $C_1 = \frac{A_1 l_1^2}{I_1}$ and A denotes the area, E, the elastic modulus, l_l the side length of material 1, and I, the second moment. Equation 2.7 takes into account bending stresses in material 1 but not in material 2.

Equations 2.6 and 2.7 perform well for metastructures in which material 1 (blue/dark in Figure 2.1) exhibits low width to length ratio. However, when the thickness to length ratio increases the analytical predictions deviate significantly (up to ~ 200% error in this work) from FEM results. This effect is also observed in [61] and is attributed to incorrect effective length estimation of the frame. To achieve better agreement with FEM results scaling factors are used in [61].

Steeves et al. and Berger et al. [22, 23] also provide expressions for the biaxial stiffness, S_b, (such that $S_b = \frac{\varepsilon}{N_b}$, where N_b is the force applied) of the pin-jointed metastructures:

$$\mathrm{S_b} = \frac{\frac{\mathrm{E_2A_2}}{\mathrm{L}}\cos\left(\frac{\pi}{6}+\theta\right)\left(3-2\sqrt{3}\sin(\theta)\sin\left(\frac{\pi}{6}+\theta\right)\right)}{3\mathrm{Q}+2\sin^2(\theta)\sin\left(\frac{\pi}{6}+\theta\right)},\ \mathrm{Q} = \frac{\mathrm{E_2A_2}}{\mathrm{E_1A_1}}. \tag{2.8}$$

Equation 2.8 is shown to fall closely within the Gibiansky-Torquato [56] bounds for the area fraction of a three-phase system (two materials and gaps) when the biaxial stiffness is prescribed. The closeness to this bound suggests that, from a stiffness perspective, this may be an optimal design. Steeves et al.'s and Berger et al.'s design performs comparably against this bound to the designs obtained with shape optimization by Sigmund and Torquato [20, 28].

These structures were fabricated with 3 mm thick Ti and Al plates. Examples of bonded and pin-jointed metastructures were shown. Their CTE was characterized experimentally and computationally and their stiffness and in-plane buckling

behavior was characterized computationally [23, 29]. Detailed design principles were also developed [23].

The work by Steeves et al. and Berger et al. significantly advanced the state of the art of low CTE metastructures. They experimentally showed, for the first time, the manufacturability of such metastructures and also developed theoretical principles for predicting their CTE and stiffness. However, Steeves et al. and Berger et al. demonstrated the applicability of the design principles only in large, macroscale structures; the minimum thickness achieved was 3 mm. The fabrication principles and analysis that they performed are not scalable to thinner structures. Furthermore, they did not take into account 3D effects which become significant in high-aspect ratio metastructures. Also, while they allude to the potential of negative CTE, they did not experimentally demonstrate it. Finally, the accuracy of the theory predicting the CTE of bonded metastructures diminishes as the metastructure frame gets wider, a shortcoming which is mentioned but not addressed.

Chapter 3

ENGINEERED THERMAL EXPANSION METASTRUCTURE UNIT CELLS

In this chapter, we study the design and testing of thin (< 200 μm), tunable CTE unit cells with large aspect ratios (~100) [62]. These unit cells can be periodically arranged to 2D arrays. Such structures are well suited for applications where low thickness, high aspect ratio, and mechanical flexibility are desirable, such as biomedical devices, solar energy systems, and semiconductors. The large aspect ratio of the metastructures in my design causes sensitivity to stress concentration. To manage these stresses we add curvature to the unit cell in the areas close to the low CTE points. We model the metastructures using both planar and full three-dimensional finite element models to guide the design of the materials' interfaces and to inform the experiments. In order to design a thin and thermally stable unit cell we draw inspiration from previous theoretical work [22] as a starting point and employ FEM simulations to drive the design process. In 2007, Steeves et al. [22] showed that through a specific periodic arrangement in a two-dimensional truss-like structure of materials with different CTEs (Figure 3.1a) the overall response of the structure could have zero CTE at specific points. The thermal expansion of these points is governed by Equations 2.6 and 2.7, for pin-jointed and bonded structures, respectively.

As can be seen in Equation 2.6, the overall CTE of the structure is a function of the ratio of CTEs the constituents and the characteristic angle ϑ. Equation 2.7 takes into account more parameters, but the added parameters do not change the response substantially (discussed in 2.3.2). As shown in Figure 3.1b, this function

vanishes for pairs of values of ϑ and α_2/α_1. Thus by designing a unit cell with specific angle ϑ and picking appropriate constituent materials, it is possible to create unit cells, and consequently full-scale lattices having a final CTE less than that of either constituent.

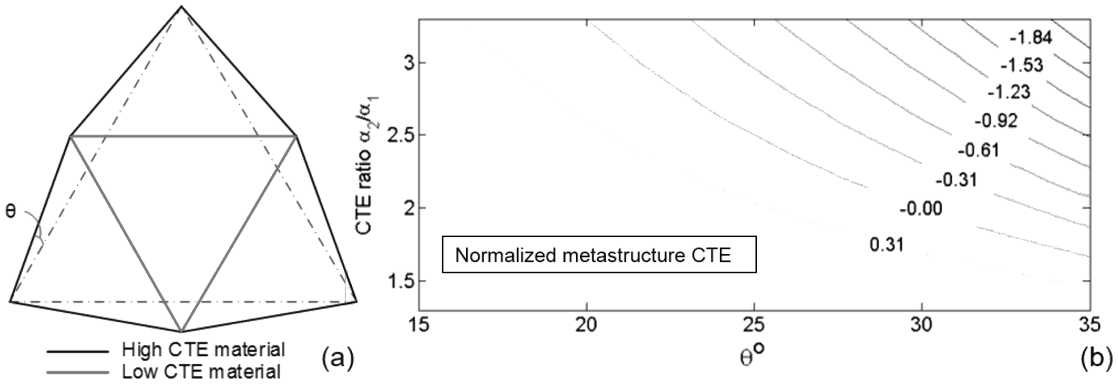

Figure 3.1 (a) Pin-joined structure designed by Steeves [22] consisting of a high and a low CTE material and exhibiting low overall CTE, governed by Equation 2.6. (b) Equation 2.6 plotted for various values of α_2/α_1 and ϑ showing the thermal expansion coefficient of a pin jointed low CTE structure normalized by α_1. It is possible to achieve zero and even negative thermal expansion coefficients by picking appropriate combinations of CTE ratio α_2/α_1 and angle ϑ.

3.1 Design of Unit Cells with Engineered Thermal Expansion

In this work, the unit cell is composed of a low-CTE outer frame (Figure 3.2a) and a high-CTE inner plate (Figure 3.2b) combined to form a low CTE metastructure (Figure 3.2c), as in [23]. However, the unit cells presented here are ~25 times thinner, ~4 times smaller laterally, and have ~6 times higher aspect ratio than those in [23]. Such smaller sizes required the redesign of the interface between the constituent materials, to mitigate fabrication challenges. The interfaces of the two

constituents are lap-jointed and ultimately fabricated by spot laser-welding instead of press fit jointed as in [23].

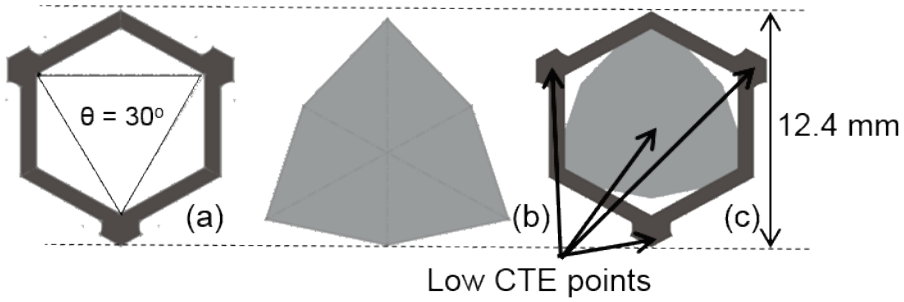

Figure 3.2 (a) Schematic diagram showing the geometrical characteristics of the unit cell's outer frame. ϑ is the angle between the internal unit cell frame angle and the inscribed equilateral triangle. (b) Schematic diagram of the unit cell's inner plate. (c) Schematic diagram of the assembled unit cell.

The plate and frame are joined at three interfaces. These interfaces displace primarily in-plane during thermal loading and cause rotation, but no in-plane displacement, at the low-CTE points (Figure 3.2c). In this design, the characteristic angle ϑ is fixed at 30°. This results in the frame having a regular hexagonal shape, which is advantageous for isotropy in mechanical and thermal response. Unit cell dimensions are as shown in Figure 3.2c with thickness of 125 μm. Lateral dimensions are chosen by taking into account functional, application, and fabrication based constrains. Functionally, it is preferable that the unit cell has a low aspect ratio, and thus smaller lateral dimensions than those in this work. In terms of the specific aerospace applications that are most applicable to this work [63, 64], it is advantageous that the coverage area be maximized, which also suggests smaller lateral dimensions. However, fabrication of metastructures with dimensions smaller than ~12 mm, would result in significant challenges with conventional machining (electron discharge machining) or even the lithography techniques used here (UV photolithography). Thus, in order to demonstrate

scalability to lower scales we chose to fabricate low-CTE metastructures with the dimensions shown in Figure 3.2.

3.2 Computational Study

To understand the behavior of these structures, predict their thermal and mechanical response, and improve upon previous theoretical work, we built realistic FEM models. While previous theoretical and computational work [22, 23] allows for an approximation of the thermal response, it is based on several limiting assumptions: (i) parts are composed of truss members; (ii) the interfaces are point contact; (iii) the interfaces are either pinned or bonded; (iv) it does not take into account out-of-plane effects which are relevant for this design. In addition, it gives little insight into the response of the structure as a function of variables other than ϑ and α_2/α_1. The FEM models developed in this work address the analytical limitations of previous work and enable a sensitivity analysis to material and geometric variables.

3.2.1 FEM Model Formulation

In a general sense, FEM is a method for numerically solving a class of partial differential equations. FEM is composed of four steps: (i) constructing a mesh; (ii) formulating the discrete problem; (iii) solving the discrete problem; (iv) computing variables of interest based on variables calculated during solution of the problem. Constructing a mesh is conducted by breaking up the geometry of the problem to discrete elements. The discreet problem is then formulated by converting the governing equation from its strong form to its weak form and discretizing the weak form. In linear elasticity problems, the strong form and the weak form are mathematically equivalent.

To predict the thermal response of the unit cells designed, we developed planar and full 3D FEM models of the unit cell, using commercial software Abaqus FEA [65]. The mechanics of the unit cell are modeled using static linear elastic analysis. This assumption is accurate for small deformations and linear elastic materials. The validity of this assumption is shown in section 3.2.4. In the model used here, the FEM solves the equilibrium equation by converting it to its weak form and discretizing over elements to arrive to the following formulation for my problem [66]:

$$\mathrm{w}\left\{\sum_{e=1}^{n}(\mathrm{K_e d}-\mathrm{f_e})\right\}=0 \quad \forall \mathrm{w}. \tag{3.1}$$

In Equation 3.1, the weight function, *w,* is an arbitrary function which vanishes on the zero displacement boundary of the problem; *d* is the nodal displacement matrix and subscript *e* refers to a specific element. K_e and f_e are the element stiffness matrix and element external force matrix, respectively:

$$\mathrm{K_e}=\int_{\Omega_e}\mathrm{B_e^T D_e B_e}\,d\Omega, \tag{3.2}$$

$$\mathrm{f_e}=\int_{\Omega_e}\mathrm{N_e^T b}\,d\Omega+\int_{\Gamma_e^t}\mathrm{N_e^T\,t}\,d\Gamma. \tag{3.3}$$

In Equation 3.2, Ω is the geometric volume of the element, B is the strain-displacement matrix, computed by taking the gradient of the shape functions N, t is the traction boundary condition specified by the problem, and Γ is the boundary on Ω on which the traction boundary condition is applied. The displacement boundary condition is naturally applied through the shape functions.

To fully define an FEM problem, we specified the model geometry (Ω), the mesh and element type, the constitutive law (D), and boundary conditions (Γ, t, b, N, B). A boundary condition must be prescribed across the whole boundary of the geometry. In Abaqus FEA, areas not assigned boundary conditions by the user are

assigned to be traction-free by default. Abaqus FEA then defines the stiffness and external force matrices per Equations 3.2 and 3.3 and solves the problem of Equation 3.1 for the nodal displacements, d, using Newton's method [67]. The strain and stress can be computed from the displacement field and constitutive law, respectively.

As with any computational approach, it is important to identify and quantify sources of error in the solution. The major sources of error in an FEM model are of three kinds: (i) due to discrepancies between the model and the physical world; (ii) due to the inherent approximation of discretization in the model; (iii) due to compounding error during arithmetic operations in the solution phase.

Error arising from discrepancies between the model and reality is discussed in the sensitivity analysis section, 3.4. Inaccuracies arising due to discretization can be minimized by selecting an appropriate mesh and are discussed in section 3.2.3 along with a detailed mesh convergence study. Errors of the third kind are generally related to the solver of the FEM software as well as the condition of the problem being studied. In a linear elastic problem, these errors are generally small, will generally not compound, and may produce a consistent (but not growing) discrepancy with the exact solution [66]. Since the problem being studied is linear elastic and the Abaqus FEA software solver has been studied extensively this type of error is not analyzed in depth here.

In the planar mode, to account for the high aspect ratio and low thickness of the structure, we modeled the structure using triangular shell elements (S3R). In the full 3D case, we used 10 node tetrahedral elements (C3D10). Engineering drawings of the as modeled unit cell frame and plate are shown in Appendix A.1. A discussion of leveraging symmetry to improve computational efficiency is discussed in section 3.2.5. The interfaces between the plate and the frame are 396.6 μm diameter circles

and are modeled as bonded by using *tie constraints* in Abaqus. This method was used to simulate the way that the two parts would be joined experimentally; i.e., by welding.

The main simplification of the planar model is that the two constituent parts of the unit cell are modeled in the same plane, whereas the 3D model fully captures the geometry of the metastructure. To measure the CTE of the unit cell we computed displacements under a simulated thermal load of 80 ^{o}C. Displacement and rotation at the node of the unit cell corresponding to the centroid of the lower face of the inner plate was constrained in all directions to prevent rigid body motion. The node at the centroid of the upper face was constrained from in-plane displacement to prevent rigid body rotation. The remaining part of the surface geometry was set to a thermal load of 80 ^{o}C. Post-processing, we calculated the CTE of the unit cell by measuring the expansion of the low-CTE points. In order to understand the response of the metastructure as well as the limitations of this design approach, we studied its thermal response as a function of two design variables: (i) the ratio of CTEs of the constituents; (ii) the frame width normalized by the length of the unit cell (12.4 mm). We consider CTE ratios between 1.75 and 2.75. This range is important because the CTE ratio of most metals is below 2.75 (Table 3.1) [68], while when considering ratios less than 1.75, the CTE of the unit cell is larger than desired. As seen in Figure 3.1b, the CTE ratio has a significant effect on the unit cell CTE, as predicted by Equation 2.7. To study the effects of the unit cell's geometry, we modeled frames with normalized widths between $3.84\text{x}10^{-2}$ (476 μm frame width) and $10.97\text{x}10^{-2}$ (1.36 mm frame width). These widths ratios were selected based on bounds imposed by fabrication constraints on the lower end and the resulting CTE of the unit cell on the high end.

Material	CTE (ppm/°C)
Aluminum	23.1
Beryllium	11.3
Gold	14.2
Iron	11.8
Lead	28.9
Magnesium	24.8
Nickel	13.4
Tantalum	6.30
Titanium	8.60
Zinc	30.2
Zirconium	5.70

Table 3.1 CTE of common pure metals [68]

3.2.2 Computational Results

The 3D FEM predicts higher CTE for the unit cell than the planar FEM model, while both models predict that the CTE is a function of the constituents' ratio and the frame width. For a unit cell composed of constituents with CTE ratio of 2.7, and frame width of 814 μm (the design that was experimentally implemented and discussed in section 3.3), the planar FEM model predicts a CTE of 0.6 ppm/°C, while the full 3D FEM model predicts a CTE of 1.19 ppm/°C. As shown in section 3.3, the full 3D FEM prediction agrees more closely with experimental results.

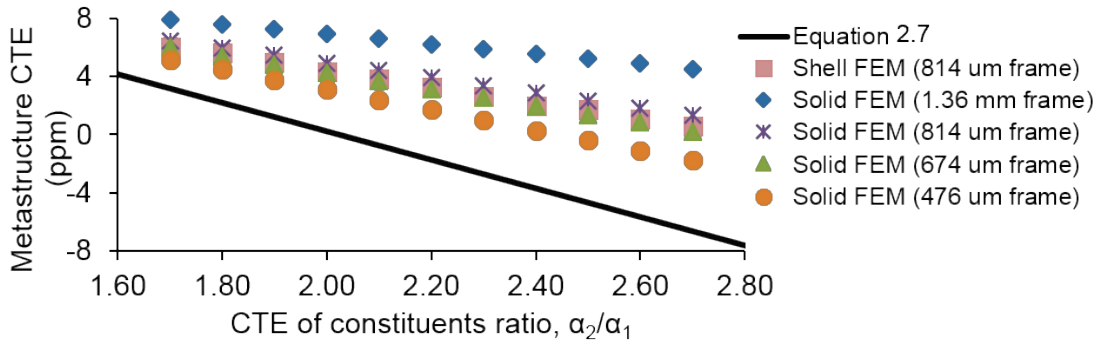

Figure 3.3 The CTE of the unit cell as predicted by FEM for various CTE ratios α_2/α_1. The solid line indicates the prediction of Equation 2.7. The circular, triangular, star, and rhomboidal symbols indicate the FEM prediction of a unit cell design with frame width ratios of $3.84\text{x}10^{-2}$, $5.44\text{x}10^{-2}$, $6.56\text{x}10^{-2}$, and $10.97\text{x}10^{-2}$, respectively. The square symbols indicate the planar FEM prediction of the $6.56\text{x}10^{-2}$ frame width ratio unit cell. The full 3D solid FEM model predicts a higher CTE for the unit cell than the planar FEM model.

As the normalized width dimension increases, the CTE of the unit cell increases. This is due to increased resistance in the bending of the frame. Furthermore, it is evident from Figure 3.3 that Equation 2.7 is not an accurate approximation for the CTE of the unit cell. This is due to violation of the assumption that the frame's beams behave like truss-like structures. This presents a design trade-off as the frame beams need to be wide enough to support structural loads, but the ratio of CTEs of the constituent materials need to be small to prevent significant dissimilarities between the two materials which would result in fabrication challenges. In the final design selected for experimental testing, the normalized frame width is $6.56\text{x}10^{-2}$ (814 μm frame width). We chose this frame width as it results in a design with the lowest beam width still ensuring structural stability of the structure, scalability to smaller scales, and fabrication feasibility in the current scale. The existing theoretical framework for these metastructures treats all constituent materials as beams. In this work, we computationally compare the

response of a metastructure consisting of all beam elements (as in the theoretical framework) and of one with a plate interior constituent, using FEM. Detailed analysis shown in section 3.2.3 yielded negligible difference in the thermal response of the two unit cells.

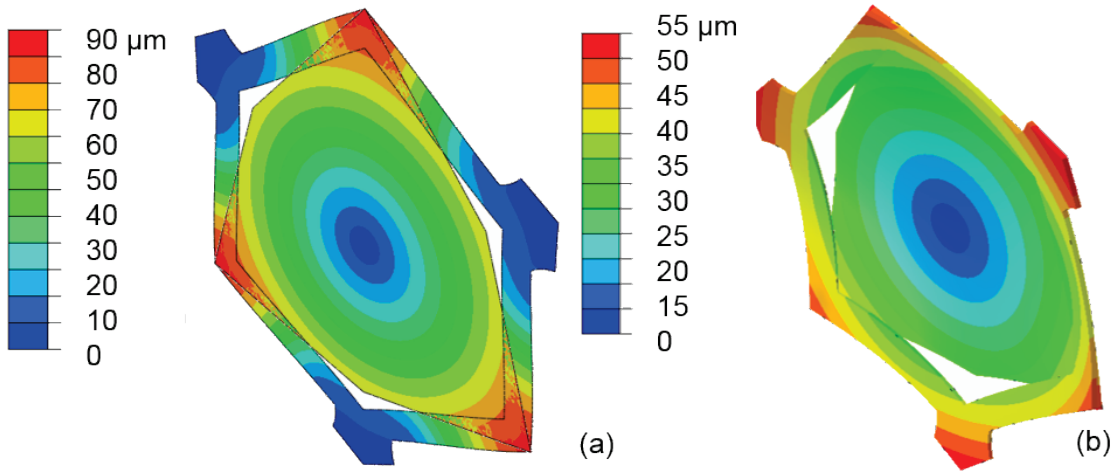

Figure 3.4 Isometric view of the shape of an exemplary unit cell as predicted by planar (a) and 3D (b) FEM with an 80 °C thermal load. Contours show the magnitude of the displacement vector. The out-of-plane deformation predicted by the 3D FEM case is evident in panel b. Displacements are magnified 40 times in (b).

In addition to in-plane geometrical effects, out-of-plane deformation is particularly important to this design. Figure 3.4 shows the magnitude of the displacements in as-designed unit cells with the planar FEM (a) and 3D FEM (b) models. The thin scale and relative out-of-plane attachment of the constituent parts can induce out-of-plane deformation on the cells. Out-of-plane displacement is clearly visible in Figure 3.4b. In this scenario, the out-of-plane response of this metastructure is critical to the performance of the optics. Figure 3.5a shows the maximum out-of-plane deformation induced during thermal loading as a function of unit cell thickness, as predicted by 3D FEM. As the thickness decreases, the out-of-plane

deformation increases, exhibiting the importance of out-of-plane effects at thinner scales.

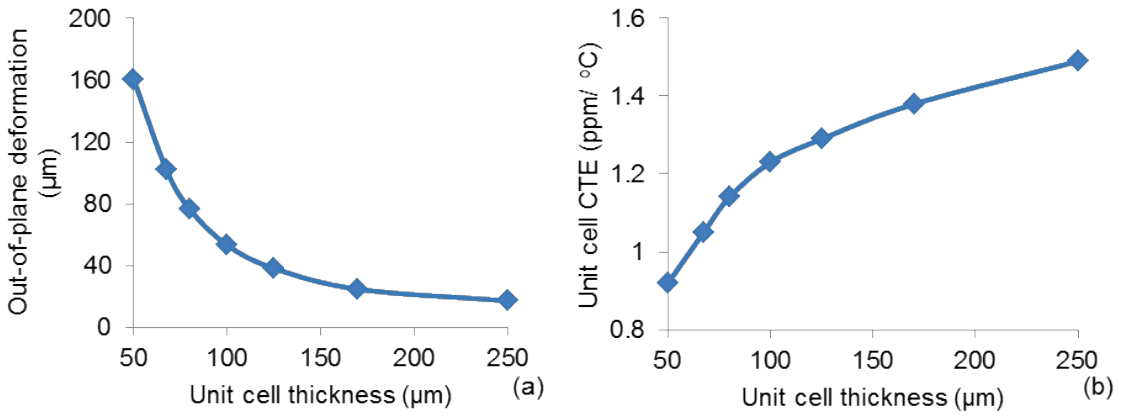

Figure 3.5 (a) The maximum out-of-plane deformation of a unit cell as a function of the unit cell's thickness. The maximum out-of-plane deformation occurs at the frame's low CTE points. (b) The CTE of a unit cell as a function of the unit cell's thickness. There is a measurable decrease in the CTE as the thickness decreases.

Figure 3.5b shows the effect of thickness on the CTE of the unit cell. As the thickness increases from 50 μm to 250 μm the CTE also increases, from 0.92 to 1.49 ppm/°C. The dependence of CTE on thickness suggests that the out-of-plane deformation has a measurable impact on the CTE of the metastructure. However, this impact is small and does not influence the low-CTE performance of the metastructure.

3.2.3 Mesh Convergence and Comparison with the Theoretical Solution

In order to minimize numerical errors and optimize computational cost, we performed a mesh convergence study using the h-refinement technique [69] as well as an error and computational cost analysis. In the h-refinement technique, the mesh density is increased while the element type is kept the same until the solution

converges to a value independent of discretization choice. For this study, we modeled the response of a unit cell under a thermal load of 80 °C. Models were made with increasing mesh densities using quadratic C3D10 elements. Quadratic elements provide a one order of magnitude lower error for a given element size compared to linear elements [66]. Once a convergence was achieved the mesh was optimized by lowering the mesh density in areas of low stress to increase computational efficiency, resulting in the mesh shown in Figure 3.6a.

Figure 3.6 shows three exemplary mesh grids used in the convergence analysis, the optimized mesh (Figure 3.6a), the most refined mesh (Figure 3.6b) and the least refined mesh (Figure 3.6c). Both the L_2 norm (defined in Equation 3.4) of principal stresses and L_2 norm of strain energy converge to values independent of discretization for the most refined mesh. The optimized mesh maintained the same level of precision for the areas of interest, while improving computational cost. The computational cost for these simulations was relatively light, ranging from 46 CPU seconds for the least refined mesh and 322 CPU seconds for the most refined mesh. However, computational cost becomes significant when simulating full scale arrays of unit cells (chapters 4 and 5).

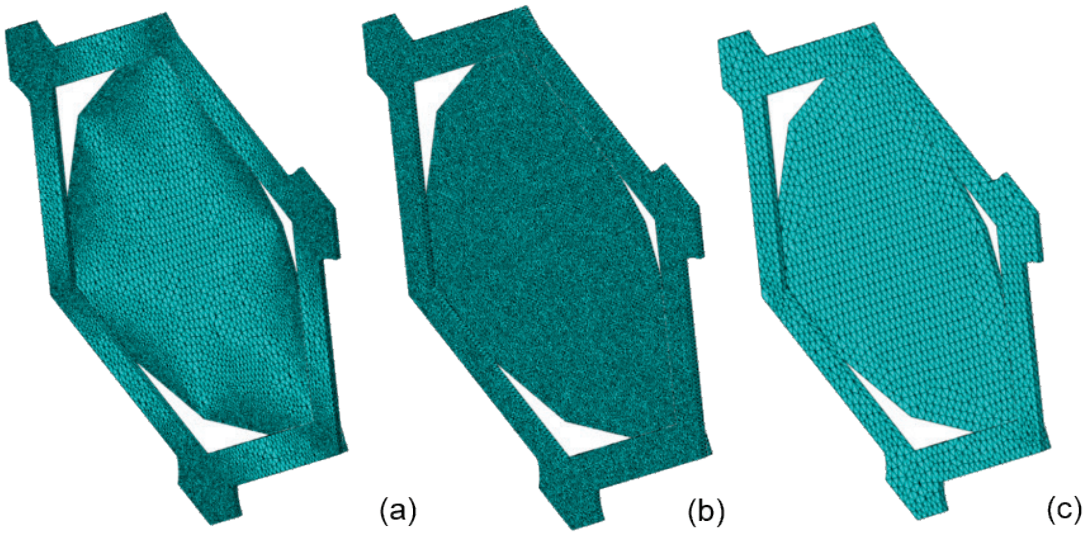

Figure 3.6 Unit cells used in my 3D FEM mesh convergence analysis. The optimized mesh, ultimately used in the model, (a) contains 66,489 nodes and 37418 elements for the frame part and 80,740 nodes and 45,169 elements for the plate part; the most refined mesh (b) contains 72,518 nodes for the frame part and 41,662 elements and 137,873 nodes and 81,331 elements for the plate part; the least refined mesh (c) contains 8,706 nodes and 3,972 elements for the frame part and 13,787 nodes and 6,776 elements for the plate part. All elements are quadratic C3D10.

The L_2 norm of the principal stresses and the strain energy over the entire volume was used as the metric to quantify mesh quality. The L_2 norm of a function is a way of defining the magnitude of a function *f(x)* and is given by:

$$\|f(x)\|_{L_2} = \left(\int_{x_1}^{x_2} f^2(x)\, dx\right)^{1/2}. \tag{3.4}$$

The L_2 norm is a useful way to compare quantities which vary as a function of space. Figure 3.8 shows the results of the mesh convergence analysis. Convergence to the limit solution is observed in both the L_2 norms of principal stresses (Figure 3.7a) and strain energy (Figure 3.7b) for sufficiently refined meshes.

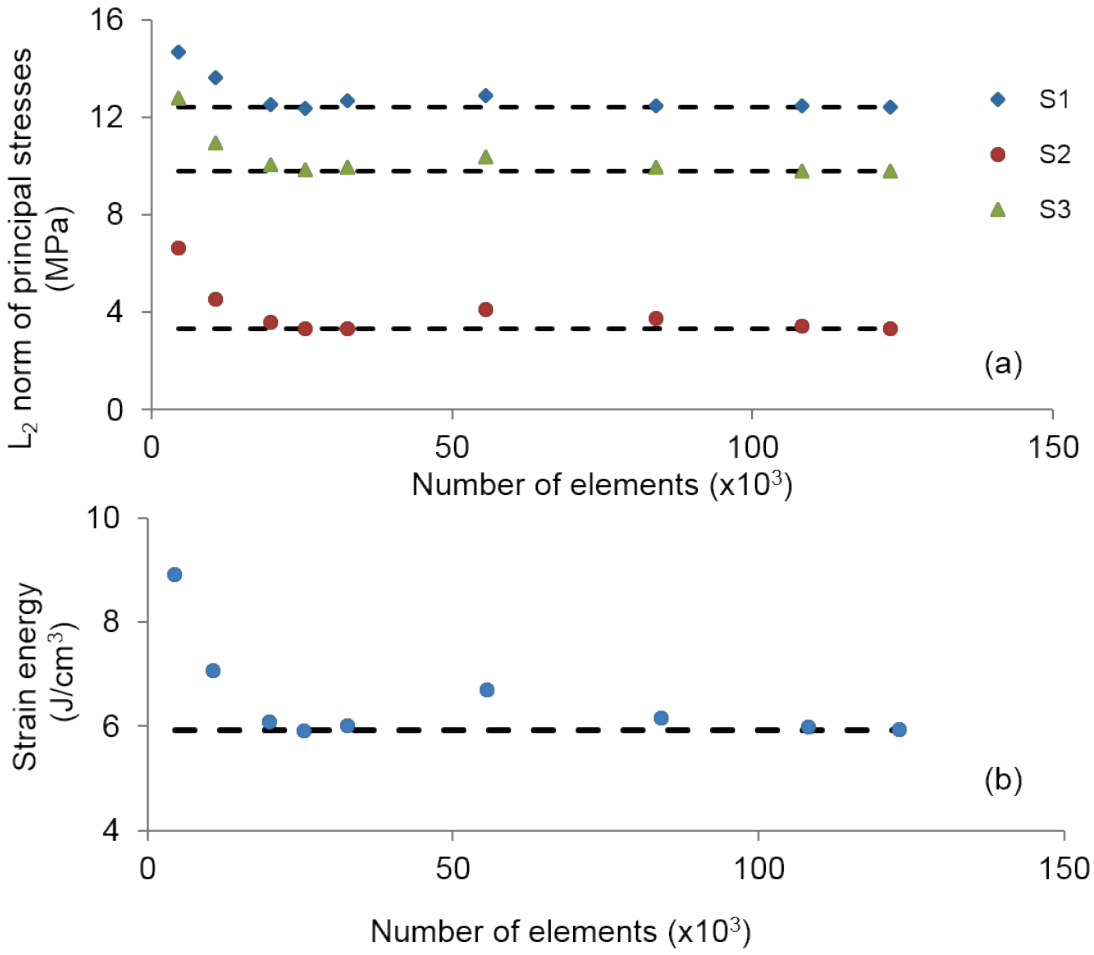

Figure 3.7 Comparison of the L_2 norms of (a) principal stresses and (b) strain energy as a function of increasing mesh density. In panel (a) the blue rhomboidal symbols represent the maximum principal stress, the red circular symbols represent the middle principal stress, and the green triangular symbols represent the minimum principal stress. Convergence to a discretization independent value is observed in principal stresses and strain energy for a sufficiently dense mesh.

Thus, to confirm the accuracy of the model, it now suffices to show that the FEM predicts the same thermal behavior as an exact solution. However, an exact solution cannot be obtained for the problem presented here by theoretical means. Previous work [22, 23] predicts the CTE of such metastructures under several limiting

assumptions (Equation 2.7). While a thorough discussion of these assumptions is presented in section 2.3.2, the three most relevant assumptions are: (i) structural elements behave like rods; (ii) the contact area is of infinitesimal size; and (iii) the structure undergoes purely in-plane deformation. To test the validity of my FEM model we modified the structure and model parameters in order to meet the three assumptions. Figure 3.8a shows the unit cell simulated to verify the FEM's model accuracy. While the basic design was kept the same, features that could cause deviation from the theoretical result were removed and all structural elements were designed in order to behave like truss members (assumption i).

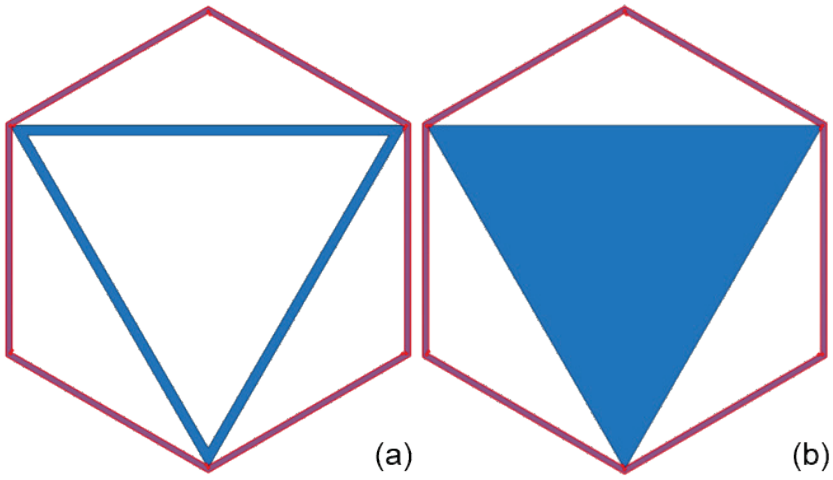

Figure 3.8 (a) Simulated structure designed to be consistent with the assumption of truss-members and exhibit only in-plane behavior; (b) structure in which the outer material (shown in red) is designed to behave like a truss-member, but the inner material behaves like a plate. The only difference between the structure in (a) and in (b) is the geometry of the inner constituent shown in blue.

The interface between the two parts was minimized as much as practically possible in area and modeled as bonded using "tie constraints" (assumption ii). Finally, to limit any out-of-plane effects (assumption iii), the parts were modeled as shells in

the same plane. The CTE of the unit cell was measured for various ratios of CTE constituents by performing a similar analysis as in 3.2.1. In addition, the effect on thermal response of the inner constituent being a plate, as opposed to a rod (which the theory assumes) was assessed by computing the CTE of the unit cell shown in Figure 3.8b. Figure 3.9 shows the comparison between theoretical predictions of the CTE and the FEM model developed in this work. Excellent agreement is observed between the theory for bonded parts and the model. It is also evident that changing the inner constituent (shown as blue in Figure 3.8) from a rod to a plate does not significantly influence the CTE of the unit cell.

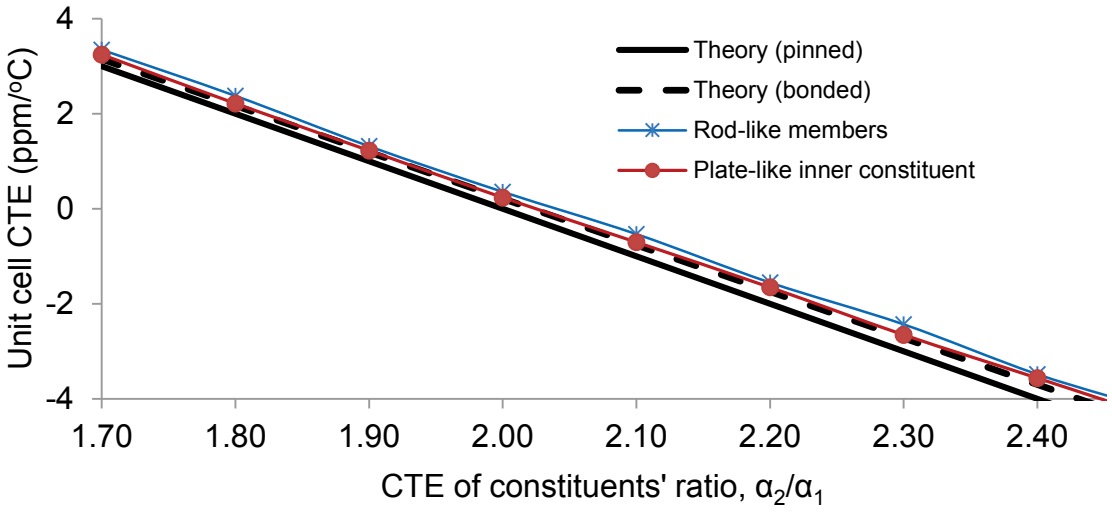

Figure 3.9 Comparison between theoretical predictions of the unit cell CTE as a function of CTE of constituents' ratio and FEM model developed in this work. The solid line corresponds to a theory assuming pin-jointed structures, while the dashed line shows the theory for bonded structures. The FEM predictions for a structure with rod-like members and a structure with plate-like inner constituents are shown with blue asterisks and red circles, respectively.

In fact, when the inner constituent can be assumed to behave like a plate, the CTE of the overall structure is slightly lower than when it behaves like a rod. This can be attributed to the increased stiffness of the plate.

The excellent agreement between the theory and the model when the model is simplified to the theoretical limits confirms the viability of the FEM model in this work and enables predictive use of this model.

3.2.4 Validity of the Linearity Assumption

The model developed in this work and formulated in section 3.2.1 assumes linearity, i.e., the response is a linear function of the input variable over the range of interest. This assumption is valid when the material constitutive law is linear and when deformations are "small". In this work, material properties are assumed linear over the range of interest. To verify that displacements are indeed small, theoretical and computational analyses were performed.

For the theoretical analysis, the unit cell was assumed to behave like a bimetallic strip. It can be shown that the curvature, $\varkappa$, of a bimetallic strip under thermal loading is expressed by [59]:

$$\kappa = \frac{1}{\rho} = \frac{48}{33}\frac{(\alpha_2-\alpha_1)(\Delta T)}{h}. \tag{3.5}$$

In Equation 3.5, α_2 and α_1 are the CTEs of two materials, h is the thickness of the strip and ΔT is the temperature difference experienced by the strip. Equation 3.5 assumes that the two materials of the bimetallic strip have the same thickness and disregards the effect of the materials' elastic moduli (the effect can be shown to be less than 3% even when the elastic modulus ratio is $\frac{1}{2}$). The deflection can be evaluated from the curvature by recognizing that the deformed bimetallic strip of length L forms a circular arc (Figure 3.10).

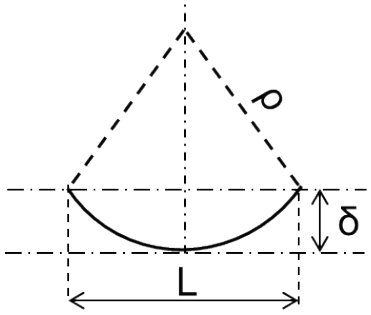

Figure 3.10 Deflection, δ, of a bimetallic strip of length L, and radius of curvature ρ.

Thus the deflection δ is expressed by:

$$\delta(2\rho - \delta) = \left(\frac{L}{2}\right)^2. \tag{3.6}$$

This expression can be linearized to $\delta = \frac{L^2}{8\rho}$ provided that $2\rho\delta \gg \delta^2$; i.e., the deflections are small compared to the radius of curvature. To test this linearity assumption we compare 2ρ and δ. We can compute δ by solving 3.6 for δ:

$$\delta = \frac{2\rho \pm \sqrt{4\rho^2 - L^2}}{2}. \tag{3.7}$$

In Equation 3.7, the negative value of the square root is taken since δ must be smaller than ρ. Figure 3.11 compares 2ρ and δ for a range of values of bimetallic strip L and change in temperature ΔT. In Figure 3.11, the CTEs of the two materials, α_1 and α_2, were set to 23.1 and 8.6 ppm/ °C and the bimetallic strip height, h, was set to 0.25 mm.

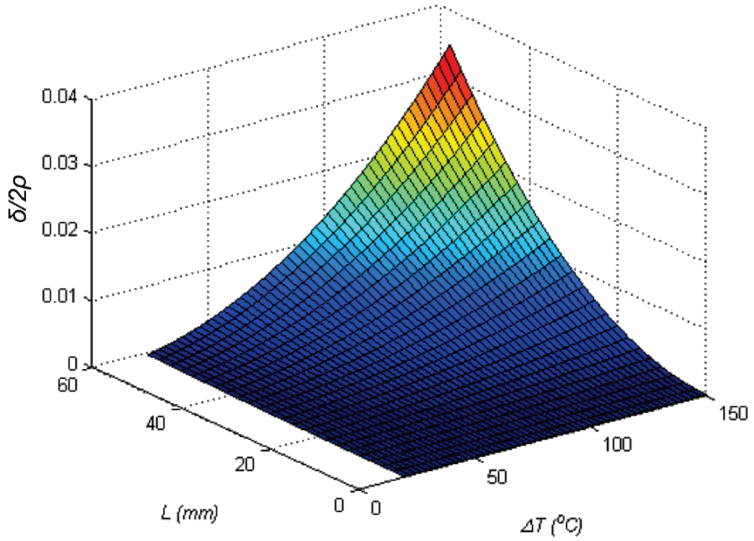

Figure 3.11 Ratio of bimetallic strip deflection δ and twice the radius of curvature ρ for a range of values of bimetallic strip length L and change in temperature ΔT. The assumption $2\rho\delta \gg \delta^2$ remains accurate over the range of values shown.

As Figure 3.11 shows, the assumption that $2\rho\delta \gg \delta^2$ is accurate for strip lengths at least up to 60 mm (unit cell studied here is ~13 mm long) and temperature differences at least up to 150°C. Furthermore, the bimetallic strip assumption is a conservative (upper) estimate of the out-of-plane deflection of the unit cell since in the unit cell the two materials are not in full contact. Based on this analysis, the linearity assumption is valid for the unit cell under the conditions studied.

The linearity assumption and quality of the bimetallic strip model were further evaluated using FEM. The out-of-plane behavior of the unit cell studied here was modeled with linear and fully nonlinear FEM and compared with the theoretical prediction (Figure 3.12).

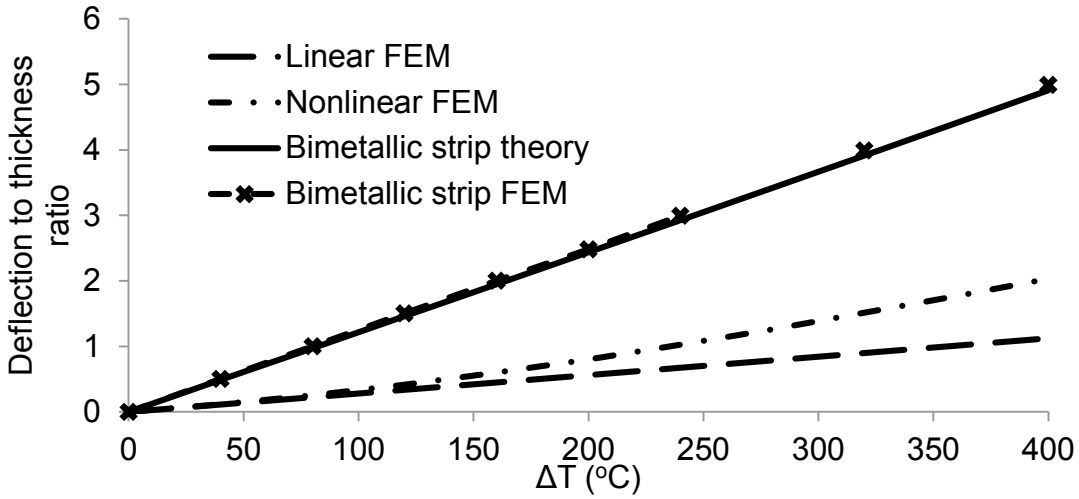

Figure 3.12 Comparison between linear FEM, nonlinear FEM, and the bimetallic strip theory for the deflection of a low CTE unit cell normalized by its thickness. Linear FEM is a good approximation until at least $\Delta T = 80^{o}C$, while the bimetallic strip theory provides an upper bound for the deflection.

The bimetallic strip theory predicts deflections between two and four times higher than the FEM and as predicted, provides an upper bound for the deflection of the unit cell studied here (Figure 3.12). By comparison with nonlinear FEM, the linearity assumption is confirmed for values up to least $80^{o}C$ ΔT. The linear assumption significantly deviates (~25% error) for normalized deflections greater than 0.25. This analysis provides a more stringent bound than the convention used in industry where deflection for a plate in bending can be described as "small" when it is smaller than half the thickness of the plate [70]. In this work, nonlinearity will be assumed whenever deflections are greater than 25% of the plate thickness.

3.2.5 Symmetric Boundary Conditions on the Unit Cell

While a full 3D FEM model analyzes the exact geometry of a structure with no simplifications or artificial boundary conditions, it is often advantageous to reduce

the size of the problem being modeled by leveraging symmetries. The reduced model should output the same solution as the full model but at reduced computational time. The unit cell in this work exhibits two-fold, three-fold, and six-fold symmetry. Figure 3.13 shows the full unit cell (a) and its equivalent symmetric models (b,c,d).

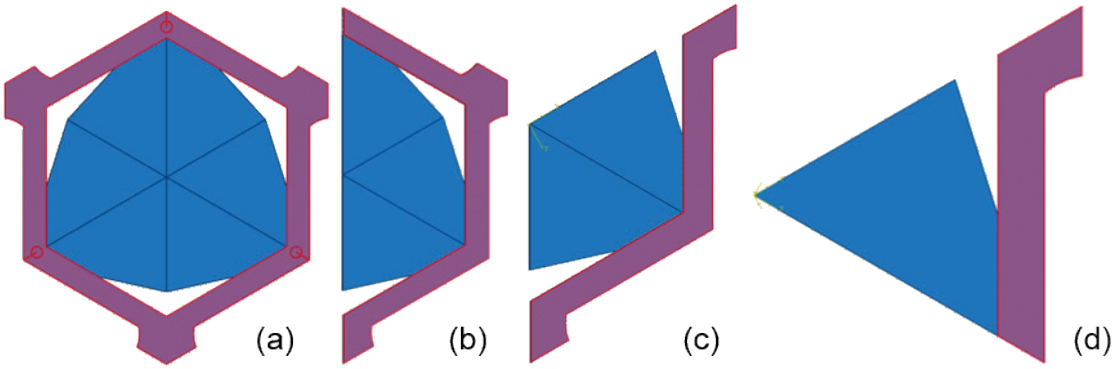

Figure 3.13 (a) Full unit cell model; equivalent unit cell model leveraging two-fold (b), three-fold (c), and six-fold (d) symmetry.

The equivalence of the symmetric models with the full unit cell was verified by computing the deflection of the unit cell for linear and nonlinear FEM (Figure 3.14a). The difference in results between the full unit cell and the symmetric equivalents was negligible. However, computational efficiency is significantly improved when reducing the model size by symmetry (Figure 3.14b). Computational efficiency is more significant in simulating lattices of unit cells, as in later chapters. In the case of lattices, it will be shown that the two-fold symmetry is the highest form of symmetry.

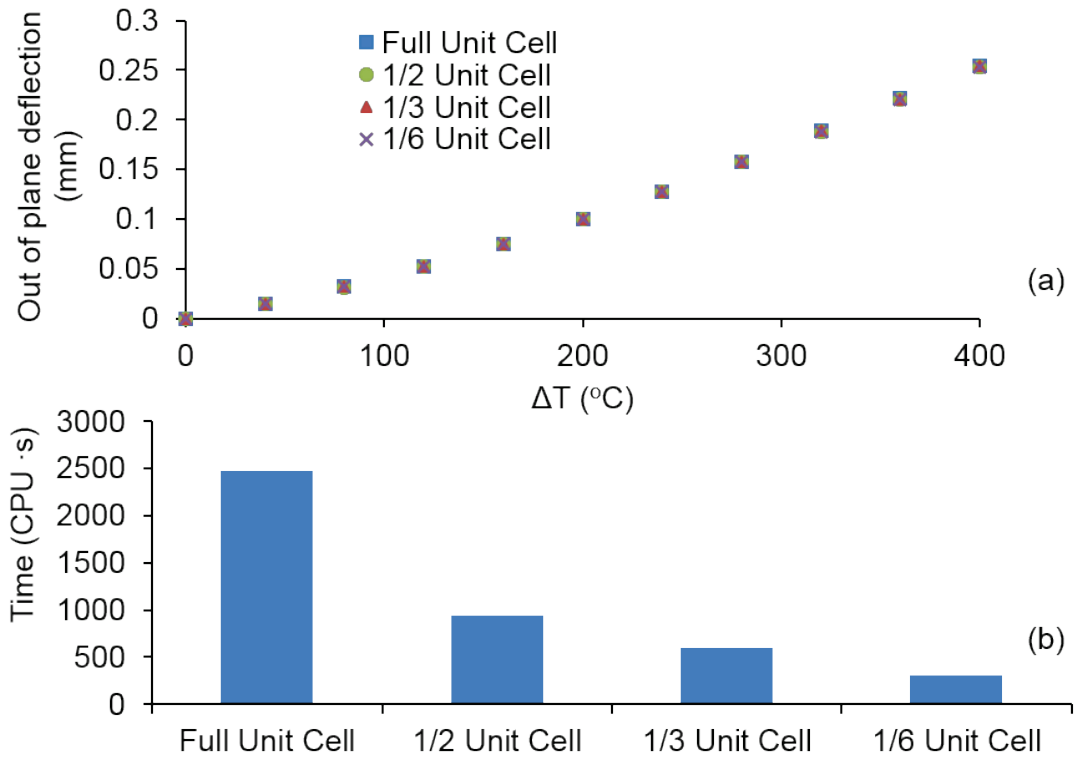

Figure 3.14 Comparison between modeling a full unit cell and its symmetric equivalents in (a) out-of-plane deflection; and (b) computational time.

3.3 Experimental Study

With the final design determined through FEM analysis, we proceeded to experimentally show that this metastructure indeed behaves as predicted. While we show metastructures achieving different (and even negative) values of CTE in Chapter 4, here, we focused on showing near-zero CTE, as proof of principle. Thus, based on Figure 3.3, we chose to experimentally realize this design with two materials whose CTE ratio is about 2.7. Based on their CTE ratio and mechanical robustness, we fabricated the outer frame out of Titanium ($\alpha_{Ti} = 8.6$ ppm) and the inner plate out of Aluminum ($\alpha_{Al} = 23.1$ ppm) [68].

3.3.1 Sample Preparation

We fabricated and prepared samples for testing in three steps: (i) fabricate the Ti frame and Al plate separately; (ii) attach the two pieces at three points; (iii) add speckle pattern for Digital Image Correlation [71, 72] testing. Frame and plates were fabricated using wire electron discharge machining (EDM). Figure 3.15a shows a unit cell after the laser welding step, but before the speckle pattern has been applied. Following fabrication the two parts were cleaned and attached at three points by laser welding (Figure 3.15b). Laser welding was performed with a 50 W maximum power pulsed Nd:YAG laser. The power and frequency were adjusted such that the laser beam melted the titanium, which has a higher melting point than aluminum (1941 K vs. 933 K), but did not go through to the aluminum. Instead, the molten titanium at the interface with the aluminum melted a region of aluminum which resulted in the weld. During the laser welding process, the laser beam was normal to the sample while Argon gas was used to remove oxygen from the weld area.

To characterize the laser welding process, we measured the size of the weld for a series of Al/Ti welds. As can be seen in Figure 3.15b, the weld area consists of an inner circular area which corresponds to coalescence of the two materials and an outer area which encompasses the material deformed during the weld process. The material in the outer area exhibits wrinkles, likely due to buckling as a result of compressive stress developed as the inner area was heated during welding. The average inner and outer weld diameters were 400 μm and 894 μm, respectively. Finally, we added the speckle pattern by first painting the sample white and then adding black speckles by using Krylon Flat White and Flat Black spray paint, respectively.

From a random sample of speckles, the average speckle size was 26.97 pixels. Approximately half of the speckles contained less than 20 pixels and 40% of speckles contained 10-20 pixels. The size was controlled by changing the distance from which black spray paint was applied. The speckle size must be large enough to prevent aliasing but small enough that the correlation algorithm can accurately track the speckle subsets.

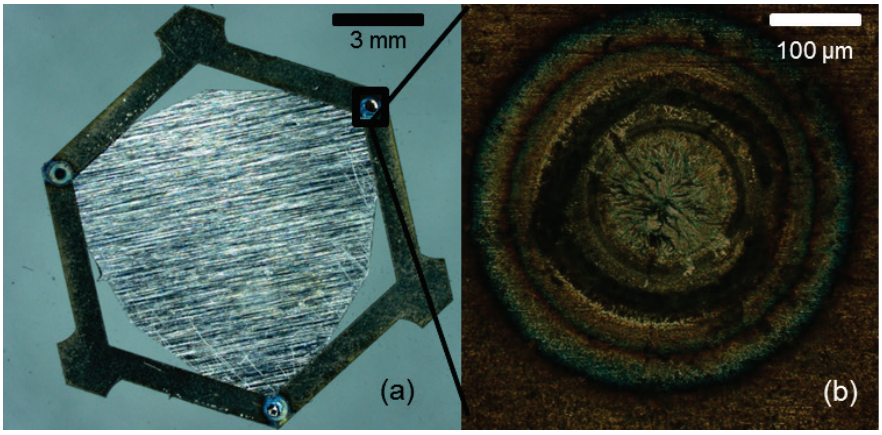

Figure 3.15 (a) Fabricated low CTE sample comprised of an Al inner plate and a Ti outer frame. (b) Laser-welded interface between the sample's Al and Ti part.

3.3.2 Experimental Setup

We experimentally measured the CTE of the samples by heating them and measuring displacements using digital image correlation (DIC) [71, 72]. The DIC algorithm tracks the speckle pattern by performing a correlation on the greyscale values of "subsets" (groups of pixels) between the deformed and undeformed images. Based on the correlation, displacements are computed at specific pixels, with the resolution determined by the "step" size (e.g., with a step size of 1, displacements are computed at every pixel). If the step size is too high, spatial resolution is lost; if it is too low, noise is introduced to the displacement field. Subsets in this work

were composed of 21 pixels and the step size was five pixels. This resulted in a ~50 μm spatial resolution and a correlation displacement accuracy of ~500 nm. The correlation accuracy corresponds to ~5% of the maximum displacement observed. The 50 μm spatial resolution is adequate to capture the overall deformation behavior of the ~12 mm sample.

A similar experimental setup to the one used here is discussed in detail in section 4.1. The samples were heated on a hot plate and the temperature was measured using a thermocouple and a resistance temperature detector. Images were taken once the temperature had stabilized at steps between 40 °C and 160 °C using a Nikon ShuttlePix P-400R microscope. We then computed the displacements at each temperature step using commercial VIC-2D [73] software.

3.3.3 Measurement of the Thermal Expansion Coefficient

We observed agreement between the deformation predicted by our full 3D FEM model and the experimentally tested samples (blue areas in Figure 3.16). The four thermally stable areas predicted by the FEM models (shown in blue in Figure 3.16a,b) agree very well with the low CTE areas in the experiments (Figure 3.16c). The experimental data shows slight variations between the deformations at the welds, due to sample fabrication defects.

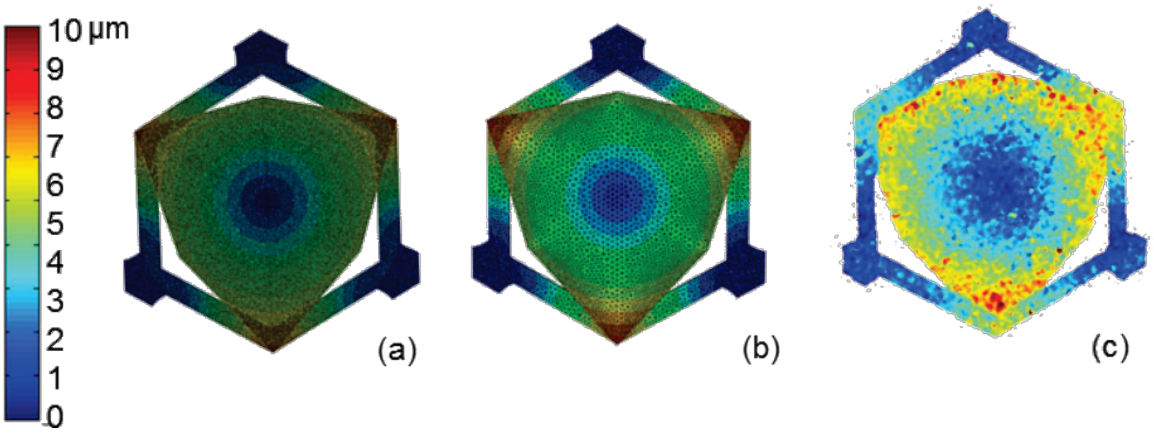

Figure 3.16 Magnitude of in-plane deformation predicted for a 70°C change in temperature by (a) planar FEM, (b) 3D FEM, and (c) experimentally observed between 55 °C and 125 °C. Colder color tones represent regions of the unit cell with low thermal expansion.

To validate my experimental setup we measured the CTE of the fabricated Al and Ti parts by themselves. As shown in Figure 3.17, we measured the CTEs of Al and Ti to be within 2.2% and 1.6% of values reported in literature [68], respectively. We measured our metastructures to have CTE of 2.56 ppm/°C (Figure 3.17). In Figure 3.17, specifically for the unit cell, error bars with horizontal caps indicate one standard deviation in measurement of the CTE error, while error bars without horizontal caps indicate the predicted effect a 5% measurement error in Al CTE, Ti CTE and frame width would have on the unit cell CTE.

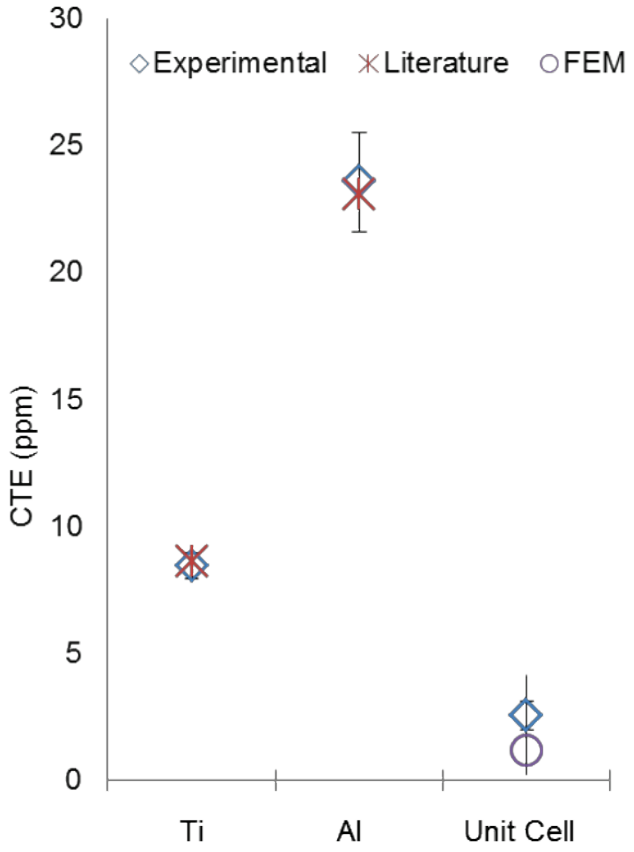

Figure 3.17 CTE of Ti, Al, and unit cell samples as measured by our setup. Error bars indicate one measurement standard deviation for Al and Ti.

3.4 Predicting and Engineering the Coefficient of Thermal Expansion through Sensitivity Analysis

To demonstrate CTE tunability with this design, establish the effect of measurement error on our experimental results, and determine the sensitivity of the CTE to its dependent variables, we performed a sensitivity analysis on the CTE as a function of six parameters: the CTEs and elastic moduli of the constituents (α_1 , α_2, E_1, E_2) and the width of the frame (f_{width}) and the size of the welded contact area ($A_{contact}$). The frame width and contact area were normalized

by the unit cell length (as shown in Figure 3.2c) to allow scaling. The welded contact area is neither a pivot nor a point contact, as assumed in Equation 2.7. Thus, some deviation from the CTE predicted by Equation 2.7 is expected. To assess the effect of the bending induced by the welded area, we analyze the sensitivity of the CTE to the contact area and frame width, in addition to the material properties. The sensitivity analysis indicated that a 5% measurement error in the CTE of the materials, and frame width can lead to significant error in the unit cell CTE. This is shown as the error bars without horizontal caps on the unit cell in Figure 3.17. Figure 3.18 shows the CTE of the unit cell as a function of frame width and the CTE of the inner plate constituent material. By varying those two parameters, it is possible to tune the CTE of the unit cell from -0.5 to 1 ppm/^{o}C.

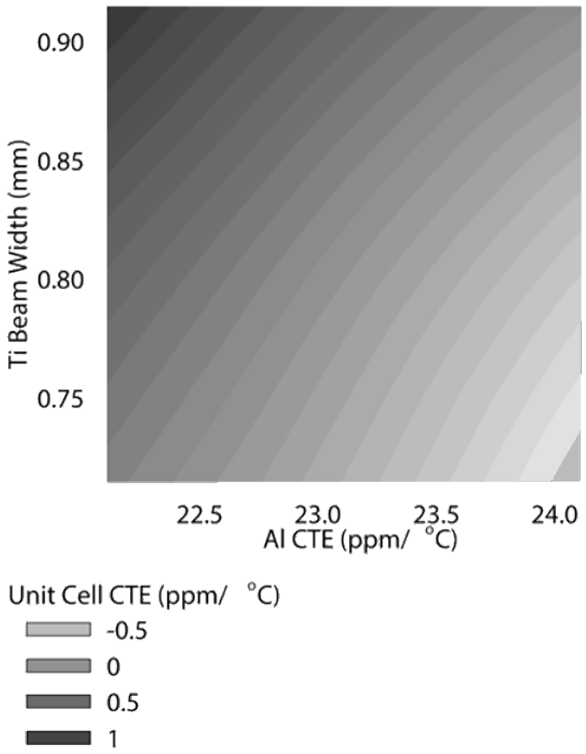

Figure 3.18 Unit cell CTE as a function of frame width ('y' axis) and CTE of constituent material ('x' axis). The unit CTE can range from -0.5 to 1 ppm/°C ppm by adjusting the CTE of one of its constituents and the width of the other constituent.

The sensitivity analysis was performed by running planar FEM simulations and computing the unit cell CTE by varying the six parameters: α_1 from 7.6 to 9.6 ppm, α_2 from 22.1 to 24.1 ppm/°C, E_1 from 106 to 126 GPa, E_2 from 60 to 80 GPa, f_{width} from 5.77×10^{-2} to 7.38×10^{-2} μm/μm, and $A_{contact}$ from 8.06×10^{-3} to 24.2×10^{-3} μm/μm. Commercial data analysis software JMP [74] was used to determine the simulations necessary in order to obtain enough data for data regression and model generation. Forty six simulations were used to generate a data set of unit cell CTE as a function of each of the six parameters mentioned above. The correlation coefficient, *r*, which is a measure of the linear dependence between two variables,

of each of these variables and the unit cell CTE was computed in the following way:

$$r = \frac{1}{n-1}\sum_{i=1}^{n}\left(\frac{X_i-\overline{X}}{S_x}\right)\left(\frac{Y_i-\overline{Y}}{S_y}\right). \tag{3.8}$$

In Equation 3.8, $\overline{X}$ and $\overline{Y}$ are the sample and response means, and S_x and S_y are the sample and response standard deviations, as defined in Equations 3.9 and 3.10 below:

$$\overline{X} = \frac{1}{n}\sum_{i=1}^{n} X_i, \tag{3.9}$$

$$S_x = \sqrt{\frac{1}{n-1}\sum_{i=1}^{n}\left(X_i - \overline{X}\right)^2}\ . \tag{3.10}$$

The dataset used to compute the correlation coefficient is shown in Appendix A.2.

Table 3.2 shows the correlation of unit cell CTE with the six parameters. As expected, the strongest correlation is observed with the CTEs of the constituents. However, while theoretical work predicts that the unit cell thermal expansion depends equally on the CTE of the constituents, the sensitivity analysis shows a much stronger correlation on the CTE of the frame. This is likely attributed to the finite width of the frame which the theory does not take into account. Also strong correlation of the unit cell CTE is observed on the width of the frame. The Young's moduli of the two materials and the contact area between them do not have a strong correlation with the CTE.

α_1	α_2	f_{width}	$A_{contact}$	E_1	E_2
0.89	-0.33	0.29	0.04	0.03	-0.05

Table 3.2 Correlation coefficient between unit cell CTE and design parameters.

Since α_1, α_2, and the frame width (f_{width}) are the most important parameters influencing the CTE of this metastructure, we conducted a series of full 3D FEM simulations to determine the effect of these variables on the CTE. Statistics programming language R [75] was used to produce a multivariate fit of the CTE on those three variables. The multivariate fit performed is a linear, least squares regression and results in an expression of the unit cell CTE as a linear function of the six parameters. Give a dataset of inputs X**,** and response variable y, the least squares regression takes the following form:

$$y = Xb + \varepsilon. \tag{3.11}$$

In Equation 3.11, b is computed to minimize $\boldsymbol{\varepsilon}$ and yield the coefficients linking the response variable to the input as follows:

$$b = (X^T X)^{-1} X^T y. \tag{3.12}$$

Performing the least squares calculation on the dataset shown in Appendix A.2, yields the following regression for the unit CTE:

$$\alpha = -4.263 + 1.689\,\alpha_1 - 0.646\,\alpha_2 + 87.945\,f_{width}. \tag{3.13}$$

In Equation 3.13, α_1 and α_2 are in ppm, f_{width} is in μm/μm, and the output α is expressed in ppm/°C.

Figure 3.19 presents a comparison between the CTE predictions of Equation 2.7, Equation 3.13, the planar and 3D FEM models developed in this work, and the experimental results.

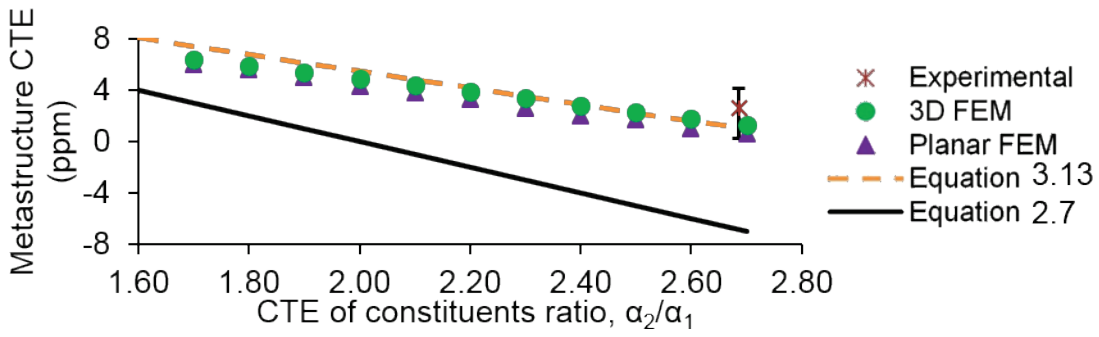

Figure 3.19 A comparison for the CTE prediction between Equation 2.7 (solid line), Equation 3.13 (dashed line), the planar FEM (triangular symbols) and 3D FEM (circular symbols) models developed in this work, and experimental results (star symbol), for various values of CTE of constituents' ratio α_2/α_1.

Equation 3.13 was designed for the range 2.3 $\leqslant \alpha_2/\alpha_1 \leqslant$ 3.6. However, Equation 2 performs well at the boundary $\alpha_2/\alpha_1 = 1$ for $\alpha_2 = \alpha_1 = 23.1$ (11% error) and $\alpha_2 = \alpha_1 = 8.6$ (22% error). As seen in Figure 3.19, Equation 3.13 agrees well with computational and experimental results in this work. Using Equation 3.13 we can thus engineer the CTE of my samples by varying three parameters: the CTEs of the constituents and the width of the frame. We can use the strong sensitivity of the frame's width to make coarse adjustments to the unit cell CTE, while making finer adjustments through the CTE of the plate and frame. This enables the design of metastructures with a precisely specified CTE.

Constituent 1 Constituent 2	Kovar Aluminum	Titanium Aluminum	Nickel Aluminum
CTE prediction (ppm/°C)	-3.63	1.12	8.35

Table 3.3 CTE of metastructures with different constituent materials

Table 3.3 shows the CTE of metastructures that can be achieved by using different metallic constituents and by tuning geometric parameters such as the frame width.

Metastructures with a wide range of CTE can be fabricated by using the approach described in this work. Even negative CTEs can be achieved if the ratio of CTEs of the constituents is high enough as in the in the case of the metastructure composed of Kovar (α=5.9 ppm/^{o}C) [76] and Aluminum.

3.5 Summary

In this chapter, we have demonstrated experimentally the ability to create thin bi-material metastructures exhibiting CTE of 2.6 ppm/^{o}C, significantly lower than that of their constituents (α_1= 8.6 and α_2= 23.1 ppm/^{o}C). Using planar and 3D finite element analysis, in agreement with experiments, we showed the ability to achieve fine and coarse control of the CTE from -3.6 to 8.4 ppm/^{o}C by varying three key parameters (α_1, α_2, and the frame beam width). We developed a robust fabrication procedure for high aspect ratio thin metallic structures allowing us to easily attempt new designs and ultimately develop large structures of arbitrary CTE. This allows us to design and fabricate thin, thermally stable, high aspect ratio metastructures with tunable CTE. In later chapters, we adapt this concept to test large areas lattices and to scale down this design to thin film scales.

Chapter 4

TAILORING THE THERMAL EXPANSION OF HIGH ASPECT RATIO METASTRUCTURE ARRAYS

In this chapter, we demonstrate metastructure arrays that exhibit a specified CTE which can be tailored by selecting constituent materials with difference thermal properties. The objective is to achieve arrays with large area coverage that can exhibit low and negative CTE.

The ability to vary the CTE of an array by appropriately choosing its constituent materials is demonstrated experimentally and computationally. The metastructure arrays fabricated and tested consisted of 16 unit cells with an aspect ratio of ~570. We studied the thermal response of the arrays as a whole as well as within the array. We observed excellent experimental agreement with FEM modeling and measured the CTE to be -3.72 and 1.17 ppm/°C for arrays made of Kovar/Al and Ti/Al, respectively.

4.1 Experimental

The experimental study of these arrays involved characterizing their thermal response and leveraging the impact of different constituent materials to tailor the thermal response. Two kinds of metastructure arrays were fabricated and tested in order to demonstrate near-zero and negative CTEs. Samples were fabricated using lithographic patterning and chemical etching. We characterized the thermal response of the samples using DIC and an IR camera.

4.1.1 Sample Design and Fabrication

Arrays consisting of 16 (4x4) unit cells were designed for fabrication and testing (Figure 4.1a). The number of unit cells was chosen such that there would be sufficient area to test away from the boundaries of the unit cell to avoid potential boundary effects.

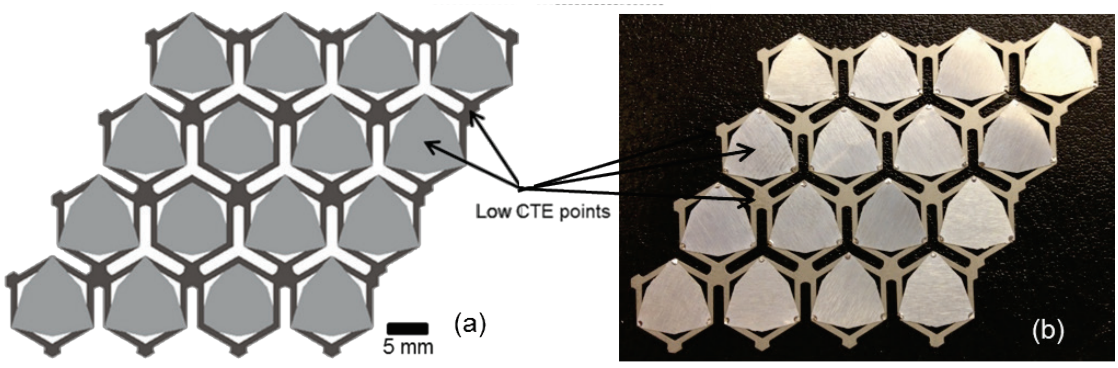

Figure 4.1 (a) Schematic diagram showing the geometrical characteristics of a lattice. (b) Image of a lattice fabricated out of Al and Ti constituents.

Previous work only studied lattices containing up to 10 unit cells and discussed the presence of boundary effects [23, 29]. Here, there exists four interior cells away from the boundary, allowing investigation of the lattice in all directions, in contrast to previous work [23].

Fabrication of the individual constituents was accomplished by photolithographic patterning and chemical etching of 125 μm thick sheet metal, as opposed to EDM which was used for the unit cells. Chemical etching proved more robust in maintaining part dimensions than EDM. Feature sizes in all chemically etched parts were within +/-25 μm, corresponding to ~3% variability for the frame beam width, the most dimensionally stringent feature. In many cases, the dimensional variability was related to undercutting, though this was not extensively studied.

Parts manufactured by EDM were also frequently damaged due to high temperatures on the part surface during machining. Chemical etching of the lattice constituents was performed in bulk by Photofabrication Engineering Inc [77]. This fabrication technique was essential in the successful development of arrays with engineered CTE. Analysis performed for single unit cells (Section 3.4) guided the material selection for the constituents of the arrays. Frame parts were made out of titanium and Kovar (a nickel-cobalt ferrous alloy related to Invar). All inner plates were made out of aluminum.

The constituent frames and plates were then joined by laser welding as in the unit cell. To prevent inconsistencies in the welds, tooling was designed to keep the parts in intimate contact during the process. Lack of intimate contact between the parts during welding was deemed to be the leading cause of weld inconsistency. Stress developed during laser-welding contributed to curvature in the initial configuration of the arrays, though the effect of the initial array shape was not extensively studied. Figure 4.1b shows an array successfully fabricated out of a titanium frame with aluminum inner plates. Successful arrays were also made with Kovar. The constraints in materials selection were weldability and lithographic patterning and etching.

4.1.2 Thermal Testing Methodology

The CTE of these arrays was computed by measuring displacements incurred as a result of temperature change. The experimental setup can be described by the schematic flow chart in Figure 4.2. Accurate measurement of displacements and temperature was critical.

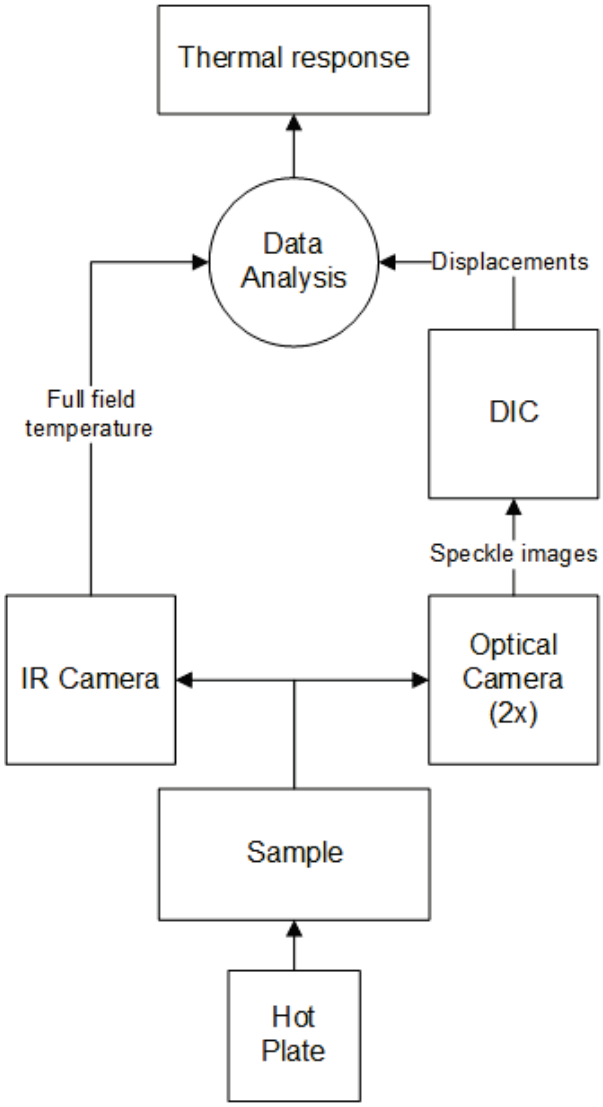

Figure 4.2 Flow chart of the setup used to measure the CTE of the array samples.

The size of the arrays necessitated accurate full-field temperature knowledge. This could be achieved in two ways: (i) by ensuring uniform temperature across the sample, and thus only requiring temperature data at only a few points; or (ii) by accurate knowledge of the temperature across the sample. We assessed both options. Maintaining uniform temperature across the sample would require a

thermal chamber. However, use of a thermal chamber would result in a large working distance in the optics used for digital image correlation and negatively impact resolution (see section 4.1.3). Instead, we chose to allow variability in the temperature across the sample, provided that it could be accurately determined.

Accurate, full-field knowledge of the temperature across the sample was obtained with an infrared (IR) camera. Displacements were computed with DIC. Then, the CTE of the sample was computed by analyzing the displacement and temperature data. An aluminum plate on top of the hot plate was used to improve the uniformity of heating. The hot plate temperature was incrementally increased in 20-40 °C steps and the sample was let to equilibrate at each temperature for about 20 minutes. Then, samples were imaged simultaneously with two optical cameras for DIC (Figure 4.3a) and an IR camera (Figure 4.3b). DIC was used to measure the thermal displacements and the IR camera was used to measure the sample temperature.

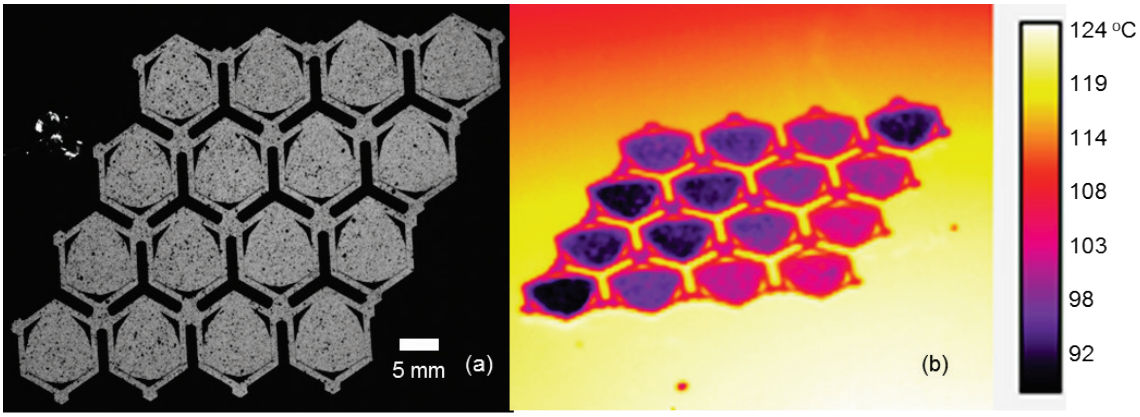

Figure 4.3 (a) Speckle image of array composed of Kovar and aluminum during testing; (b) IR camera image indicating temperature across the sample during testing.

An IR camera works by detecting electromagnetic radiation in the infrared spectrum (between 0.75 and 100 μm), which bodies at temperatures above 0 K emit. The intensity of this radiation is a function of physical constants, the absolute temperature of the body, and the wavelength of the radiation and is given by Planck's law [78]:

$$W_{\lambda b} = \frac{2hc^2}{\lambda^5\left(e^{hc/\lambda kT}-1\right)}. \tag{4.1}$$

In Equation 4.1, $W_{\lambda b}$ is the spectral radiant emittance at wavelength λ of a blackbody at temperature T, h is Planck's constant (6.626 x 10^{-34} J s), c is the speed of light (2.998 x 10^{8} m/s), and k is the Boltzmann constant (1.381 x 10^{-23} J/K). Equation 4.1 is plotted for various temperatures in Figure 4.4.

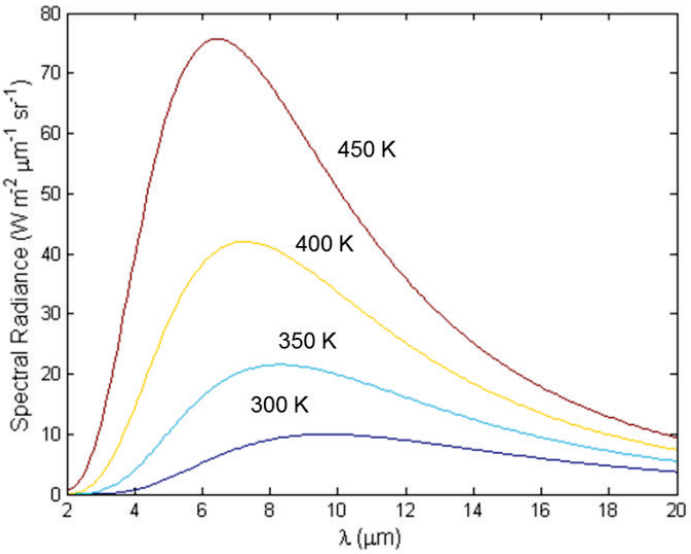

Figure 4.4 Planck's law (Equation 4.1) plotted for various temperatures; the spectral radiance is a measure of the intensity of radiation.

As shown in Figure 4.4, a blackbody will emit IR wavelengths with different intensity. An IR camera, which works over a narrow wavelength range, is calibrated to detect intensity and convert it to a temperature reading. A complication arises because most objects do not actually behave like blackbodies. In fact most materials will emit less radiation than a blackbody. The ratio of the actual intensity emitted to the intensity predicted by Planck's law under the blackbody assumption is called emissivity, ε. For an IR camera to accurately measure temperature the emissivity of the object should be high.

The IR camera used in this work, a FLIR SC6000, employs an indium antimonide (InSb) detector, sensitive at 3-5 μm [79]. The IR camera's reading was verified with thermocouples between room temperature and 250 °C and was found accurate to within 0.4 °C. To achieve such accuracy it is necessary that the emissivity of objects imaged is high enough ($\varepsilon > 0.9$) so that the radiation from the sample is detectable against noise. The objects being imaged during thermal testing were the aluminum plate on top of the hot plate and the arrays composed of aluminum, titanium, and Kovar. The emissivity of these materials generally ranges from 0.04 to 0.2 [80], which is too low for accurate temperature reading. This was resolved however, by spray painting the objects with Krylon Flat Black 1502 ($\varepsilon = 0.95$) [81].

4.1.3 Accuracy of the Testing Methodology

Error in the measurement of the thermal response can arise from error in measuring the displacements and/or error in measuring temperature. Error (%) in displacement measurement, u_{err}, in a particular direction would linearly affect error (%) in measured CTE, α_{err}, by the same amount: $\alpha_{err} = u_{err}$, for small displacements. Error in temperature measurement, ΔT_{err}, however, would affect percent error in measured CTE according to: $\alpha_{err} = \frac{1}{1+\Delta T_{err}} - 1$.

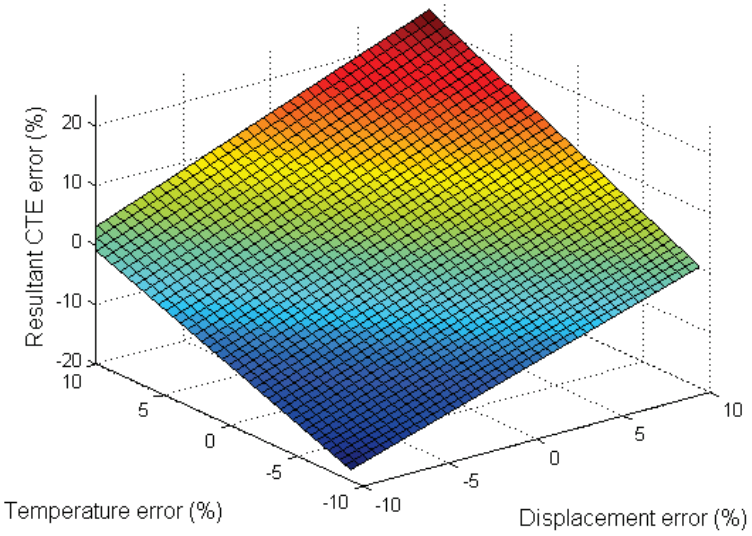

Figure 4.5 Combined effect on CTE error (%) due to measurement error in displacement and temperature.

Figure 4.5 shows the resultant error in CTE due to errors in temperature and displacement measurement, computed by multiplying the contributions of the individual errors. In the worst case scenario, 10% errors in displacements and temperature cause error in the CTE greater than 20%. However, actual displacement and temperature errors are considerably smaller. The thermal camera temperature accuracy was determined to be +/- 0.4 °C. A typical temperature step size used in determining the CTE was ~100 °C, which amounts to 0.4% error due to temperature. Error arising from displacements can be determined from the quality of the DIC correlation. Confidence intervals on the accuracy of the displacement are provided by VIC-3D. The displacement, mean, one standard deviation confidence margin is 730 nm. Error in displacement can be translated to error in CTE by computing the CTE resolution. CTE is computed across the length of a unit cell, 11.4 mm. Displacement error in a temperature step of 100 °C results in CTE error of 0.65 ppm/°C. Combining this with 0.4% error in temperature

measurement, we compute that the error in CTE over 100 °C is 0.66 ppm/°C. This error represents the effective resolution of the experimental setup used in this work.

4.1.4 Experimental Results

The CTE was computed by plotting strain vs. temperature for Kovar/Al and Ti/Al. arrays. Strain was computed by dividing the displacement of the segment of interest by its original length. To account for temperature differences between the two points of interest, displacements were scaled linearly by the temperature ratio of the points. Figure 4.6 shows the segments on an array over which the CTE was measured.

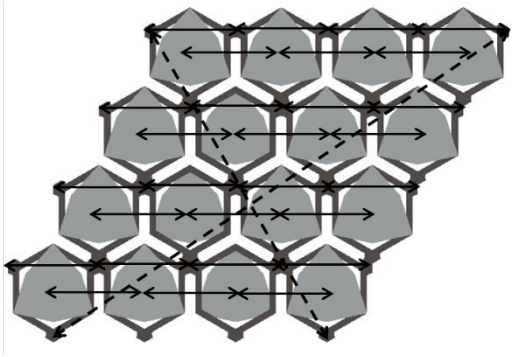

Figure 4.6 Array schematic showing segments used to measure the CTE of an array. Measurements were made across solid lines in order to determine the thermal behavior inside the array. Dotted lines indicate areas measured to determine the overall CTE.

Segments that were expected to exhibit low CTE based on the analysis in Chapter 3 were chosen for analysis. We took measurements at points both inside the array (shown as solid lines in Figure 4.6) and across the array (dotted lines in Figure 4.6). Even though the thermal behavior of the metastructure is defined by the expansion at its extremities, information inside the array is necessary to understand

the overall thermal response. In some cases, the region of engineered CTE was shifted slightly from the true centroids of the plate constituents. In these cases, we measured the CTE between the true centroids as well as the nearby regions which exhibited the desired behavior (see section 4.3 for more detail).

A linear fit (for details see section 3.4) of the strain vs. temperature was taken to compute the CTE. Scaling displacements by using temperature data generally resulted in significantly improved linear correlation between strain and temperature when compared with using an average homogeneous temperature. The correlation coefficient was improved from an average of 0.83 to 0.96 for a set of Kovar/Al array results. Correcting for the temperature distribution across the sample also resulted in an average 10% improvement in measured CTE. Figure 4.7 shows exemplary strain vs. temperature data for (a) Kovar/Al and (b) Ti/Al arrays. The negative slope (-4.5 ppm/^{o}C) of the linear fit in the Kovar/Al indicates contraction during heating. The CTE results are summarized in Table 4.1.

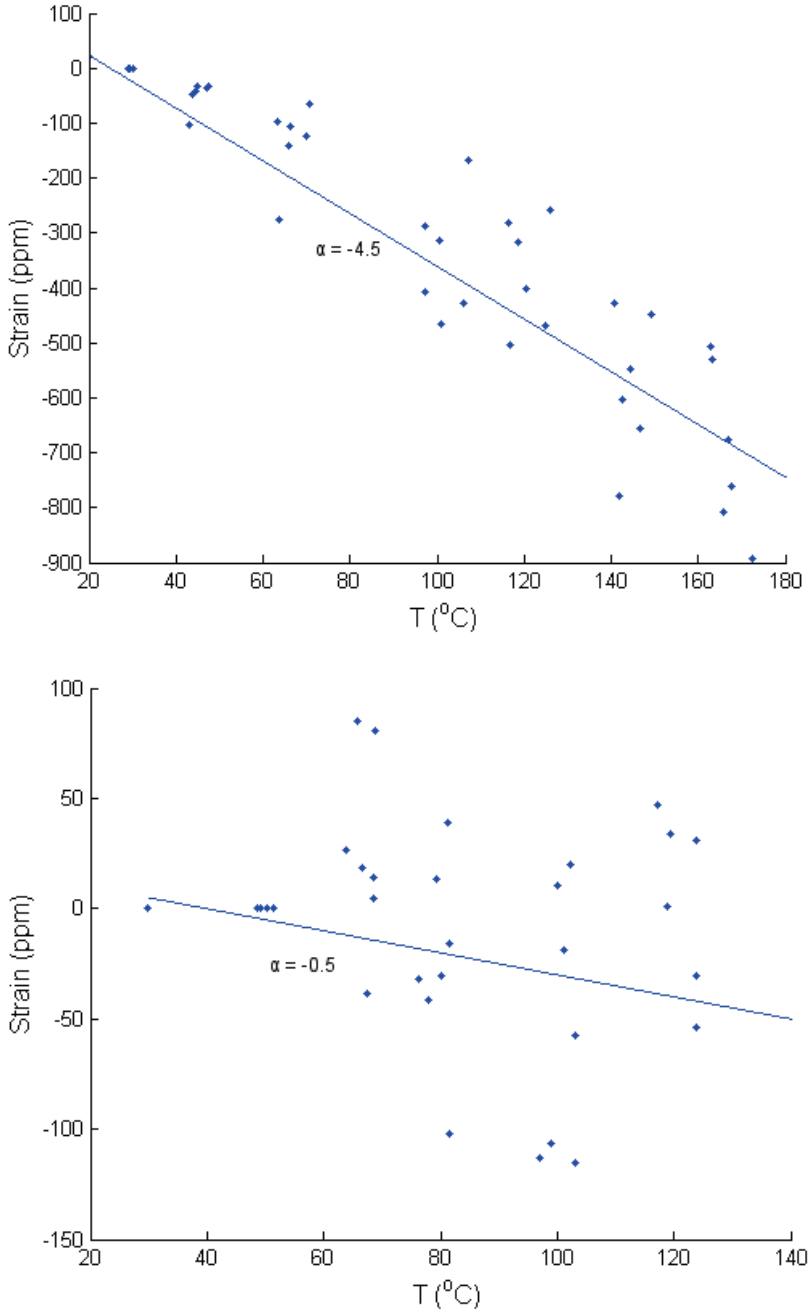

Figure 4.7 Strain (ppm) against temperature (°C) data for (a) Kovar/Al array and (b) Ti/Al array along points on a sample. The points represent experimental measurements and the lines indicate linear fits of the data. The slope of the lines corresponds to the CTE. Points on the frame nodes were used for the Kovar/Al array and points on the low CTE plate nodes were used for the Ti/Al array.

CTE (ppm/°C)	**Kovar/Al**	**Ti/Al**
Entire array (frame nodes)	-4.91 +/- 1.50	0.95 +/- 0.98
Entire array (plate centroids)	-2.52 +/- 0.52	3.78 +/- 0.83
Entire array (actual plate nodes)	-	-1.21 +/- 0.57
Entire array (average)	**-3.72 +/- 1.01**	**1.17 +/- 0.87**
Adjacent frame nodes	-4.50 +/- 1.79	1.72 +/- 2.35
Adjacent plate (centroids)	-2.69 +/- 1.64	3.11 +/- 2.19
Adjacent plate (actual nodes)	-	-0.50 +/- 2.02
Adjacent cell (average)	**-3.60 +/- 1.72**	**1.44 +/- 2.19**

Table 4.1. CTE of arrays as experimentally measured across the entire array, between adjacent nodes on the frame constituent, and between adjacent nodes on the plate constituent. Reported errors are either one measurement standard deviation or the measurement accuracy as determined in section 4.1.3, whichever is higher.

4.2 Computational

An FEM model was developed to simulate the experiments performed on the arrays and gain further understanding of their thermal response. The objective was to simulate the experiment performed on the arrays as accurately as possible and use the FEM model to explain observed phenomena.

4.2.1 FEM Model of Arrays

The FEM problem formulation was similar to the one described in section 3.2.1. However, nonlinear FEM was necessary as global out-of-place displacements exceeded 25% of the array thickness. Nonlinear FEM solves the problem iteratively, beginning with a deformed configuration obtained from the previous step. The experiment was simulated by changing the temperature of the array in 20 °C increments from 20 to 220 °C. Half the array was simulated by taking advantage of symmetry and a fully converged mesh was used. The model contained 185,204

C3D10 elements with 382,392 nodes. The material properties used in the model are shown in Table 4.2.

	Al	Ti	Kovar
Elastic Modulus (GPa)	70	116	159
Poisson's Ratio	0.35	0.32	0.32
CTE (ppm/oC)	23.1	8.6	5.0

Table 4.2 Properties of materials used in array FEM model

4.2.2 FEM Results

The FEM model showed agreement with experimental results. The thermal deformation mechanics of the arrays can be visualized by plotting the 2D displacements (Figure 4.8).

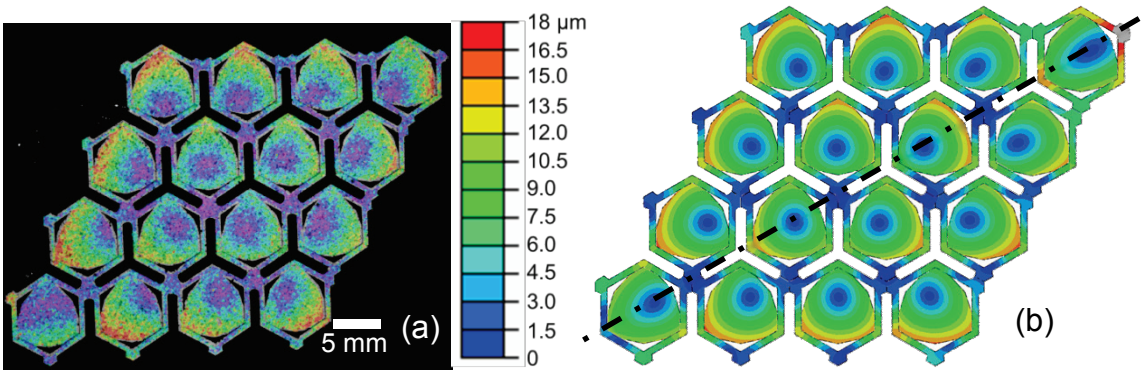

Figure 4.8 In-plane displacement magnitude for Ti/Al metastructure under a thermal load of 125°C (a) as measured experimentally by DIC; and (b) as computed by FEM. The dashed line indicates the axis of symmetry that was used in the FEM model to increase computational efficiency. Blue areas indicate regions of zero displacement and low overall thermal expansion between those regions. Experimental (a) and computational (b) results agree very well both in the magnitude and spatial variation of the displacements across the sample.

Figure 4.8 shows good agreement in thermal deformation between the (a) experimentally tested and (b) simulated Ti/Al array. As seen by the blue regions in Figure 4.8b, each unit cell exhibits a region of zero displacement and thus, zero CTE. The maximum displacement (shown in red) occurs at regions symmetrically opposite to the regions of minimal displacement. As experimentally observed (Figure 4.8a), the FEM simulation predicts an eccentricity to the location of the zero displacement regions (Figure 4.8b). In an ideal zero CTE array, the zero CTE region would occur at precisely the center of each unit cell. However, in realistic, nonzero-CTE arrays, there exists a region of zero displacement within each unit cell, though it is not located at the center. This region distinguishes positive CTE and negative CTE areas. Figure 4.9 shows how the CTE of an array varies based on distance from the center of the unit cell. The Kovar/Al array, which on average exhibits negative CTE, contains regions of positive CTE and similarly the Ti/Al array contains regions of negative CTE. The thermal deformation mechanics between the two arrays are similar except for a shift in the CTE.

The thermal strain between different points on the array was computed in order to further study the thermal response. As in the experiments, points in frame nodes and plate centroids were chosen. Figure 4.10 shows the strain against change in temperature for the Kovar/Al (a) and Ti/Al (b) arrays. For the adjacent frame nodes, two nodes on the frame in the middle unit cells of the array were chosen. In computing the entire array CTE the two unit cells at the top edge of the array were chosen. The nonlinear out-of-plane deformation introduces dependence in the CTE as a function of temperature. Thus the thermal strain curves are nonlinear. In Figure 4.10, the thermal strain curves are all concave down; increasing out-of-plane displacements results in lower CTE. This phenomenon is consistent with what is discussed in Chapter 3. The nonlinearity is more significant in the arrays than in the unit cells due to the higher aspect ratio of the arrays (discussed in Chapter 3).

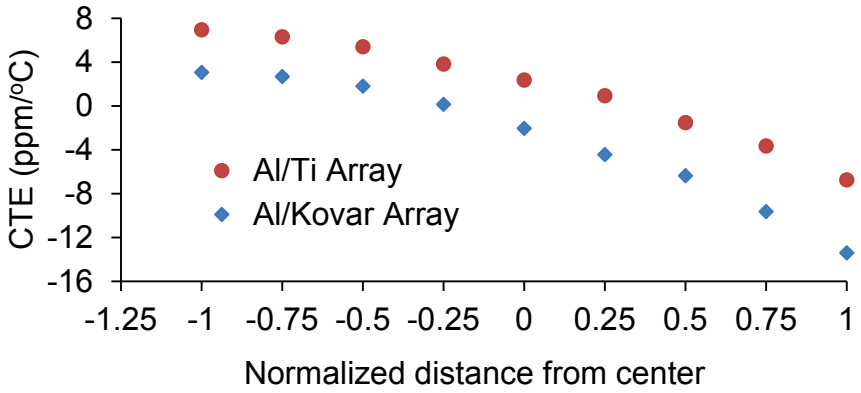

Figure 4.9 CTE between two unit cells in Ti/Al and Kovar/Al arrays as a function of radial distance from the center of the unit cell, as computed by FEM. The CTE is computed by measuring the strain between a point on one unit cell and the reflectively symmetric point on a unit cell two cells away and dividing by the temperature difference (80 °C).

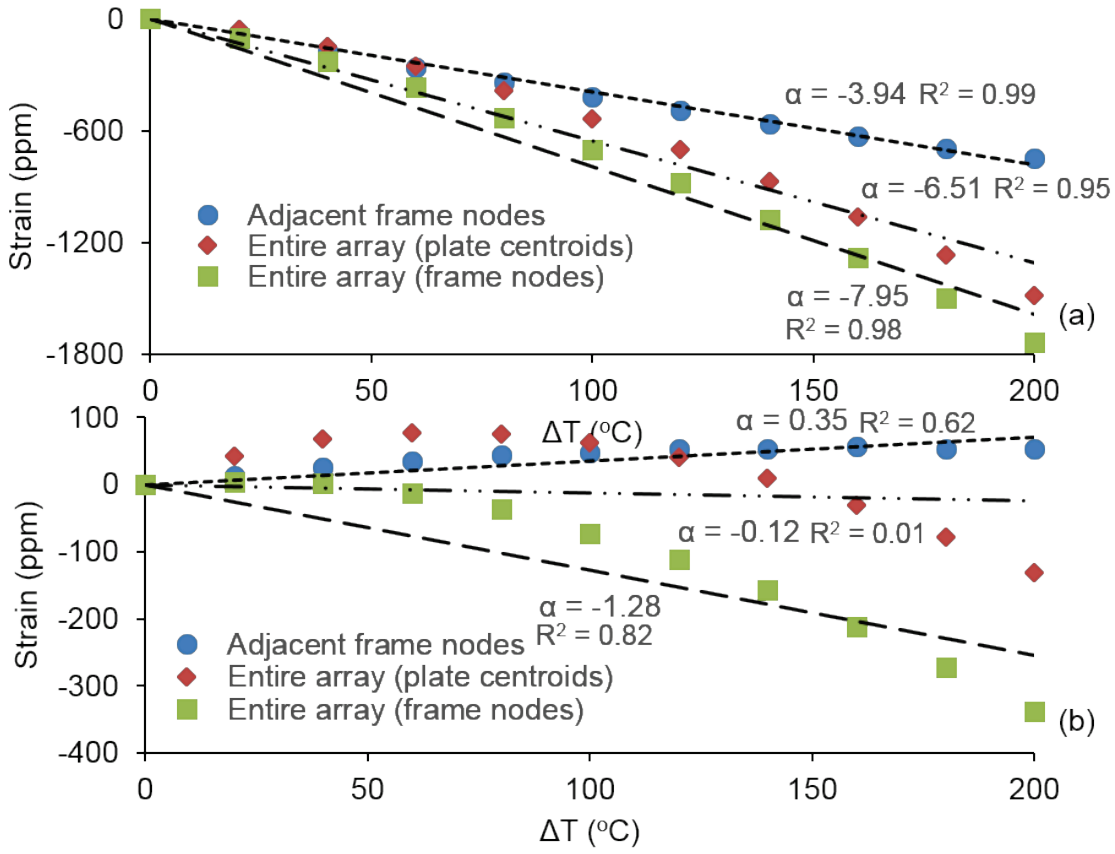

Figure 4.10 Strain against change in temperature for the Kovar/Al (a) and Ti/Al (b) arrays, as predicted by FEM. Dotted lines indicate linear fits to the data. The CTE, α, is computed by the slope of the linear fit.

Out-of-plane deformation also results in CTE dependency on the distance between the measured points. Since unconstrained thermal loading causes the arrays to undergo flexure (with theoretically constant curvature), the points at the extremities of the array will experience the highest out-of-plane displacement. Thus the CTE will be minimum between those points. This is evident in Figure 4.10; the CTE is lowest between the frame nodes of the entire array. The concavity of thermal strain results in increasing spatial dependence of the CTE as the temperature differences increase. The average CTE over the whole 200 °C

temperature difference range, α, is computed by taking the slope of the linear fit of the strain-temperature data (Figure 4.10). Even though the curves are nonlinear, the linear fit is computed to maintain consistency with the definition of CTE. The CTE of the Kovar/Al array is negative and that of the Ti/Al array is near zero, as designed. To compare directly with experimental results the CTE is calculated at the same points as in experiments by computing a linear fit up to 140 °C (for plots see Appendix A.3). The results of the CTEs as computed by FEM are shown in Table 4.3. Since the CTE within the array is not constant, multiple points are chosen for the calculation, similarly with experimental procedure.

CTE (ppm/oC)	**Kovar/Al**	**Ti/Al**
Entire array (frame nodes)	-8.25 +/-1.90	-0.44 +/- 1.18
Entire array (plate centroids)	-3.34 +/-1.20	1.62 +/- 0.70
Entire array (average)	**-5.80 +/- 1.55**	**0.61 +/-0.94**
Adjacent frame nodes	-4.42 +/- 0.53	0.72 +/- 0.23
Adjacent plate (centroids)	-2.44 +/- 0.67	2.20 +/- 0.73
Adjacent cell (average)	**-3.43 +/- 0.60**	**1.46 +/- 0.48**

Table 4.3 CTE of arrays as computed by FEM between the entire array, between adjacent nodes on the frame constituent, and between adjacent nodes on the plate constituent. Since the CTE is not constant within the array, one standard deviation of the CTE between the points used to determine the CTE is also shown.

Figure 4.11 compares the experimental and FEM CTE results. Good agreement is observed in between the FEM and experiments. In all cases, computational and experimental results are within error. The predictive model developed in Chapter 3 (Equation 3.13) shows excellent agreement with experimental results.

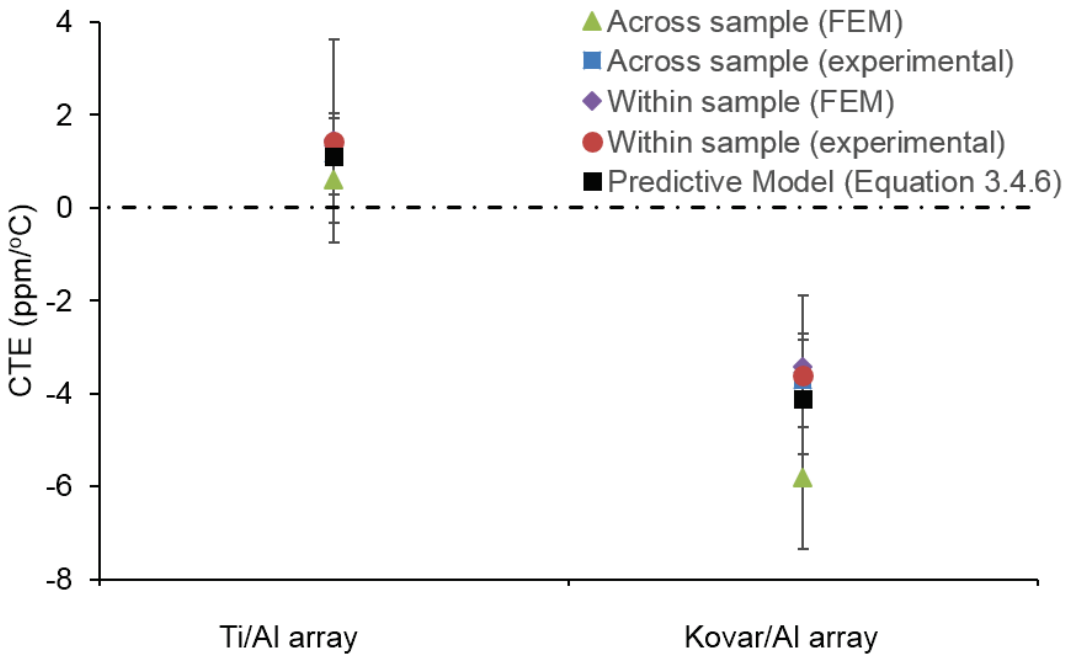

Figure 4.11 CTE of the Ti/Al and Kovar/Al arrays measured within and across the sample experimentally and computationally with FEM. The prediction of the model developed in Chapter 3, is also shown. The arrays perform as designed, with the Ti/Al array exhibiting near-zero CTE and the Kovar/Al array exhibiting negative CTE.

The FEM tends to predict lower CTE than experimentally observed when measuring across the sample. This can be attributed to the nonlinear of out-of-plane thermal deformation at the edges. Experimentally, out-of-plane deformation causes the sample to not be in contact with the hot plate, thus decreasing the sample temperature and ultimately out-of-plane deformation at the edges. In the FEM simulations, however, a uniform temperature distribution is applied on the model, regardless of out-of-plane deformation. As the deformation becomes nonlinear, the methodology used to account for a temperature distribution across the sample becomes less accurate, because it assumes linear displacements.

The stresses induced by thermal loading were determined to be within the Von Mises yield criterion for temperatures up to at least 150 °C (Appendix A. 3.5). Stress concentrations occur near the weld areas, while the inner plate region exhibits significantly lower stress.

4.3 Discussion

4.3.1 Comparison with Previous Work

The unique thermal properties of the arrays developed here can be seen in Figure 4.12 which compares the CTE of the metastructures with that of their constituents. Arrays developed and studied in this work exhibit CTE outside the bounds of their constituents. We demonstrate, for the first time, the experimental realization of a Kovar/Al metastructure array, which exhibits negative CTE (~ -3.6 ppm/°C), even though composed of positive-CTE constituents. The Ti/Al array exhibits near-zero CTE (~ 1.4 ppm/°C), similar to the one in [23].

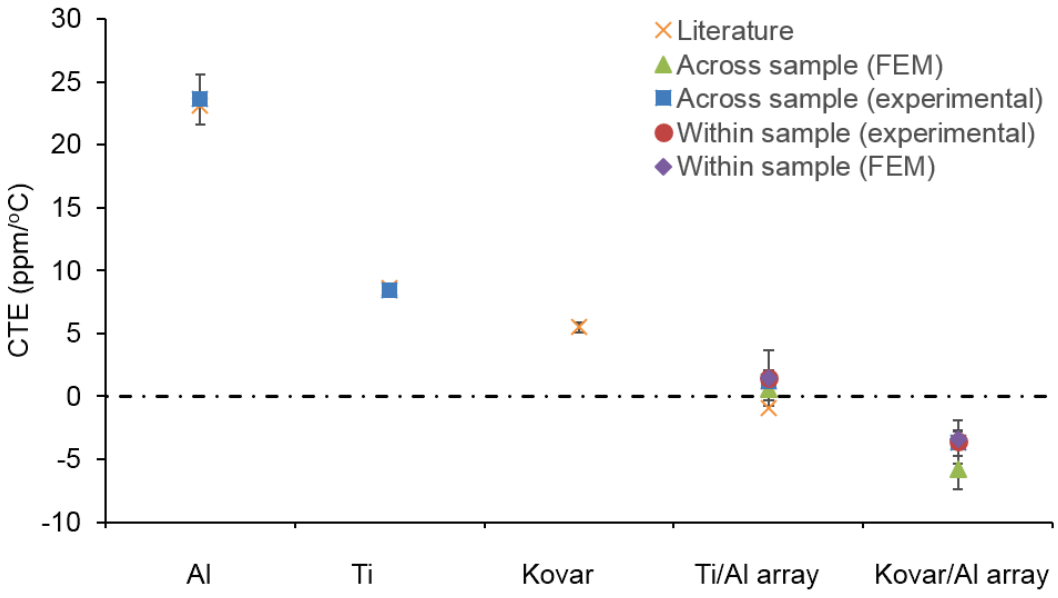

Figure 4.12 The CTE of metastructure arrays developed in this work compared with the CTE of their constituent materials and arrays developed in literature. The Ti/Al array developed here exhibits similar CTE to the one demonstrated in [23] with six times higher aspect ratio. The measured CTEs of Al and Ti agree well with literature [68]. The CTE of Kovar was reported in [76]. This work presents the first time a Kovar/Al array has been experimentally realized and shown to exhibit negative CTE.

The arrays that we studied are the first experimental instantiations of thin foil scale (125 μm thick constituents) arrays with 16 unit cells. Thinner and laterally larger structures solely of Ti and Al constituents have been incrementally developed in previous work; however, the most recent development prior to this work studied 3 mm thick of nine unit cells [22, 23, 29]. Improved fabrication techniques have been essential to extending previous work to higher aspect ratios. Previous work used laser-cutting and press-fitting techniques described by Wadley et al [82]. However, these methods were replaced in this work by photolithographic patterning and laser-welding, which are more effective in smaller scales. Also essential to the implementation of higher aspect ratio metastructures has been the study of out-of-

plane effects. As the bending stiffness decreases due to lower thickness, the out-of-plane deformation increases and the effect on thermal response becomes more significant.

4.3.2 Future Work

The design, fabrication, and testing approach used in this chapter can be easily adapted to develop and characterize metastructures of even smaller size scales with a wide range of CTE. Photolithographic fabrication can be easily used in smaller scales, while the resolution of DIC can be improved by decreasing the speckle pattern size and by using higher magnification optics. Of course, there are also limitations to this approach. The out-of-plane deformation induced by the metastructure design could produce undesired effects in applications where low out-of-plane CTE is critical. Additionally, the variability of the CTE within an array leads to potentially undesirable inhomogeneity. Finally, the laser-welding technique can limit further decreasing of the size scale of the metastructure.

In future work, it will be important to assess the possibility of limiting out-of-plane deformation. One way that this could be accomplished would be by balancing the metastructure with symmetrical layers, similarly to composite laminates. It is also important to further study and identify all causes of inhomogeneity of thermal deformation within an array. This can be partly accomplished by removing potential sources of fabrication variability, primarily arising during the alignment phase. Tooling similar that is used in microfabrication could be developed to ensure precise alignment. Metastructures developed in this work could be applied in the future as thermally stable substrates, attached potentially by laser-welding.

4.4 Summary

We designed, fabricated, and thermally characterized low and negative CTE, thin (125 μm), high aspect ratio (~570) Ti/Al and Kovar/Al metastructure arrays in good agreement with FEM results. Principles developed in Chapter 3 enabled me to design metastructure arrays by predicting the CTE of metastructures with different constituents and appropriately considering out-of-plane deformations and structural design effects. To fabricate these metastructure arrays, we used photolithographic patterning and laser-welding. These techniques enabled precise and repeatable feature control in the desired size scale. We used DIC and an IR camera to obtain full-field measurement of displacements and temperature of the sample during testing. The IR camera allowed me to accurately correct for temperature differences across the sample during testing, while achieving submicron resolution with DIC. The full-field temperature and displacement information enabled direct comparison with FEM and led to understanding of the thermal deformation within an array.

Chapter 5

CHARACTERIZATION OF THIN FILM METASTRUCTURE ARRAY CONSTITUENTS

Since the overall thermal and mechanical properties of the bimetallic lattice depend on the properties of its constituents, we characterized as-deposited Al and Ti by SEM inspection, nanoindentation, XRD, and by measuring the wafer curvature and applying Stoney's equation [83]. The films were found to exhibit nanograined microstructure with [1 1 1] preferential orientation (i.e., texturing). The elastic moduli of the Al and Ti thin films were found to be 78.5 and 135.3 GPa, slightly higher than the bulk values of 70 and 116 GPa. This discrepancy was attributed to the film texturing. Wafer curvature measurement showed that the as-deposited Al film exhibited compressive residual stress (~50 MPa) while the Ti film exhibited tensile residual stress (~200 MPa). The Al film compressive stress, which could cause buckling during wafer lift-off, was mitigated by annealing.

5.1 Deposition of Al and Ti Films

First, Al and Ti films were deposited on Silicon wafers using electron-beam (E-beam) evaporation. Electron-beam evaporation is a process wherein a target material is heated by an E-beam in high or ultra-high vacuum ($< 7\text{x}10^{-6}$ Torr). The E-beam vaporizes the target material which is then deposited on the substrate. Uniform deposition is highly dependent on the quality of the vacuum, which influences the mean free path of the vapor particles. The vapor particle mean free path, l, is given by:

$$l = \frac{k_B T}{\sqrt{2}\pi d^2 p}, \tag{5.1}$$

where k_B is the Boltzmann constant, T is the temperature, d is the diameter of the gas particle diameter, and p is the pressure. In a typical evaporation process at $5x10^{-7}$ Torr and 30 – 100 °C, the mean free path of the vapor particles is of the order of kilometers. In our process the evaporation rate was set to 2.0 A/s. This relatively high evaporation rate was necessary to deposit 1 μm thick films within tool usage time constraints. The high evaporation rate caused inconsistencies during the deposition of Ti, which requires a more powerful E-beam than Al, due to its higher melting point. The target thickness was 1 μm, though the actual thickness of the deposited films ranged from 0.9 μm – 1.2 μm. The thickness was measured by profilometer and cross-sectional SEM observation. We attribute deviation from the target thickness to error accumulation in the rate measurement during the deposition process due to the relatively thick films that we deposited.

5.2 Grain Size of Deposited Al and Ti Films through SEM Observation

Following film deposition, we inspected the films' grain structure with SEM (Figure 5.1). We observed nanograined structure in both metals. By using the intercept procedure [84] we measured the average grain size to be 80 nm for Al and 92 nm for Ti. Grain size can impact material properties such as yield strength. Grain size is known to inversely influence yield stress through the Hall-Petch [85, 86] relationship:

$$\sigma_y = \sigma_o + \frac{k_y}{\sqrt{d}}, \tag{5.2}$$

where σ_y is the material yield stress, σ_o and k_y are material constants and d is the average grain diameter. Equation 5.2 is accurate for grain sizes larger than 1 μm

and roughly accurate for grain sizes between 30 nm and 1 μm; for grains smaller than 30 nm an inverse Hall-Petch behavior is observed [87]. The yield strength of nanograined Al and Ti films has been shown to range from 300 to 600 MPa and 650 to 800 MPa, respectively [88-90]. Inverse dependence of grain size has also been observed for the CTE of nickel and copper thin films [91]. However, little work exists in literature on the dependence of CTE and Young's modulus on grain size for Al and Ti films. It has been shown that the CTE of nanograined Al films can range from 32 ppm/°C to 23 ppm/°C as a function of thin film thickness [92-94]. The Young's modulus of nanograined Al and Ti thin films has been shown to range from 60 to 90 GPa and 90 to 110 GPa, respectively [90, 95, 96].

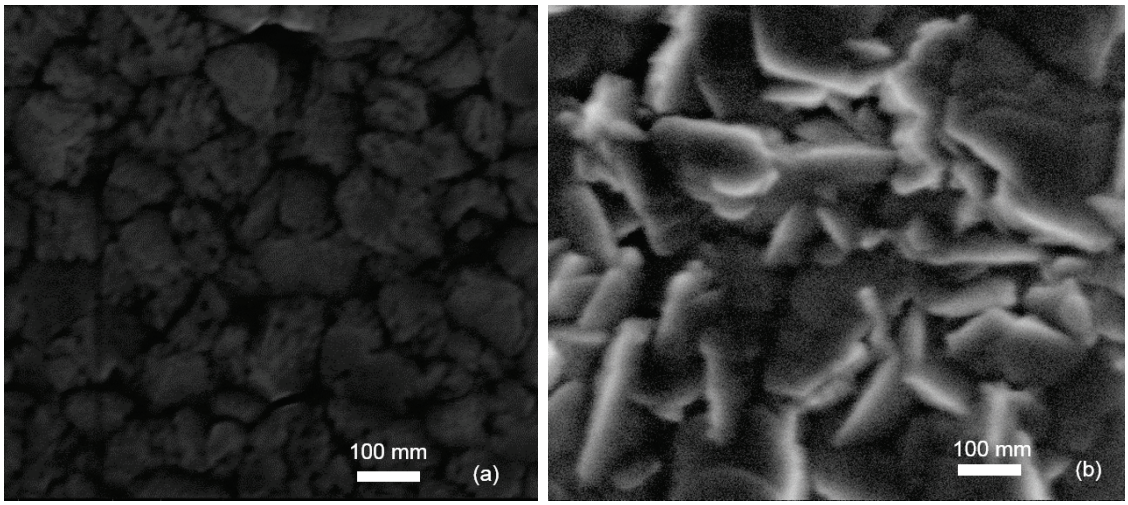

Figure 5.1 SEM image of grains in (a) Al and (b) Ti as-deposited thin films. Magnification is 300,000 for both images. Al (a) was imaged with a 19.5 kV E-beam, while Ti (b) was imaged with a 2 kV E-beam.

5.3 Elastic Modulus of Al and Ti Films through Nanoindentation

To characterize the mechanical properties of the as-deposited Al and Ti thin films we performed nanoindentation experiments.

5.3.1 Fundamentals of Nanoindentation

Nanoindentation is an experimental technique in which an indenter tip penetrates a material while the applied load and displacement are being recorded; mechanical properties can then be extracted from the load-displacement data. The type of indenter tip has been shown to significantly influence the accuracy of the measurement of mechanical properties, with the Berkovich tip, a three-sided pyramidal shape, yielding good results [97]. The Young's modulus of a material is related to the slope of the initial portion of the unloading portion of the load-displacement curve:

$$\frac{\mathrm{dP}}{\mathrm{dh}} = \frac{2}{\sqrt{\pi}} \mathrm{E_r} \sqrt{\mathrm{A}}. \tag{5.3}$$

In Equation 5.3, $\frac{dP}{dh}$ denotes the slope of the unloading curve (P is the load, h the penetration depth), A is the projected contact area, and E_r is the sample's reduced elastic modulus. The contact area, A, can be shown to follow the following relation:

$$\mathrm{A} = \mathrm{f}(\mathrm{h_{max}} - \mathrm{h_s}), \tag{5.4}$$

where $\mathrm{h_{max}}$ is the maximum penetration depth, f is a function determined empirically through experimental calibration, and h_s is given by:

$$\mathrm{h_s} = \epsilon \frac{\mathrm{P_{max}}}{\mathrm{dP}/\mathrm{dh}}, \tag{5.5}$$

where ϵ is a geometric constant dependent on the indenter tip shape. It is shown that $\epsilon = 0.75$ is a good approximation for a Berkovich tip [98].

The reduced elastic modulus, E_r, is related to the sample elastic modulus, E, by:

$$\frac{1}{E_r} = \frac{1-\nu^2}{E} + \frac{1-\nu_i^2}{E_i}, \tag{5.6}$$

where E_i and ν_i are the elastic modulus and Poisson's ratio of the indenter tip, respectively. Thus, the sample's elastic modulus can be computed with knowledge of the load-displacement curve and a calibrated nanoindentation system by using Equations 5.3 – 5.6.

5.3.2 Measurement of Thin Film Elastic Modulus

We used an MTS Nanoindenter G200 system to conduct the indentation experiments on as-deposited Al and Ti thin films, 1 μm thick. A diamond Berkovich indenter tip was used. It was assumed to behave elastically, with $E_i = 1140$ GPa and $\nu = 0.07$. The maximum penetration depth for each sample was 100 nm, i.e., 10% of the film thickness. It has been shown that the maximum indentation depth should be less than 10% of the film thickness to avoid substrate effects in measurement [99]. Between 10 and 20 spots, 1 mm apart, are indented in each sample. The penetration happens at a strain rate of 0.025 s^{-1}. The nanoindenter system automatically adjusts to account for indenter movement due to thermal drift. Load-displacement curves for exemplary nanoindentation experiments on Al and Ti films are shown in Figures 5.2a and 5.2b, respectively.

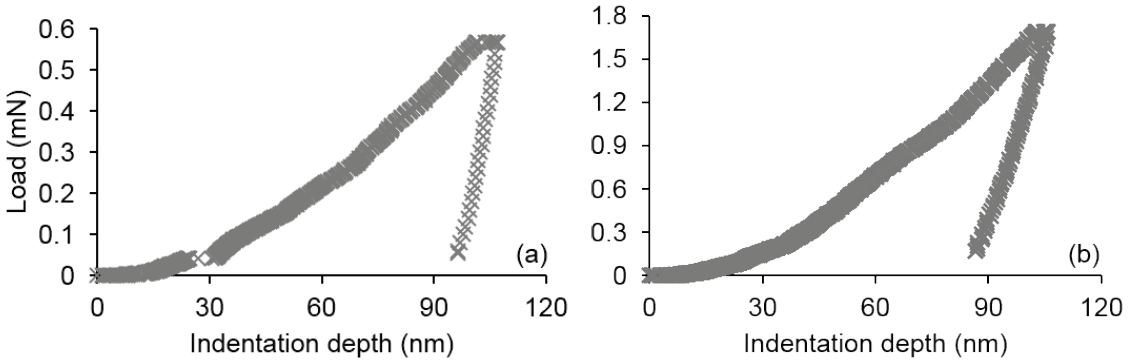

Figure 5.2. Load vs. displacement as measured in a nanoindentation experiment for (a) Al and (b) Ti thin films.

Table 5.1 summarizes the findings of the nanoindentation measurements. We performed a total of 55 indentations on three Al films and 30 indentations on three Ti films. The elastic modulus for the Al films is measured within the range of what is reported in literature and within 13% of the commonly used value of 70 GPa [68]. The elastic modulus of Ti exhibits higher variability than Al, as measured by the standard deviation. This is attributed to inconsistencies experienced during deposition of the Ti films, as mentioned above. Deposition parameters have been shown to influence mechanical properties [96]. Furthermore, we measured a relatively high elastic modulus for the Ti films as compared to the range reported in literature, though still within 17% of commonly used 116 GPa [68]. The consistently relatively high measurement of the elastic modulus in the Al and Ti films, over a statistically significant sample, leads us to believe that the error is of systematic nature. To test the system calibration we performed nanoindentation with the same settings on a 2 mm thick piece of Al 6061 sheet and measured the elastic modulus to be 71.6 GPa (2.4% error from 70 GPa). This result significantly decreases the probability that the systematic error is due to poor calibration of the nanoindentation system. Instead, it points to either the presence of a substrate

effect, which has been shown to be present at even 10% penetration depth [95, 99], or truly altered mechanical properties. A possible explanation could be preferential orientation of the films in a direction of higher stiffness. Regardless of whether the observed increase in elastic modulus is an artifact or a physical result, elastic modulus has been shown in Chapter 3 to not significantly influence the CTE of bi-material metastructures.

Elastic modulus (GPa)	**Measured**	**Literature**
Titanium (1 μm thick)	135.3 +/- 23.3	90 - 116 [68, 90, 96]
Aluminum (1 μm thick)	78.5 +/- 9.4	60 – 90 [68, 95, 96]
Al 6061 (2 mm thick)	71.6 +/- 19.3	70 [68]

Table 5.1 Mean elastic modulus of as-deposited thin films measured by nanoindentation. 55 indentations were performed on three Al films and 30 indentations on three Ti films. Variability indicates one standard deviation.

5.4 Lattice Structure of Al and Ti Films through X-ray Diffraction

To further characterize the microstructure of the Al and Ti films we conducted XRD measurements.

5.4.1 Fundamentals of XRD

XRD is a technique for extracting information about the atomic structure of a material by shining an X-ray beam (of wavelength λ) at a series of angles, ϑ, and recording the intensity of the beam scattered by the material's atomic structure. Depending on the material's interatomic spacing, d, intensity peaks will be observed for specific angles. Interatomic spacing can thus be computed from Bragg's law [100]:

$$2d\sin(\theta) = n\lambda. \tag{5.7}$$

From Bragg's law we would expect that there would be discreet angles of high intensity. However, in a typical XRD experiment, a finite width peak is observed in the diffraction curve. There are two factors that contribute to the peak widening: (i) imperfections (slight misalignments, calibration, etc...) in the XRD instrument and testing conditions and (ii) physics from the sample itself. By accurately deconvoluting the effect of instrument and test conditions from sample-intrinsic reasons for peak broadening, we can use peak broadening to gain information about the sample. The instrument and testing conditions effect can be determined by measuring the peak width of a very large grain size standard sample. The sample causes peak broadening for three reasons: (i) finite crystallite size; (ii) presence of microstrain; and (iii) temperature effects. The finite crystallite size contributes to peak broadening because incident X-rays at angles close to the theoretically infinitely narrow peaks produce incomplete destructive interference due to differences in in spacing between atomic planes [100]. The width of the diffraction curve, B, is related to the crystallite thickness, t, by Scherrer's formula:

$$t = \frac{K\lambda}{B\cos(\theta)}, \tag{5.8}$$

where K is a factor related to the shape of the crystallite, commonly taking the value 0.9 [100]. Equation 5.7 is accurate for crystal sizes up to 1000 nm; when the crystal is larger than 1000 nm, the peak broadening due to crystallite size is so slight that it cannot be deconvoluted from the other sources.

Uniform crystal lattice strain does not cause peak broadening but rather peak shift, according to 5.7. However, non-uniform strain results in multiple shifts of the peak which in turn appears as peak broadening. The strain can be calculated from by differentiating 5.7 with respect to d:

$$b = -2\frac{\Delta d}{d}\tan(\theta), \tag{5.9}$$

where b is the broadening due to fractional variation in the Bragg plane spacing. This value of strain corresponds to the sum of the maximum principal strains and is usually divided by two to obtain the maximum tensile/compressive strain, assuming that the two are equal in magnitude [100].

Atomic oscillations around their mean position in a crystal are a function of temperature and the elastic constants of the crystal. Theoretically, such thermal vibration causes an increase in peak width. However, temperature factors have been experimentally shown to not be a big contributor to peak broadening until temperatures near the melting point and can usually be safely ignored [100].

5.4.2 XRD Measurements

We performed XRD measurements on Al and Ti films in order to compute the crystallite size and effective internal strain. We also performed XRD measurements on a polycrystalline Si powder standard sample to deconvolute the effect of instrument and testing parameters. A PANalatyical X'Pert Pro X-ray powder diffractometer was used to perform the measurements. The diffractometer uses a Copper anode which emits X-rays at a wavelength of 0.15406 nm. The anode voltage was set to 45 kV. The full spectrum of angles (30^o – 90^o) was measured with quick scans (less than 30 minutes) and the peaks at ~38^o were observed to be the strongest. Consequently they were imaged by scanning between 35^o and 41^o. The angular step size was 0.001^o and each step was held for 2 seconds. The total XRD measurement time was 3.5 hours and it was performed at ambient temperature. Figure 5.3 shows the XRD peaks of the imaged (a) Al and (b) Ti thin film samples.

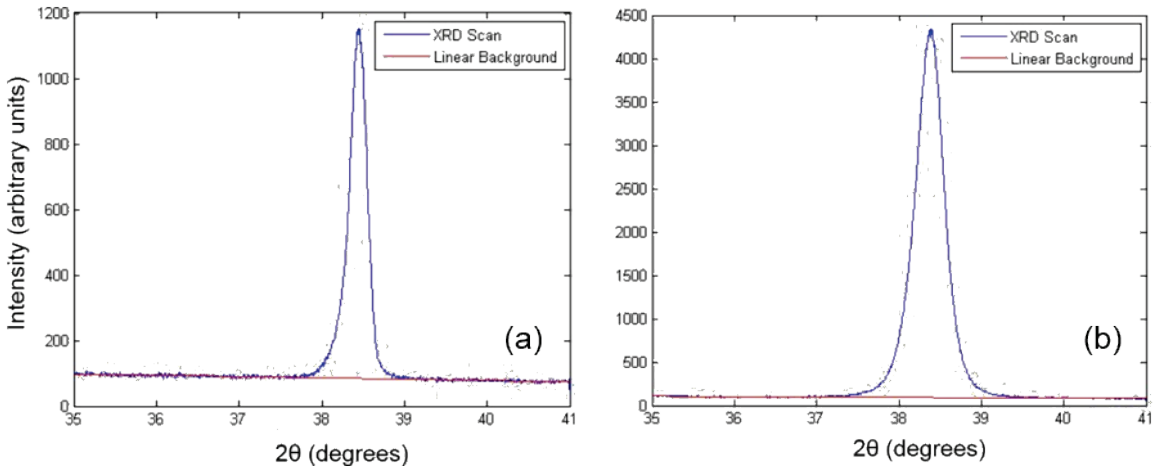

Figure 5.3 Intensity vs. 2ϑ in a typical XRD measurement for (a) Al and (b) Ti thin films. A broader peak is observed on the Ti sample.

The relative intensity of the ~38° peaks compared to the other peaks indicated that the films had a [1 1 1] texturing. X'Pert HighScore software was used to deconvolute the effects of internal lattice strain, crystallite size, and instrument and testing setup on peak broadening. Table 5.2 summarizes the computed strain, stress, and crystallite size for our samples.

	Crystal size (nm)	**Orientation**	**Strain (%)**	**Stress (MPa)**
Titanium	22	[1 1 1]	+/- 0.496	+/- 575.4
Aluminum	39	[1 1 1]	+/- 0.294	+/- 205.8

Table 5.2 Lattice properties of Ti and Al thin films determined by XRD measurements. XRD predicts the sum of absolute values of the maximum and minimum principal strains.

The texturing observed in the Aluminum and Titanium could explain the increased elastic modulus measured by indentation. If we consider purely [1 1 1] oriented Al and Ti films in uniaxial tension, their elastic moduli would be 106.75 GPa and

162.4 GPa respectively [68]. The nanoindentation measurements of 78.5 and 135.3 GPa for the elastic moduli of A and Ti fall between the bulk values (70 and 116 GPa) and those for purely [1 1 1] oriented crystals (106.75 and 162.4 GPa), indicating that texturing could be the cause of the observed increased elastic moduli.

The crystal sizes of 22 and 39 nm for Ti and Al is consistent with the SEM observed grain sizes of 92 and 80 nm, corresponding to 2-4 crystallites per grain. The measured internal stress in the Al and Ti films could create challenges during fabrication of the lattice, particularly with out-of-plane buckling. Since XRD cannot determine the exact value of strains/stresses, but rather the sum of absolute values of principal strains, it is important to measure internal strains/stresses directly.

5.5 Internal Stress of Al and Ti Films through Wafer Curvature and Effect of Annealing

A direct way to measure internal stresses in a thin film of thickness h_f on a substrate of thickness h_s is by measuring the resulting curvature, $\varkappa$, and relating it to stress through Stoney's formula [83]:

$$\sigma_f = \frac{E_s h_s^2 \kappa}{6h_f(1-\nu_s)}. \tag{5.10}$$

In Equation 5.10, subscripts f and s denote the film and substrate, while E and ν are the elastic modulus and Poisson's ratio respectively. Equation 5.10 assumes film and substrate thickness uniformity, infinitesimal strains, linear elasticity, isotropic film stresses and no out-of-plane stresses, equibiaxial curvature, and spatially constant stresses across the system [101]. To satisfy the last assumption it is important to measure the global curvature of the system. We used a Tencor

FLX-2320 Thin Film Stress Measurement system, which uses laser interferometry to measure the wafer curvature. The wafer curvature is measured before and after deposition and the stress is calculated with Equation 5.10. To assess the effect of thickness on residual stress we measured films of various thicknesses.

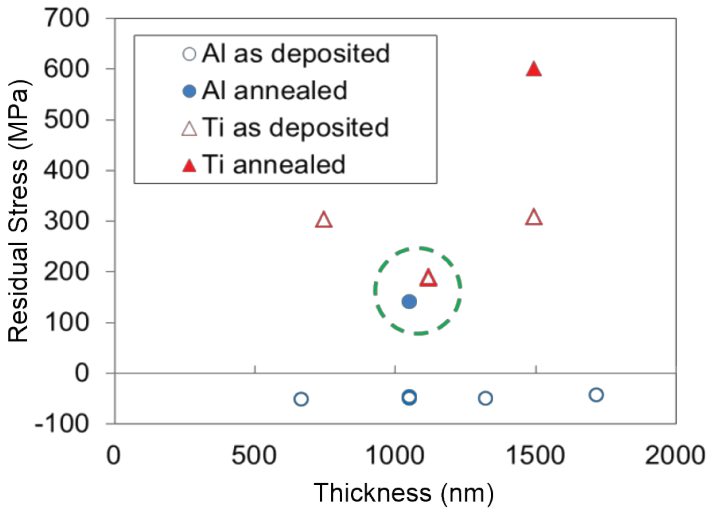

Figure 5.4 The effect of annealing on residual stress of Ti and Al thin films as a function of film thickness. Film stress is independent of thickness but becomes more tensile after annealing.

We measured compressive stress (~50 MPa) for the Al films and tensile stress (~200 MPa) for the Ti films. The compressive stress of the Al film could cause buckling during lift-off from the wafer. To mitigate the compressive stress we annealed the Al films at 200 °C for 2 hours in a nitrogen/hydrogen environment. After annealing, we measured tensile film stress (~200 MPa). The effect of annealing on residual film stress as a function of film thickness is summarized in Figure 5.4. Annealing results in more tensile stress in both Al and Ti samples. In Ti samples, growth of a TiN layer was observed by energy-dispersive X-ray spectroscopy and SEM observation (Appendix A.4). X-ray diffraction imaging after annealing showed

unchanged [1 1 1] texture and revealed the commonly observed peak doublet resulting from annealing [100] (Appendix A.4). While compressive stress could cause buckling during wafer lift-off, tensile stress does not significantly affect the fabrication of a low-CTE thin film array. As a result the Al films needed to be annealed prior to substrate lift-off. However, Ti annealing should be avoided to prevent the nitride layer growth.

5.6 Summary

As-deposited and annealed Al and Ti thin films were characterized by SEM, nanoindentation, XRD, and wafer curvature measurements. The results of this characterization are summarized in Table 5.3. The films were nanograined ($<$ 100 nm grains) and exhibited [1 1 1] texture. The texture contributed to the increased elastic modulus measured by nanoindentation. Annealing increased tensile stress in all films and residual stress was found to be independent of film thickness.

		Aluminum		**Titanium**	
		As deposited	Annealed	As deposited	Annealed
Grain size (nm)	SEM	80	-	92	-
Crystal size (nm)	XRD	22	-	39	-
Modulus (GPa)	Nanoindentation	79	-	135	-
Orientation	XRD	[1 1 1]	[1 1 1]	[1 1 1]	[1 1 1]
Stress (MPa)	Wafer curvature	-50	200	200	600

Table 5.3 Summary of characterization of Al and Ti thin films. The thin films were used as constituent materials of the Ti/Al low-CTE metastructure.

Chapter 6

LOW THERMAL EXPANSION THIN FILM METASTRUCTURE ARRAYS

In this chapter we present the fabrication, characterization, and demonstration of the unique thermal properties of ~1 μm thick bi-metallic thin films [102-104][1]. These thin film metastructures can lead to the development of low-cost, adaptive structures that operate in extreme thermal environments, such as reflective layers for space telescopes. Micro-electro-mechanical-system (MEMS) devices and packaging, and even flexible electronics may also benefit from this 2D, low-CTE bi-material array film, which could be used as buffer layers to minimize thermal fatigue and failure caused by CTE mismatch.

The design of these films is based on principles developed in Chapter 4 by using 3D finite element simulations while taking into account microfabrication

[1] This work was performed in collaboration with Dr. Namiko Yamamoto, Dr. Risaku Toda, and Dr. Victor White. E.E.G. conducted early fabrication attempts. N.Y., led sample fabrication with technical support from R.T. and V.W. E.E.G. ran and analyzed the simulations. N.Y. performed the experiments and analysis. N.Y. prepared the manuscript.

limitations. The films consist of a periodic array of Al hexagonal plates attached to a Ti frame. We successfully fabricated these discontinuous structured films by a unique combination of conventional micro-fabrication process steps, and measured their CTE to be -0.6 ppm/^{o}C using 3D DIC. Fabrication was accomplished by conventional microfabrication techniques such as photolithography, etching, lift-off, and metal deposition [105].

6.1 Fabrication of Free-Standing Thin Film Low-CTE Metastructure Arrays

We fabricated a free-standing 1 μm thin film low CTE metastructure using a combination of metal deposition, photolithography, metal lift-off, and dry etching. Figure 6.1a shows the target design of the thin film metastructure, while the fabricated and lifted-off structure is shown in Figure 6.1b.

The fabrication procedure can be broadly categorized in two steps: (i) fabricating the metastructure array on a substrate (steps 1-6 in Figure 6.2); and (ii) lifting off the array from the substrate (steps 7-9 in Figure 6.2).

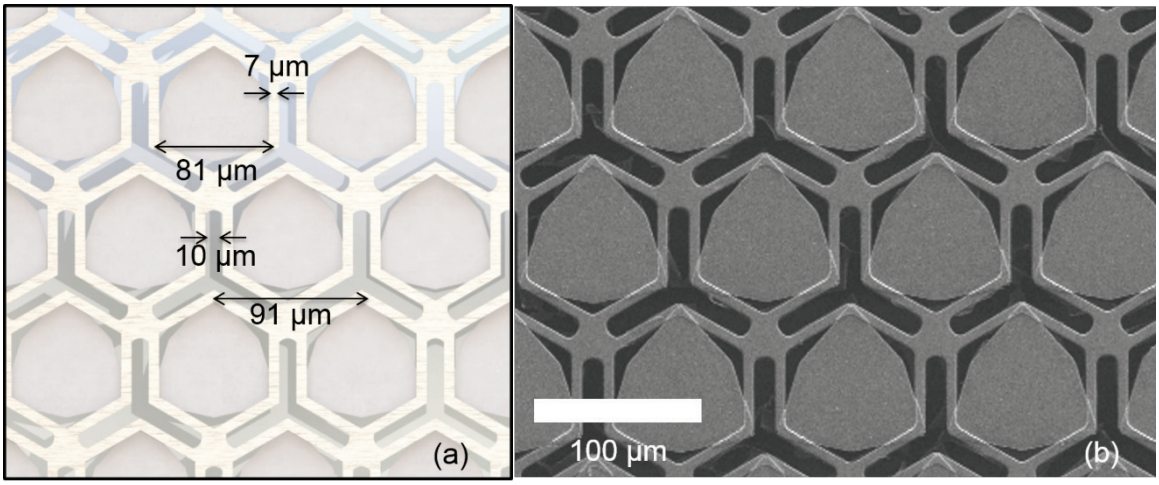

Figure 6.1 (a) Design of thin film low-CTE thin film metastructure. (b) SEM image of fabricated low-CTE metastructure after lift-off.

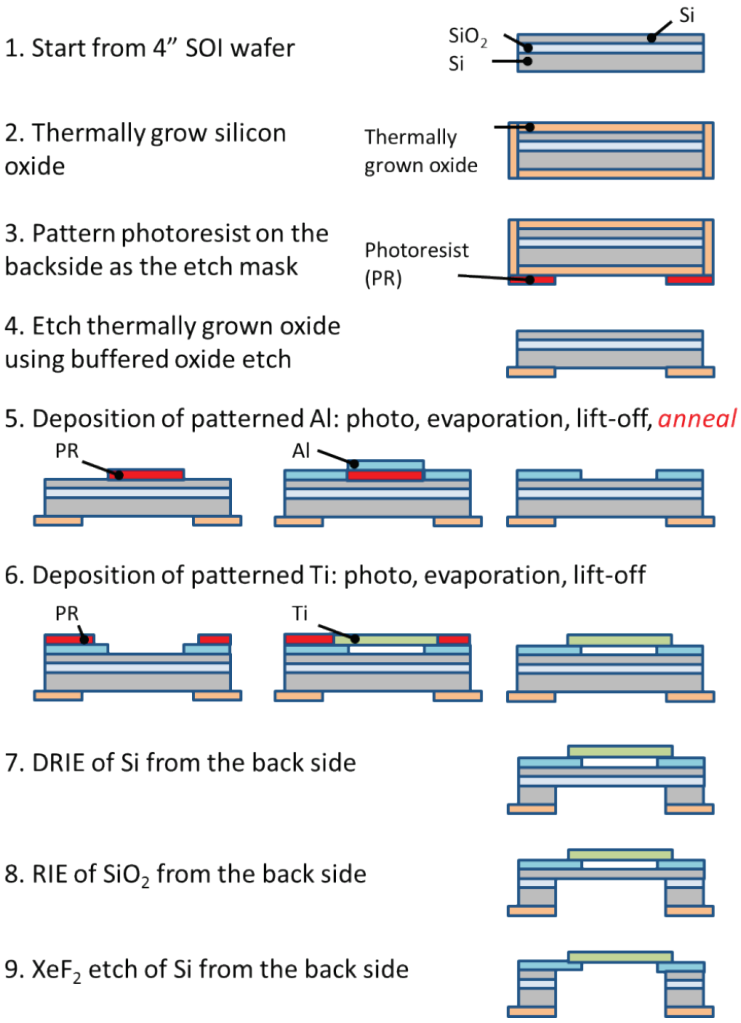

Figure 6.2 Process flow for fabrication of free-standing low-CTE thin film metastructure.

6.1.1 Fabrication of Low-CTE Thin Film Metastructure Arrays on a Substrate

The first fabrication step in the fabrication process is to thermally grow SiO_2 on an SOI wafer. An SOI (Silicon on Insulator) wafer contains a top layer of Si, an in-between layer of SiO_2 and a bottom layer of Si. SOI wafers are preferred to Si

wafers because the SiO_2 layer can be used as etch-stop in the substrate lift-off phase. SiO_2 is grown in a "wet" oxidation process characterized by the reaction $Si + 2H_2O \rightarrow SiO_2 + 2H_2$. The substrate is left in a water vapor (1000 °C) chamber for 15 hours. The resulting SiO_2 layer is ~2 μm thick. The SiO_2 is then patterned such that it consists of a ring on the backside of the wafer. The patterning is done by spin coating photoresist (AZ 5214E) on the SiO_2 on backside of the wafer, developing the photoresist, and etching away the SiO_2 in the unprotected areas with buffered oxide etch (BHF, 5:1 buffered HF) for about 1 hour. The SiO_2 ring is used as an etch mask in the substrate lift-off steps to maintain a substrate ring around the thin film metastructure for structural support.

Once the SiO_2 layer has been removed from the top surface of the wafer, a photolithography step is used to enable patterning of the Al layer via metal lift-off. It is important that Al is deposited first, so that it can be annealed without also annealing the Ti layer. For the lithography step AZ 5214E image reversal photoresist is spun onto wafer, exposed, and developed. Image reversal photoresists can behave like positive or negative photoresists depending on post-exposure treatment. Specifically for AZ 5214E, post-bake at 120 °C and a 10 s flood exposure after regular exposure will enable negative photoresist behavior. Negative photoresists exhibit negative wall profile, which is better suited for metal liftoff processes, such as the one we use here. After the wafer is patterned with photoresist, a nominally 1 μm thick Al film is deposited by E-beam evaporation. Then the wafer is placed in acetone, which is used to remove all photoresist. Metal deposited on top of the photoresist is removed ("lifted-off") and the desired Al pattern is left on the substrate. The Al film is then annealed at 200 °C. The patterned Ti film is then deposited on the substrate in the same way as the Al. Before the photoresist is exposed, the Ti mask is aligned to the Al patterned film. We ensure that the alignment step is good enough that there are always regions of overlap between the Al and Ti films in areas where the parts are joined.

After the Ti film is deposited, a photoresist speckle pattern is added for DIC testing. This is done by photolithography as described above. Photoresist speckles are ~5 μm in diameter.

6.1.2 Substrate Lift-off of Low-CTE Thin Film Metastructure Arrays

We tried methods such as gold or photoresist sacrificial layers and etching the substrate itself to achieve a free-standing film. Etching the substrate was the most successful method. Gold sacrificial layers did not work because the etchant could not penetrate between the metastructure and the substrate to remove the sacrificial layer (this problem can be modeled as Stokes flow). Photoresist sacrificial layers were not successful because the photoresist swelled when stripped, causing cracking in the film during lift-off.

We etched the substrate in three steps: (i) fast etching of the wafer's Si backside; (ii) etching of the SiO_2 "etch-stop" layer; and (iii) slow etching of the remaining Si layer behind the Ti/Al metastructure film.

The first step was achieved with deep reactive-ion etching (DRIE). Ion bombardment is the primary etching mechanism, resulting in anisotropic etch profiles. An SPTS Technologies system running the Bosch process was used. The Bosch process consists of two alternating steps, each lasting a few seconds: (i) an isotropic plasma etchant (SF_6) bombards the substrate vertically; (ii) an inert passivation layer (C_4F_8) is deposited. The alternating etching/passivation process results in a series of small isotropic etches, which result in an overall anisotropic etch profile. DRIE was used until the SiO_2 was encountered. The SiO_2 layer was necessary in order to stop the aggressive DRIE etching early enough to not damage the Ti/Al films. The DRIE process lasted ~2 hours to etch 200 μm of Si.

The SiO_2 layer was then removed with reactive-ion etching (RIE). Contrary to DRIE, RIE is a chemical etching process, wherein an ion plasma chemically reacts with the surface and etches it isotropically. RIE is a slower process than DRIE and was used to remove the bulk of the SiO_2 layer in a controlled fashion. The RIE process was performed at 10 mTorr with CHF_3 and O_2 flowing at 40 and 2 sccm, respectively; the electric field was created at 400 W. It took about 14 minutes to etch a ~1 μm SiO_2 layer.

The final step was removal of the Si layer behind the Ti/Al film with XeF_2 etching. XeF_2 isotropically etches Si through the reaction $2XeF_2 \rightarrow 2Xe + SiF_4$. XeF_2 is released in 60 s pulses and sequentially etches the substrate. This method was used as the final etching step because it would not significantly etch the Ti/Al film, though relatively slow etching of Ti was observed.

6.1.3 Free-standing Ti/Al Thin Film Metastructure Fabrication Summary and Discussion

Free-standing Ti/Al thin film metastructure arrays were successfully fabricated using a combination of conventional microfabrication techniques. Figure 6.3a shows a schematic broadly describing the fabrication method and Figure 6.3b shows an SEM image of the free-standing array. A circular 10 unit cell diameter thin film array was successfully released for the first time. The array's flatness was measured by optical interferometry to be within 200 nm, except for the areas where the Ti and Al films overlapped (Appendix A.4).

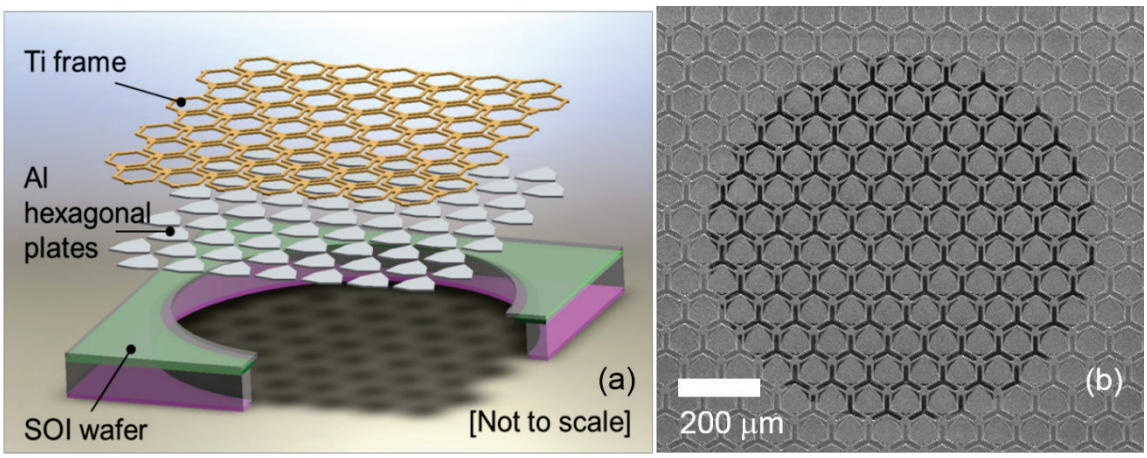

Figure 6.3 (a) Schematic showing fabrication process of free-standing Ti/Al thin film array. (b) SEM image (top view) of free-standing Ti/Al thin film array. A circular 10 unit cell diameter area was released from the substrate.

There are significant challenges in fabricating free-standing thin film arrays as compared to sheet metal structures, such as internal stresses, film fragility due to low thickness, and substrate release challenges. However, microfabrication also has advantages compared to the fabrication processes discussed in previous chapters. First, welding is avoided since the two metals alloy at their interface during deposition. Secondly, alignment between the two parts can be performed much more accurately and precisely thanks to the presence of microfabrication tools specifically for this purpose. Thirdly, by the nature of microfabrication, which is geared toward high aspect ratio 2D structures, a large number of unit cells can be fabricated in one step, compared to aligning and welding each part in the macroscale process. By leveraging these advantages of microfabrication it is possible to scale the procedure developed in this work to develop large thin film metastructure arrays at low cost.

6.2 Thermal Expansion of Thin Film Ti/Al Metastructure

We measured the CTE of the free-standing Ti/Al metastructure arrays by applying heat and measuring the displacements with DIC. The testing concept is similar to the one used in Chapter 4, though the size scale of the samples necessitated high magnification cameras for the DIC system. We also modeled the thermal deformation of the samples using FEM. Experimentally we measured the CTE to be -0.6 ppm/°C. The FEM model predicted 1.1 ppm/°C.

6.2.1 Experimental Setup

The experimental setup used to measure the CTE consisted of a stereo microscope attached to a heating stage and a thermocouple for temperature measurement (Figure 6.4). The 2D bi-metallic array samples were prepared with photoresist speckle patterns of ~4 μm. The samples were heated from room temperature to ~185 °C, and magnified images were recorded from two angles through a stereo microscope. The stereo microscope has a ~800 μm field of view and an in-plane spatial resolution of ~5-10 nm. The displacement noise was evaluated by taking multiple stationary images of a sample. Noise was less than ~2 nm (in-plane), compared to the expected displacement range of 5 - 15 nm.

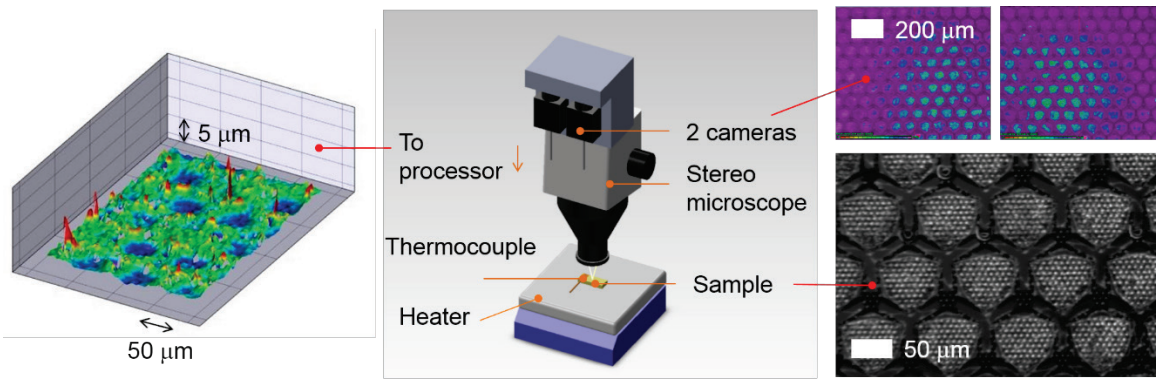

Figure 6.4 3D digital image correlation with a stereomicroscope to map small thermal displacement: (center) schematic of the set-up; (right bottom) a sample prepared with photoresist speckle pattern; (right top) 2D images of a sample taken from two different angles; and (left) 3D image constructed with DIC to show the out-of-plane displacement.

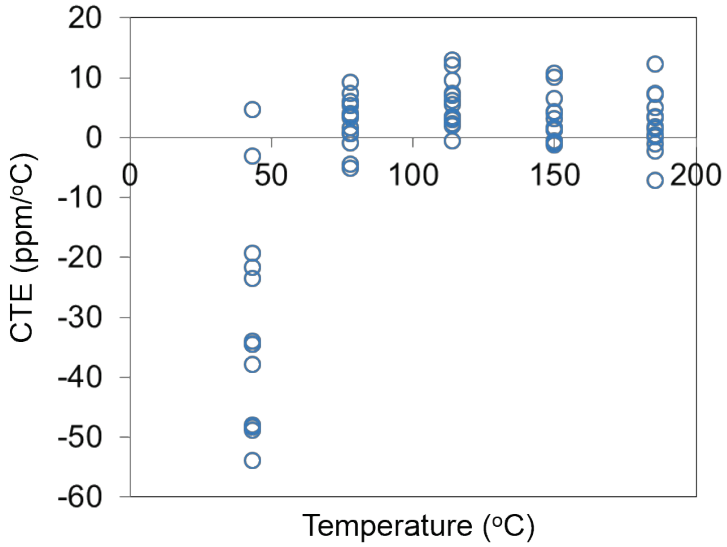

Figure 6.5 Experimental measurement of Si wafer CTE as a function of temperature. As expected, variability in the CTE measurement deceases when the CTE is computed at temperatures greater than 45 °C.

CTEs were calculated by computing the strain between two points and dividing by the temperature difference. Data points were taken at scattered locations across the sample surface, at six set temperatures (room temperature, ~45 °C, ~80 °C, ~115°C, ~150 °C, ~185 °C).

The accuracy of this measurement technique was evaluated using a Si wafer prepared with the same speckle pattern. Based on 65 data points, the CTE of the Si wafer was calculated to be 1.8 ppm/°C (median), ~31% lower than the literature CTE value of [1 0 0] Si (2.6 ppm/°C). To assess the quality of the CTE measurement we plotted the calculated CTE as a function of temperature (Figure 6.5). As shown in 5.3.1.2, variability in the CTE is highest at low temperatures (~45 °C). At small ΔT, the thermal displacement is very small (~ 2 nm), and cannot be properly distinguished from noise (~2 nm). When the data points taken at ~45 °C are eliminated, scattering significantly decreased, and the new Si CTE was computed to be 3.3 ppm/°C.

6.2.2 CTE of the Thin Film Ti/Al Metastructure Array

The CTE of the Ti/Al metastructure array was measured across 250 low-CTE nodes (Ti frame connection nodes, and centers of Al plates) scattered points on the sample by computing the strain and dividing by the temperature difference for five temperature sets up to ~185 °C.

We also simulated the thermal deformation of the thin film metastructure with a 4.5 unit cell diameter, symmetric FEM model. The Si substrate ring was modeled as a displacement boundary condition. The displacement magnitude was computed based on the CTE of Si and temperature difference applied. Out-of-plane displacement was set zero at the boundary. The direction was radially outward. The validity of this boundary condition hinges on the assumption that the response

of the thin film at the boundary is dominated by the substrate. The substrate is more than 100 times thicker than the film, supporting the assumption.

CTE (ppm/°C)	**Al**	**Ti**	**Ti/Al array**	
	Literature [68]	Literature [68]	FEM	Experimental
	23.1	**8.6**	**1.19**	**-0.6**

Table 6.1 Experimental measurements and computational predictions of the Ti/Al thin film metastructure array. The Ti/Al array exhibits slightly negative CTE, significantly lower than its constituents.

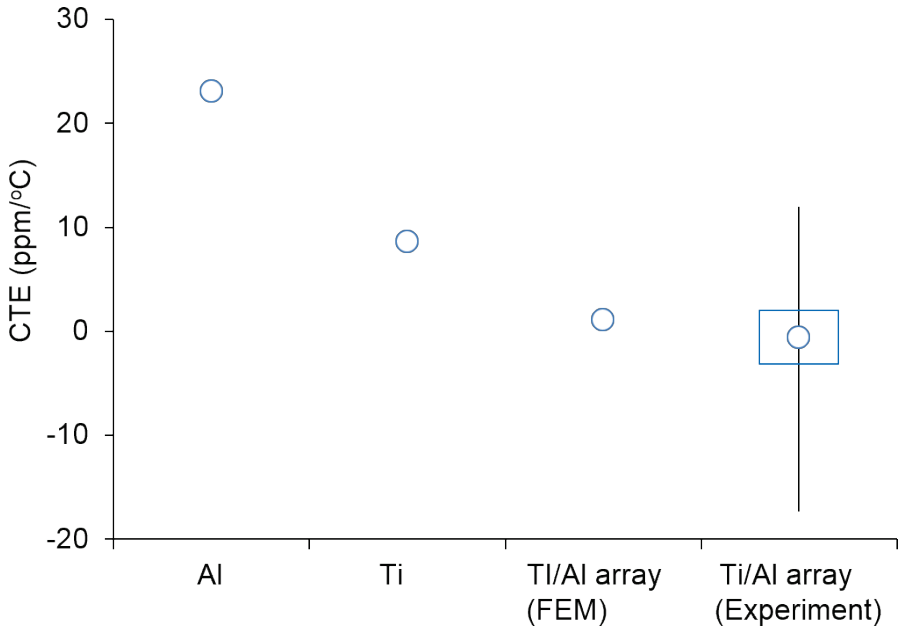

Figure 6.6 Measured Ti/Al metastructure array CTE compared with reference and simulated values. Circles show median values, the box shows the 25/75th percentile and the line shows extreme values.

The experimental measurements and computational predictions of the Ti/Al thin film metastructure CTEs are summarized in Table 6.1 and shown in Figure 6.6. The measured value (-0.6 ppm/°C) of the 2D bi-metallic lattice is comparable to,

but slightly lower than the FEM predicted CTE value (1.19 ppm/°C). We attribute this discrepancy to the following two factors: (i) differences between the experimental sample set-up and the simulation; and (ii) error and uncertainty in measurement technique. One main difference between the model and experiments is the lap joint at the Al and Ti interface. As a product of the deposition process, the Al and Ti films lie in the same plane, except at the joint. However, the FEM models the two parts in different planes. Another main difference between the experimental setup and the FEM model is the uniformity of temperature across the sample. While temperature variation is modeled as completely uniform, it is possible that this is not the case experimentally. A third difference between the FEM model and experiments is that the FEM model does not contain internal stresses which are present in the fabricated structure. Regarding measurement uncertainty, the experimental technique was shown to accurately measure the CTE of Si to within 0.7 ppm/°C, but with high variance. The CTE modeled with FEM is within the $25/75^{\text{th}}$ percentile of experimental measurements.

The FEM model predicts increasing CTE radially outward from the center of the metastructure array as the simulated Si boundary gets closer. This effect is also seen experimentally. Out-of-plane deformation measured experimentally with 3D DIC was ~1 μm, while the FEM model predicted ~2-4 μm out-of-plane deformation. One reason that the out-of-plane deformation observed experimentally is lower than the FEM's prediction is the lap joint interface. Experimentally, the two materials are in the same plane (except at the interface), whereas in the FEM model they are in different planes, which would increase out-of-plane deformation. Nonetheless, the experiments and FEM results (Appendix A.5) agree within experimental error.

6.3 Summary

We successfully developed, for the first time, a thin film metastructure designed to have low CTE with a large application temperature range. We used FEM simulations to develop the metastructure and the experimentally measured response in agreement with the FEM prediction. We developed a scalable microfabrication procedure to reliably fabricate this discontinuous thin film array. We controlled the film residual stress by annealing and the film was released from the substrate by etching the substrate with DRIE, RIE, and XeF_2. We experimentally confirmed low effective CTE (-0.6 ppm/^{o}C) for this metastructure array.

This flexible, low-cost, low-weight metastructure can be applied in areas such as fine-precision devices in thermally harsh environments and MEMS devices requiring thermal buffer layers. Beyond the current sample, material selection and lattice design can be tailored to suit the application temperature range and the aimed CTE range as in Chapter 4 for macroscale structures.

Chapter 7

CONCLUSION

In this thesis, we develop and understand the mechanics of thin foil and thin film metastructures that exhibit low and negative CTE. We experimentally demonstrate that the thermal behavior of these metastructures agrees with computational predictions and that desired thermal response can be achieved through appropriate design.

In Chapter 3, we studied the thermal response of thin foil Ti/Al metastructure unit cells. We demonstrated experimentally bi-material metastructures exhibiting CTE of 2.6 ppm/°C, significantly lower than that of their constituents. We developed a 3D FEM model to accurately predict the thermal response of these metastructures. We computationally showed fine and coarse control of the CTE from -3.6 to 8.4 ppm/°C by varying three key design parameters (α_1, α_2, and the frame beam width). We developed a robust fabrication procedure for high aspect ratio metastructures enabling new designs and geared toward ultimately developing large structures of arbitrary CTE.

In Chapter 4, we designed, fabricated, and thermally characterized low and negative CTE, high aspect ratio (~570) Ti/Al and Kovar/Al metastructure arrays in good agreement with FEM results. We used photolithographic patterning and laser-welding to fabricate these metastructures. These techniques enabled precise and repeatable feature control in the desired size scale. We developed a robust experimental setup using DIC and an IR camera to obtain full-field measurement of displacements and temperature during testing. The full-field temperature and

displacement information enabled direct comparison with FEM which led to further understanding of the inhomogeneous thermal deformation within an array.

In Chapter 5, we characterized Ti and Al thin films as potential constituents of a thin film low-CTE metastructure. We used SEM, nanoindentation, XRD, and wafer curvature measurements to determine the lattice structure and mechanical properties of as-deposited and annealed Al and Ti thin films. We used this information to inform the design and fabrication of thin film low-CTE metastructures.

In Chapter 6, we discuss the development of a thin film Ti/Al metastructure array designed to have low CTE. FEM simulations were used to design the metastructure; the experimental response is shown to be in agreement with computational predictions. We discuss the development of a scalable microfabrication procedure to reliably fabricate high aspect ratio, thin film metastructure arrays. The films were released from the substrate by etching the substrate with DRIE, RIE, and XeF_2. Low effective CTE for this metastructure array was experimentally confirmed (-0.6 ppm/^{o}C).

The discovery and characterization of metastructures with engineered CTE will aid in applications where thermal strains may cause failure or decreased performance, such as aerospace, solar energy, and semiconductor applications. In particular, the size scale of the metastructures developed in this work enables application in MEMS, solar cells, biomedical devices, and thermally stable optics. Additionally, the ideas explored can be applied in the future to develop more complex metastructures, such as anisotropic CTE by design in three dimensions. The principles developed in this work can be applied to engineer properties of metastructures beyond CTE.

BIBLIOGRAPHY

[1] R. Roy, D. K. Agrawal, and H. A. Mckinstry, "Very Low Thermal-Expansion Coefficient Materials," *Annual Review of Materials Science,* vol. 19, pp. 59-81, 1989.

[2] W. Miller, C. W. Smith, D. S. Mackenzie, and K. E. Evans, "Negative Thermal Expansion: A Review," *Journal of Materials Science,* vol. 44, pp. 5441-5451, Oct 2009.

[3] A. W. Sleight, "Negative Thermal Expansion Materials," *Current Opinion in Solid State & Materials Science,* vol. 3, pp. 128-131, Apr 1998.

[4] A. Spadoni and C. Daraio, "Generation and Control of Sound Bullets with a Nonlinear Acoustic Lens," *Proceedings of the National Academy of Sciences of the United States of America,* vol. 107, pp. 7230-7234, Apr 20 2010.

[5] D. R. Smith, J. B. Pendry, and M. C. K. Wiltshire, "Metamaterials and Negative Refractive Index," *Science,* vol. 305, pp. 788-792, Aug 6 2004.

[6] N. Boechler, G. Theocharis, and C. Daraio, "Bifurcation-Based Acoustic Switching and Rectification," *Nature Materials,* vol. 10, pp. 665-668, Sep 2011.

[7] K. Kuribara, H. Wang, N. Uchiyama, K. Fukuda, T. Yokota, U. Zschieschang*, et al.*, "Organic Transistors with High Thermal Stability for Medical Applications," *Nature Communications,* vol. 3, p. 723, Mar 2012.

[8] J. Ishii and T. Akamatsu, "Organo-Soluble Low CTE Polyimides and their Applications to Photosensitive Cover Layer Materials in Flexible Printed Circuit Boards," *High Performance Polymers,* vol. 21, pp. 123-138, Apr 2009.

[9] C. Zweben, "Advances in Composite Materials for Thermal Management in Electronic Packaging," *JOM,* vol. 50, pp. 47-51, 1998/06/01 1998.

[10] A. Bollero, L. Kaupmees, T. Raadik, M. Grossberg, and S. Fernandez, "Thermal Stability of Sputtered Mo/Polyimide Films and Formation of MoSe2 and MoS2 Layers for Application in Flexible Cu(In,Ga)(Se,S)(2) Based Solar Cells," *Thin Solid Films,* vol. 520, pp. 4163-4168, Apr 2012.

[11] M. D. Griffin and J. R. French, *Space Vehicle Design*. Washington, DC: American Institute of Aeronautics and Astronautics, 1991.

[12] M. M. Micci and A. D. Ketsdever, *Micropropulsion for Small Spacecraft*. Reston, Va.: American Institute of Aeronautics and Astronautics, 2000.

[13] J. E. Ayers, *Digital Integrated Circuits : Analysis and Design*, 2nd ed. Boca Raton: CRC Press, 2010.

[14] P. R. Yoder, *Opto-Mechanical Systems Design*, 3rd ed. Bellingham, Wash. Boca Raton, FL: SPIE Press ; CRC/Taylor & Francis, 2006.

[15] M. L. Minges and ASM International. Handbook Committee., *Electronic Materials Handbook*. Materials Park, OH: ASM International, 1989.

[16] R. S. Narayanan and A. W. Beeby, *Introduction to Design for Civil Engineers*. London ; New York: E & FN Spon, 2000.

[17] M. Gad-el-Hak, *MEMS : Design and Fabrication*, 2nd ed. Boca Raton, FL: CRC/Taylor & Francis, 2006.

[18] D. D. L. Chung, *Materials for Electronic Packaging*. Boston: Butterworth-Heinemann, 1995.

[19] L. Noethe, "History of Mirror Casting, Figuring, Segmentation and Active Optics," *Experimental Astronomy,* vol. 26, pp. 1-18, Aug 2009.

[20] O. Sigmund and S. Torquato, "Composites with Extremal Thermal Expansion Coefficients," *Applied Physics Letters,* vol. 69, pp. 3203-3205, Nov 18 1996.

[21] R. Lakes, "Cellular Solid Structures with Unbounded Thermal Expansion," *Journal of Materials Science Letters,* vol. 15, pp. 475-477, Mar 15 1996.

[22] C. A. Steeves, S. L. D. S. E. Lucato, M. He, E. Antinucci, J. W. Hutchinson, and A. G. Evans, "Concepts for Structurally Robust Materials that Combine Low Thermal Expansion with High Stiffness," *Journal of the Mechanics and Physics of Solids,* vol. 55, pp. 1803-1822, Sep 2007.

[23] J. Berger, C. Mercer, R. M. McMeeking, and A. G. Evansz, "The Design of Bonded Bimaterial Lattices that Combine Low Thermal Expansion with High Stiffness," *Journal of the American Ceramic Society,* vol. 94, pp. S42-S54, Jun 2011.

[24] C. Y. Ho and R. E. Taylor, *Thermal Expansion of Solids*. Materials Park, OH: ASM International, 1998.

[25] J. L. Cribb, "Shrinkage and Thermal Expansion of a 2 Phase Material," *Nature,* vol. 220, pp. 576-&, 1968.

[26] L. J. Gibson and M. F. Ashby, *Cellular Solids: Structure and Properties*, 2nd ed. Cambridge ; New York: Cambridge University Press, 1997.

[27] R. Lakes, "Foam Structures with a Negative Poissons Ratio," *Science,* vol. 235, pp. 1038-1040, Feb 27 1987.

[28] O. Sigmund and S. Torquato, "Design of Materials with Extreme Thermal Expansion Using a Three-Phase Topology Optimization Method," *Journal of the Mechanics and Physics of Solids,* vol. 45, pp. 1037-1067, Jun 1997.

[29] C. A. Steeves, C. Mercer, E. Antinucci, M. Y. He, and A. G. Evans, "Experimental Investigation of the Thermal Properties of Tailored Expansion Lattices," *International Journal of Mechanics and Materials in Design,* vol. 5, pp. 195-202, 2009.

[30] C. A. Steeves and A. G. Evans, "Optimization of Thermal Protection Systems Utilizing Sandwich Structures with Low Coefficient of Thermal Expansion Lattice Hot Faces," *Journal of the American Ceramic Society,* vol. 94, pp. s55-s61, 2011.

[31] G. Mie, "Kinetic theory of monatomic bodies," *Annalen Der Physik,* vol. 11, pp. 657-697, Jun 1903.

[32] E. Gruneisen, "The connection between compressibility, thermal expansion, atomic volumes and the atom volume and atomic heat of metals," *Annalen Der Physik,* vol. 26, pp. 393-402, Jun 1908.

[33] E. Gruneisen, "The thermic elongation and the specific heat of metals," *Annalen Der Physik,* vol. 26, pp. 211-216, May 1908.

[34] E. Gruneisen, "Theory of the solid condition in one atom elements.," *Annalen Der Physik,* vol. 39, pp. 257-306, Sep 1912.

[35] J. Ishii, A. Takata, Y. Oami, R. Yokota, L. Vladimirov, and M. Hasegawa, "Spontaneous molecular orientation of polyimides induced by thermal imidization (6). Mechanism of negative in-plane CTE generation in non-stretched polyimide films," *European Polymer Journal,* vol. 46, pp. 681-693, Apr 2010.

[36] M. K. Ghosh and K. L. Mittal, *Polyimides : fundamentals and applications*. New York: Marcel Dekker, 1996.

[37] F. H. Gillery and E. A. Bush, "Thermal Contraction of Beta-Eucryptite (Li2o.Al2o3.2sio2) by X-Ray and Dilatometer Methods," *Journal of the American Ceramic Society,* vol. 42, pp. 175-177, 1959.

[38] C. T. Li and D. R. Peacor, "Crystal Structure of Lialsi2o6-2 (Beta Spodumene)," *Zeitschrift Fur Kristallographie Kristallgeometrie Kristallphysik Kristallchemie,* vol. 126, pp. 46-&, 1968.

[39] H. Schulz, "Thermal-Expansion of Beta Eucryptite," *Journal of the American Ceramic Society,* vol. 57, pp. 313-318, 1974.

[40] Schott. (2011). *Zerodur: Zero Expansion Glass Ceramic*. Available: http://www.us.schott.com/advanced_optics/english/download/schott_zerodur_katalog_july_2011_us.pdf

[41] ECSO. (2012). *Zerodur Ultra-Stable Laser Quality Mirrors*. Available: http://www.escooptics.com/mirrors/precision-laser-quality-mirror/zerodur-mirrors-uncoated

[42] C. E. Guillaume, *Comptes Rendus de l'Académie des Sciences,* vol. 125, pp. 235-238, 1897.

[43] E. F. Wassermann, "New Developments on the Invar-Effect," *Physica Scripta,* vol. T25, pp. 209-219, 1989.

[44] E. F. Wassermann, M. Acet, and W. Pepperhoff, "Moment Instabilities and Structural Phase-Transitions in 3d-Alloys," *Journal of Magnetism and Magnetic Materials,* vol. 90-1, pp. 126-130, Dec 1990.

[45] V. Crisan, P. Entel, H. Ebert, H. Akai, D. D. Johnson, and J. B. Staunton, "Magnetochemical origin for Invar anomalies in iron-nickel alloys," *Physical Review B,* vol. 66, Jul 1 2002.

[46] D. G. Rancourt and M. Z. Dang, "Relation between anomalous magnetovolume behavior and magnetic frustration in Invar alloys," *Physical Review B,* vol. 54, pp. 12225-12231, Nov 1 1996.

[47] R. J. Weiss, "Origin of Invar Effect," *Proceedings of the Physical Society of London,* vol. 82, pp. 281-&, 1963.

[48] V. L. Moruzzi, P. M. Marcus, K. Schwarz, and P. Mohn, "Ferromagnetic Phases of Bcc and Fcc Fe, Co, and Ni," *Physical Review B,* vol. 34, pp. 1784-1791, Aug 1 1986.

[49] L. Harner. (1997). *After 100 Years, The Uses for Invar Continue to Multiply*. Available: http://www.cartech.com/techarticles.aspx?id=1664

[50] United States. National Bureau of Standards, *Invar and Related Nickel Steels*, 1st ed. Washington,: Govt. print. off., 1916.

[51] W. Martienssen and H. Warlimont, *Springer handbook of condensed matter and materials data*. Heidelberg ; New York: Springer, 2005.

[52] E. H. Kerner, "The Elastic and Thermo-Elastic Properties of Composite Media," *Proceedings of the Physical Society of London Section B,* vol. 69, pp. 808-813, 1956.

[53] Z. Hashin and S. Shtrikman, "A Variational Approach to the Theory of the Elastic Behaviour of Multiphase Materials," *Journal of the Mechanics and Physics of Solids,* vol. 11, pp. 127-140, 1963.

[54] G. W. Milton and R. V. Kohn, "Variational Bounds on the Effective Moduli of Anisotropic Composites," *Journal of the Mechanics and Physics of Solids,* vol. 36, pp. 597-629, 1988.

[55] B. W. Rosen and Z. Hashin, "Effective Thermal Expansion Coefficients and Specific Heats of Composite Materials," *International Journal of Engineering Science,* vol. 8, pp. 157-&, 1970.

[56] L. V. Gibiansky and S. Torquato, "Thermal Expansion of Isotropic Multiphase Composites and Polycrystals," *Journal of the Mechanics and Physics of Solids,* vol. 45, pp. 1223-1252, Jul 1997.

[57] G. W. Milton, *The Theory of Composites*. Cambridge ; New York: Cambridge University Press, 2002.

[58] G. Jefferson, R. J. Kerans, and T. A. Parthasarathy, "Bi-Material Composite Structure with Reduced Thermal Expansion," ed: Google Patents, 2012.

[59] S. Timoshenko, "Analysis of Bi-Metal Thermostats," *Journal of the Optical Society of America and Review of Scientific Instruments,* vol. 11, pp. 233-255, Sep 1925.

[60] E. Suhir, "Stresses in Bimetal Thermostats," *Journal of Applied Mechanics-Transactions of the Asme,* vol. 53, pp. 657-660, Sep 1986.

[61] J. Chu, "Topics in Designing Low Thermal Expansion Lattices at the Microscale," Master's Thesis, Graduate Department of Aerospace Science and Engineering, University of Toronto, 2011.

[62] E. E. Gdoutos, A. A. Shapiro, and C. Daraio, "Thin and Thermally Stable Periodic Metastructures," *Experimental Mechanics, In Press,* 2013.

[63] K. Patterson and S. Pellegrino, "Shape Correction of Thin Mirrors," in *52nd AIAA/ASME/ASCE/AHS/ASC Structures, Structural Dynamics and Materials Conference*, Denver, Colorado, 2011.

[64] K. Patterson, S. Pellegrino, and J. Breckinridge, "Shape Correction of Thin Mirrors in a Reconfigurable Modular Space Telescope," *Space Telescopes and Instrumentation 2010: Optical, Infrared, and Millimeter Wave,* vol. 7731, 2010.

[65] (2010). *SIMULIA web site. Dassault Systemes - Abaqus FEA*.

[66] J. Fish and T. Belytschko, *A First Course in Finite Elements*. Chichester, England ; Hoboken, NJ: John Wiley & Sons Ltd., 2007.

[67] *Dassault Systemes - Abaqus Theory Manual* 2011.

[68] W. M. Haynes, Ed., *CRC Handbook of Chemistry and Physics* (CRC Handbook of Chemistry and Physics. Boca Raton, FL: CRC Press, Taylor and Francis, 2009, p.^pp. Pages.

[69] J. N. Reddy, *An Introduction to the Finite Element Method*, 2nd ed. New York: McGraw-Hill, 1993.

[70] V. Birman, *Plate Structures*. New York: Springer, 2011.

[71] M. A. Sutton, W. J. Wolters, W. H. Peters, W. F. Ranson, and S. R. McNeill, "Determination of Displacements Using an Improved Digital Correlation Method," *Image and Vision Computing,* vol. 1, pp. 133-139, 1983.

[72] T. C. Chu, W. F. Ranson, and M. A. Sutton, "Applications of Digital-Image-Correlation Techniques to Experimental Mechanics," *Experimental Mechanics,* vol. 25, pp. 232-244, 1985/09/01 1985.

[73] "Vic2D 2009," ed. Columbia, SC: Correlated Solutions, Inc., 2009.

[74] "JMP," ed. Cary, NC: SAS Institute Inc, 2007.

[75] R. C. Team, "R: A Language and Environment for Statistical Computing," R. F. f. S. Computing, Ed., ed. Vienna, Austria, 2012.

[76] M. Pecht, *Electronic Packaging Materials and their Properties*. Boca Raton: CRC Press, 1999.

[77] PEI. (2013). *Photofabrication Engineering Inc.* . Available: http://www.photofabrication.com/

[78] X. Maldague, *Theory and Practice of Infrared Technology for Nondestructive Testing*. New York ;: Wiley, 2001.

[79] FLIR. *SC6000 Datasheet*. Available: http://www.flir.com/thermography/americas/us/view/?id=44791

[80] M. Q. Brewster, *Thermal Radiative Transfer and Properties*. New York: Wiley, 1992.

[81] H. Kaplan, *Practical Applications of Infrared Thermal Sensing and Imaging Equipment*, 3rd ed. Bellingham, Wash.: SPIE Press, 2007.

[82] H. N. G. Wadley, N. A. Fleck, and A. G. Evans, "Fabrication and Structural Performance of Periodic Cellular Metal Sandwich Structures," *Composites Science and Technology,* vol. 63, pp. 2331-2343, Dec 2003.

[83] G. G. Stoney, "The Tension of Metallic Films Deposited by Electrolysis," *Proceedings of the Royal Society of London Series A* vol. 82, pp. 172-175, May 1909.

[84] *Standard Test Methods for Determining Average Grain Size*. West Conshohocken, PA: ASTM International, 2013.

[85] E. O. Hall, "The Deformation and Ageing of Mild Steel. 3. Discussion of Results," *Proceedings of the Physical Society of London Section B,* vol. 64, pp. 747-753, 1951.

[86] N. J. Petch, "The Cleavage Strength of Polycrystals," *Journal of the Iron and Steel Institute,* vol. 174, pp. 25-28, 1953.

[87] R. Abbaschian, L. Abbaschian, and R. E. Reed-Hill, *Physical Metallurgy Principles*, 4th ed. Stamford, CT: Cengage Learning, 2010.

[88] M. A. Haque and M. T. A. Saif, "Mechanical Behavior of 30-50 nm Thick Aluminum Films under Uniaxial Tension," *Scripta Materialia,* vol. 47, pp. 863-867, Dec 9 2002.

[89] G. Palumbo, S. J. Thorpe, and K. T. Aust, "On the Contribution of Triple Junctions to the Structure and Properties of Nanocrystalline Materials," *Scripta Metallurgica Et Materialia,* vol. 24, pp. 1347-1350, Jul 1990.

[90] T. Tsuchiya, M. Hirata, and N. Chiba, "Young's Modulus, Fracture Strain, and Tensile Strength of Sputtered Titanium Thin Films," *Thin Solid Films,* vol. 484, pp. 245-250, Jul 22 2005.

[91] Y. Kuru, M. Wohlschlogel, U. Welzel, and E. J. Mittemeijer, "Crystallite Size Dependence of the Coefficient of Thermal Expansion of Metals," *Applied Physics Letters,* vol. 90, Jun 11 2007.

[92] M. M. de Lima, R. G. Lacerda, J. Vilcarromero, and F. C. Marques, "Coefficient of Thermal Expansion and Elastic Modulus of Thin Films," *Journal of Applied Physics,* vol. 86, pp. 4936-4942, Nov 1 1999.

[93] O. Kraft and W. D. Nix, "Measurement of the Lattice Thermal Expansion Coefficients of Thin Metal Films on Substrates," *Journal of Applied Physics,* vol. 83, pp. 3035-3038, Mar 15 1998.

[94] M. Janda, "Elasticity Modulus and Temperature Expansion Coefficient of Aluminum Thin Films Measured by a New Method," *Thin Solid Films,* vol. 112, pp. 219-225, 1984.

[95] R. Saha and W. D. Nix, "Effects of the Substrate on the Determination of Thin Film Mechanical Properties by Nanoindentation," *Acta Materialia,* vol. 50, pp. 23-38, Jan 8 2002.

[96] M. Chinmulgund, R. B. Inturi, and J. A. Barnard, "Effect of Ar Gas Pressure on Growth, Structure, and Mechanical Properties of Sputtered Ti, Al, TiAl, and Ti3Al films," *Thin Solid Films,* vol. 270, pp. 260-263, Dec 1 1995.

[97] W. C. Oliver and G. M. Pharr, "An Improved Technique for Determining Hardness and Elastic-Modulus Using Load and Displacement Sensing Indentation Experiments," *Journal of Materials Research,* vol. 7, pp. 1564-1583, Jun 1992.

[98] W. C. Oliver and G. M. Pharr, "Measurement of Hardness and Elastic Modulus by Instrumented Indentation: Advances in Understanding and Refinements to Methodology," *Journal of Materials Research,* vol. 19, pp. 3-20, Jan 2004.

[99] T. Y. Tsui and G. M. Pharr, "Substrate Effects on Nanoindentation Mechanical Property Measurement of Soft Films on Hard Substrates," *Journal of Materials Research,* vol. 14, pp. 292-301, Jan 1999.

[100] B. D. Cullity and S. R. Stock, *Elements of X-Ray Diffraction*, 3rd ed. Upper Saddle River, NJ: Prentice Hall, 2001.

[101] X. Feng, Y. Huang, and A. J. Rosakis, "On the Stoney Formula for a Thin Film/Substrate System with Nonuniform Substrate Thickness," *Journal of Applied Mechanics-Transactions of the Asme,* vol. 74, pp. 1276-1281, Nov 2007.

[102] N. Yamamoto, E. E. Gdoutos, and C. Daraio, "Fabrication and Characterization of 2D Bi-metallic, Structured Films with Ultra-low Thermal Expansion," presented at the SEM 2013 Annual Conference & Exposition on Experimental and Applied Mechanics, Lombard, IL, 2013.

[103] N. Yamamoto, E. E. Gdoutos, and C. Daraio, "Engineered Thin Films with Ultra-low Thermal Expansion Coefficient for Deformable Space Structures " presented at the 54th Structures, Structural Dynamics, and Materials and Co-located Conferences, Boston, MA, 2013.

[104] N. Yamamoto, E. E. Gdoutos, R. Toda, V. White, H. Manohara, and C. Daraio, "A Thin Film Metamaterial Consisting of Metallic Lattices: Tunable CTE for Thermal Stability," *In preparation,* 2013.

[105] M. J. Madou, *Fundamentals of Microfabrication and Nanotechnology*, 3rd ed. Boca Raton, FL: CRC Press, 2012.

APPENDIX

A.1 Metastructure Design

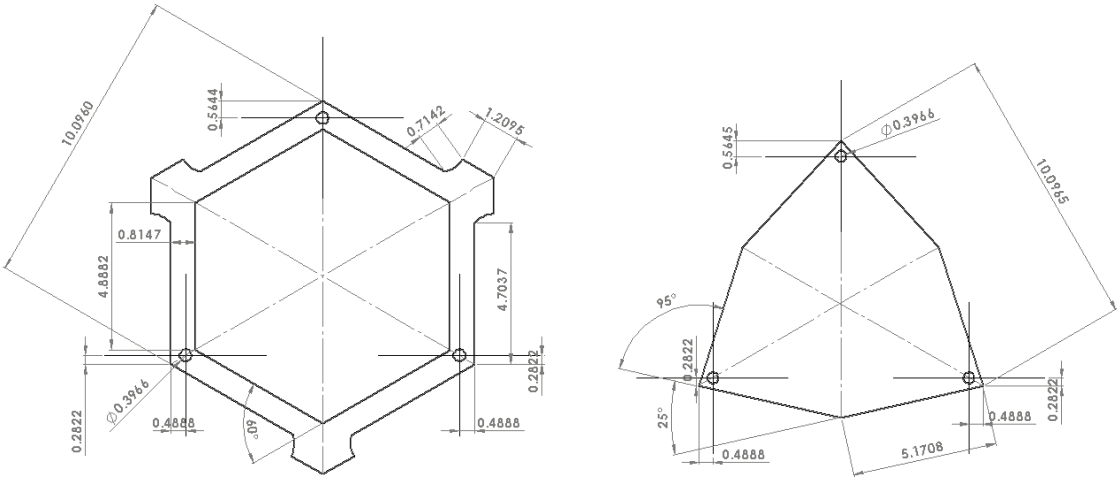

Figure A.1.1. Engineering drawings of the Ti frame (left) and Al plate (right) for a Ti/Al low CTE metastructure

A.2 Sensitivity Analysis Dataset

α_1 (ppm/°C)	α_2 (ppm/°C)	f_{width} (mm)	$A_{contact}$ (μm)	E_1 (GPa)	E_2 (GPa)	CTE (1/°C)
8.6	23.1	0.915	200	116	70	6.05E-07
9.6	23.1	0.815	200	116	70	1.64E-06
7.6	22.1	0.915	300	126	60	-1.47E-07
9.6	24.1	0.715	300	126	80	6.83E-07
9.6	24.1	0.715	300	106	60	7.26E-07
8.6	23.1	0.815	100	116	70	3.35E-08
7.6	22.1	0.915	300	106	80	-4.40E-07
8.6	23.1	0.815	200	116	60	1.46E-07
9.6	24.1	0.915	300	126	60	1.84E-06

9.6	22.1	0.915	300	126	80	2.74E-06
7.6	24.1	0.915	100	106	80	-1.66E-06
7.6	24.1	0.715	300	126	60	-2.38E-06
9.6	22.1	0.915	100	106	80	2.59E-06
9.6	24.1	0.715	100	126	60	6.42E-07
8.6	23.1	0.815	200	116	80	-1.38E-08
8.6	23.1	0.815	300	116	70	1.65E-07
7.6	24.1	0.715	100	126	80	-2.76E-06
8.6	23.1	0.815	200	126	70	1.03E-07
8.6	24.1	0.815	200	116	70	-5.34E-07
7.6	22.1	0.715	300	126	80	-1.29E-06
7.6	22.1	0.715	100	126	60	-1.36E-06
9.6	24.1	0.915	100	106	60	1.67E-06
9.6	22.1	0.715	100	106	60	1.81E-06
9.6	22.1	0.915	300	106	60	2.80E-06
9.6	22.1	0.715	100	126	80	1.76E-06
8.6	23.1	0.815	200	106	70	8.95E-09
9.6	22.1	0.715	300	126	60	2.00E-06
7.6	22.1	0.715	100	106	80	-1.57E-06
9.6	24.1	0.915	300	106	80	1.55E-06
9.6	24.1	0.915	100	126	80	1.58E-06
7.6	22.1	0.915	100	106	60	-3.33E-07
9.6	24.1	0.715	100	106	80	4.33E-07
7.6	23.1	0.815	200	116	70	-1.53E-06
7.6	24.1	0.715	300	106	80	-2.57E-06
7.6	22.1	0.715	300	106	60	-1.25E-06
7.6	24.1	0.915	100	126	60	-1.26E-06
7.6	24.1	0.915	300	106	60	-1.35E-06
7.6	24.1	0.715	100	106	60	-2.70E-06
9.6	22.1	0.915	100	126	60	2.89E-06
8.6	23.1	0.815	200	116	70	5.56E-08
8.6	23.1	0.815	200	116	70	5.56E-08
8.6	22.1	0.815	200	116	70	6.45E-07
9.6	22.1	0.715	300	106	80	1.85E-06
7.6	24.1	0.915	300	126	80	-1.44E-06
8.6	23.1	0.715	200	116	70	-3.09E-07
7.6	22.1	0.915	100	126	80	-4.21E-07

α_1 (ppm/°C)	α_2 (ppm/°C)	f_{wdith} (μm)	Normalized f_{wdith} (μm/μm)	CTE (ppm/°C)
10	27	814	6.56E-02	1.29
10	26	814	6.56E-02	1.81
10	25	814	6.56E-02	2.33
10	24	814	6.56E-02	2.85
10	27	1366	1.10E-01	4.51
10	27	674	5.44E-02	0.22
10	27	476	3.84E-02	-1.79
8.6	23.1	814	6.56E-02	1.19
8.6	23.1	476	3.84E-02	-1.45
7.6	23.1	814	6.56E-02	-0.33
7.6	23.1	476	3.84E-02	-3.14

A.3 Metastructure Array FEM Results

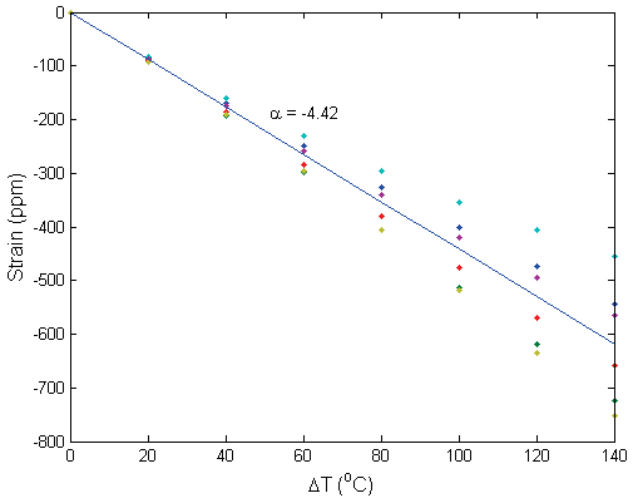

Figure A.3.1 Strain vs temperature calculated by FEM at adjacent frame nodes for a Kovar/Al metastructure

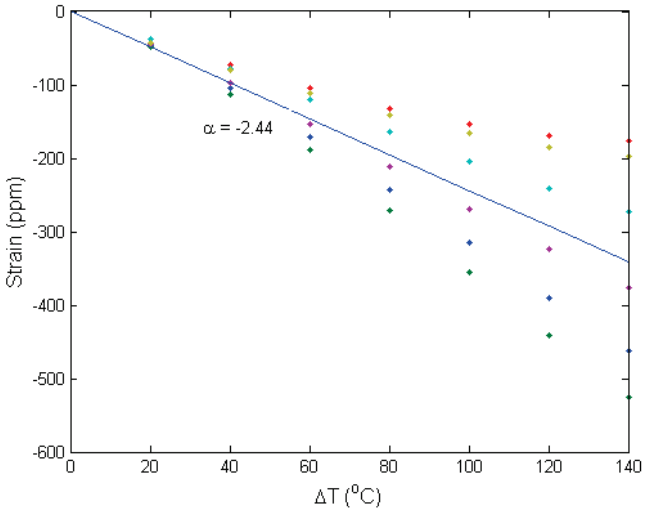

Figure A.3.2 Strain vs temperature calculated by FEM at adjacent plate centroids for a Kovar/Al metastructure

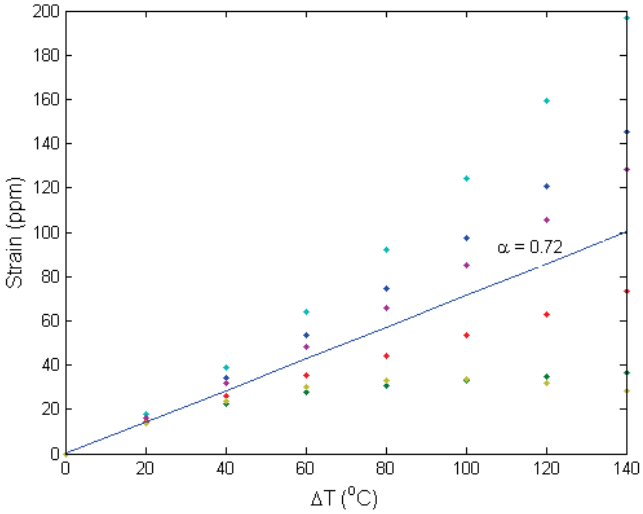

Figure A.3.3 Strain vs temperature calculated by FEM at adjacent frame nodes for a Ti/Al metastructure

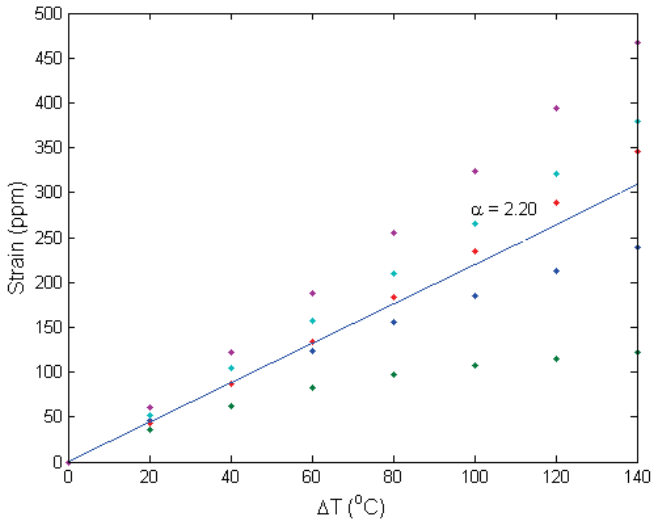

Figure A.3.4 Strain vs temperature calculated by FEM at adjacent plate centroids for a Ti/Al metastructure

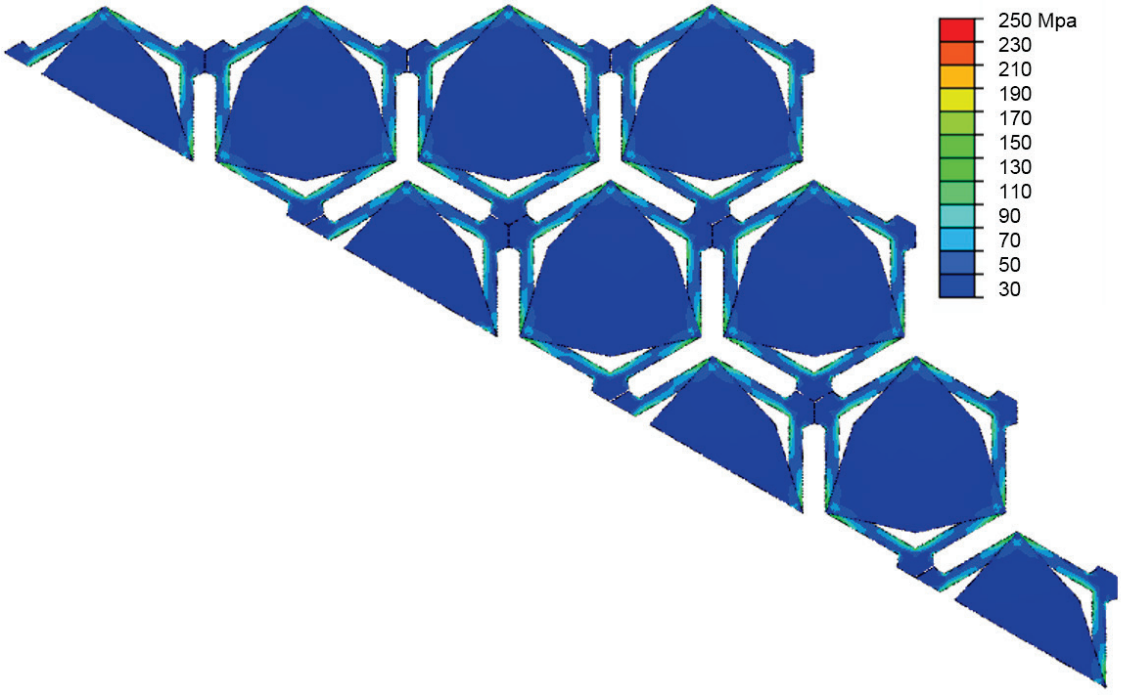

Figure A.3.5 FEM prediction of Von Mises stress developed in metastructure as a result of thermal loading at 150 °C

A.4 Thin Film Characterization

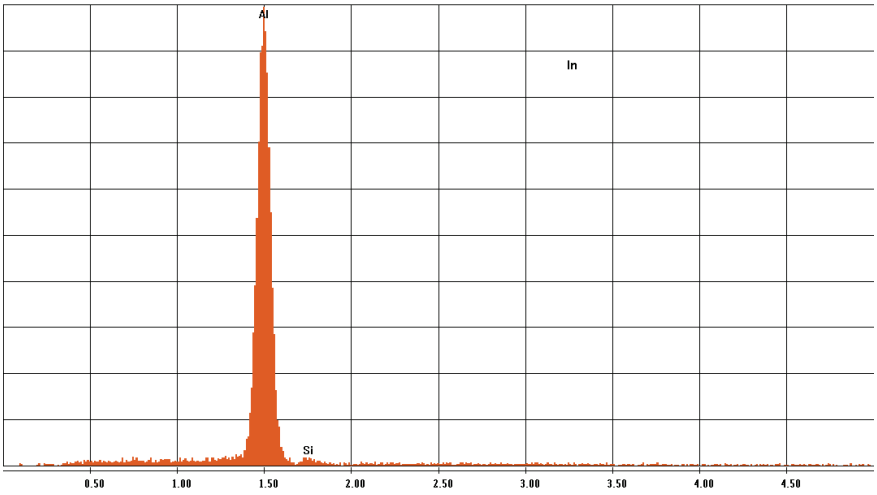

Figure A.4.1 EDX spectrum of Aluminum thin film after annealing.

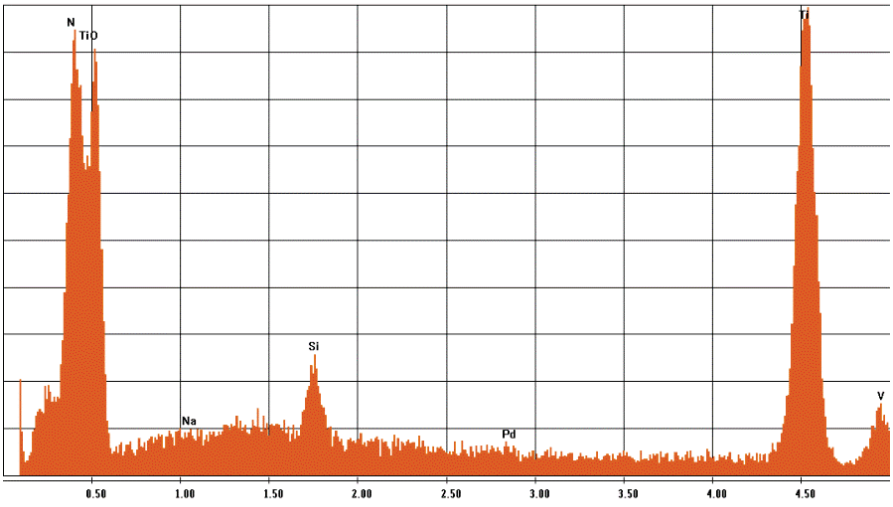

Figure A.4.2 EDX spectrum of Titanium thin film after annealing.

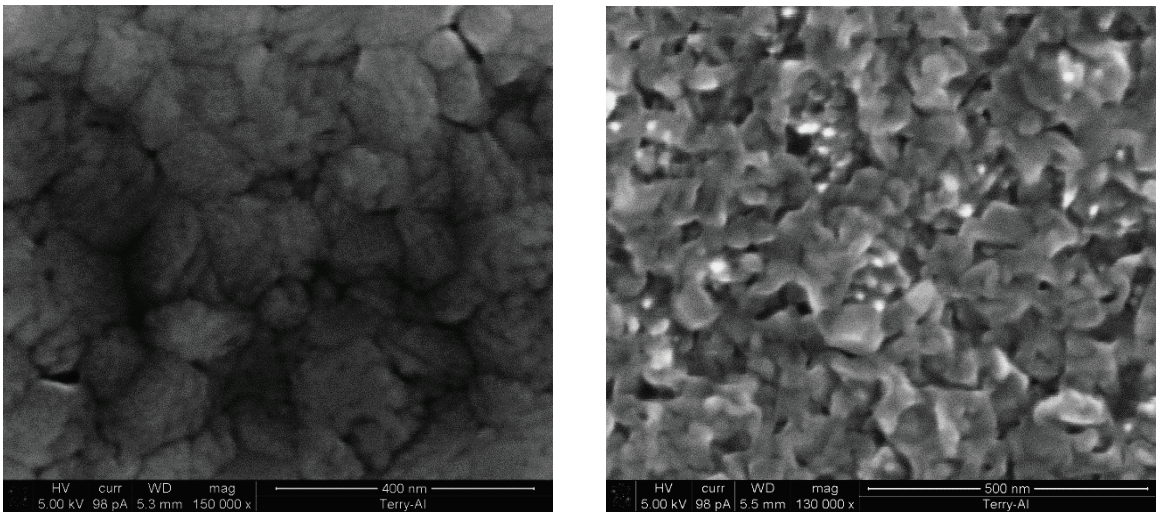

Figure A.4.3 SEM image of Al (left) and Ti (right) thin film after annealing.

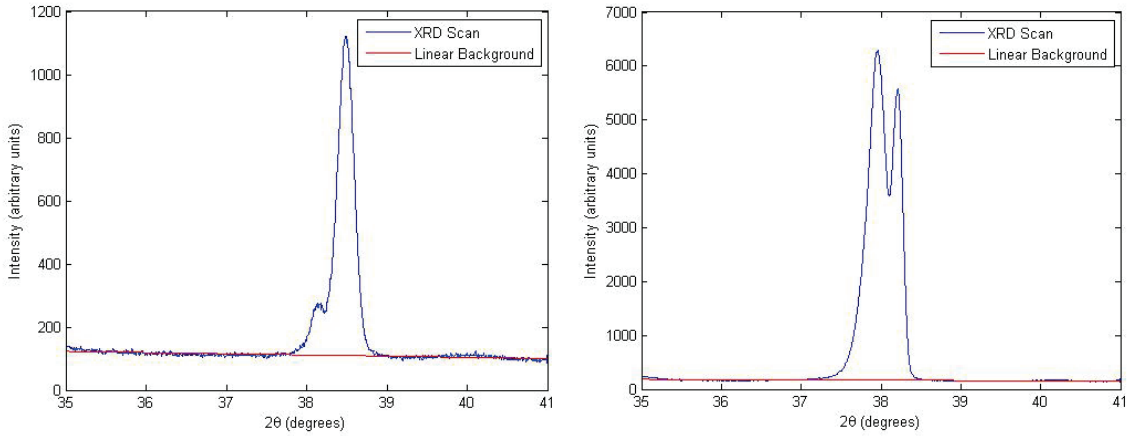

Figure A.4.4 XRD spectrum of Al (left) and Ti (right) thin films after annealing

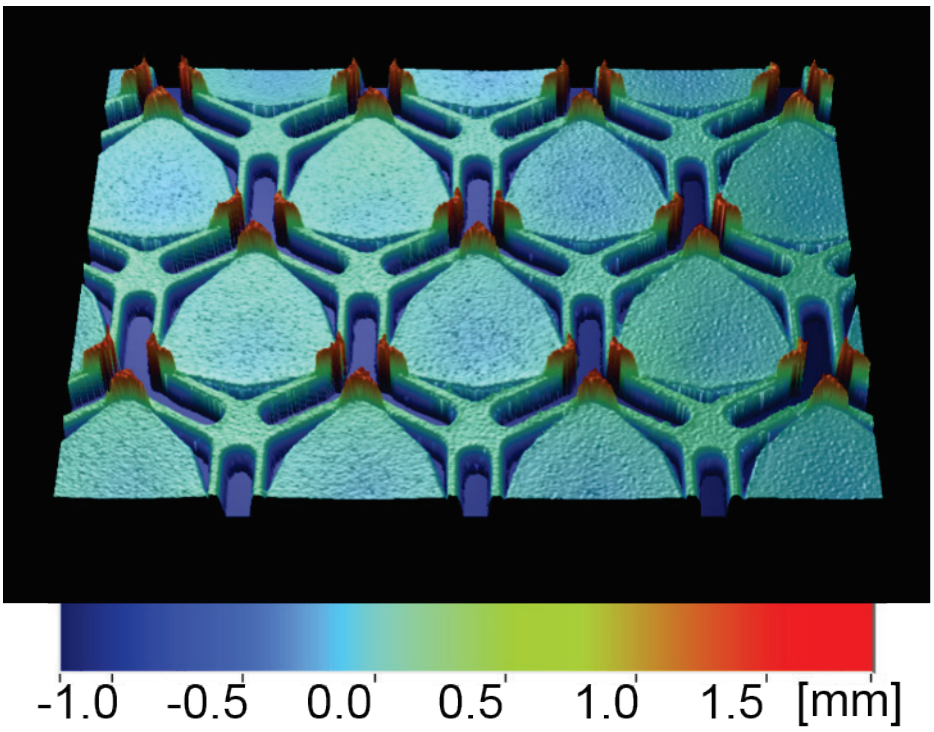

Figure A.4.5 Optimcal inteferometry image of fabricated thin film Ti/Al metastructure array

A.5 Thin Film Metastructure Array FEM

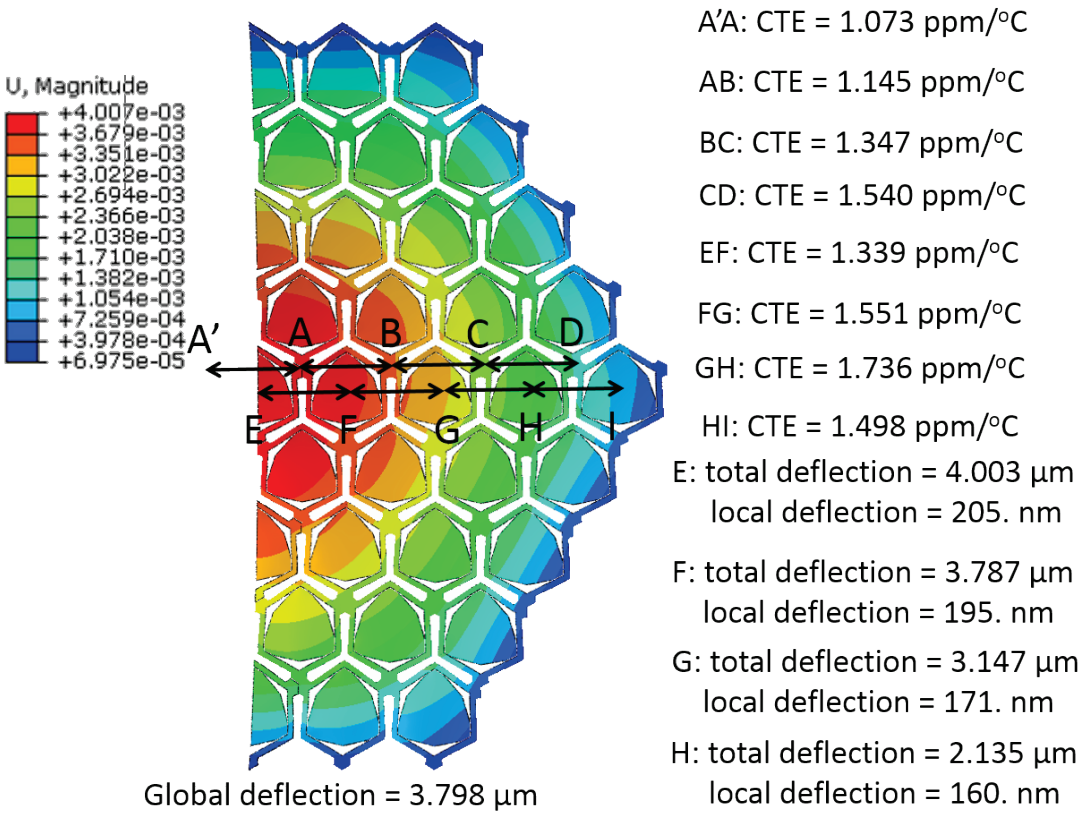

Figure A.5.1 FEM prediction of thin film Ti/Al metastructure array thermal deformation at 116 °C. The CTE computed between various points is shown on the right.